Local Modification and Characterization
of the Electronic Structure
# of Carbon Nanotubes

INAUGURALDISSERTATION

zur
Erlangung der Würde eines Doktors der Philosophie
vorgelegt der
Philosophisch-Naturwissenschaftlichen Fakultät
der Universität Basel
von

Gilles Buchs

aus Jaun(FR)

Dübendorf, 2008

Genehmigt von der Philosophisch-Naturwissenschaftlichen Fakultät auf Antrag
der Herren Professoren:

Prof. Dr. C. Schönenberger
Prof. Dr. K. Kern
Prof. Dr. C. Hierold

Basel, den 20. Mai 2008

Prof. Dr. H. -P. Hauri, Dekan

Scientific discoveries are an opportunity to worship.

Francis S. Collins

Contents

Table of Abbreviations

AC	Alternative Current
AFM	Atomic Force Microscopy
Ar	Argon
BZ	Brillouin Zone
C	Carbon
CB	Conduction Band
CBE	Conduction Band Edge
CNT	Carbon Nanotube
CNTFET	Carbon Nanotube Field-Effect Transistor
CNP	Charge Neutrality Point
Co	Cobalt
CO	Carbon Monoxide
CTE	Complete Thermodynamic Equilibrium
CVD	Chemical Vapor Deposition
DC	Direct Current
DCE	Dichloroethane
DFT	Density Functional Theory
DNA	Deoxyribonucleic Acid
DOS	Density of States
DV	Double Vacancy
ECR	Electron Cyclotron Resonance
EELS	Electron-Energy Loss Spectroscopy
Fe	Iron
FET	Field-Effect Transistor
FFT	Fast Fourier Transform
FWHM	Full Width at Half Maximum
H	Hydrogen
HiPco	High Pressure CO disproportionation process
HOMO	Highest Occupied Molecular Orbital
HOPG	Highly Oriented Pyrolytic Graphite
HREELS	High Resolution Electron-Energy Loss Spectroscopy
I-V	Current-voltage characteristic
K	Potassium
LDOS	Local Density of States
LT	Low Temperature ($4.2\,\mathrm{K}$)
LTE	Local Thermodynamic Equilibrium
MOSFET	MetalOxideSemiconductor Field-Effect Transistor
MWNT	Multi-Walled Carbon Nanotube

N	Nitrogen
NDR	Negative Differential Resistance
Ni	Nickel
QD	Quantum Dot
RF	Radio Frequency
RMS	Root Mean Square
RT	Room Temperature ($20°C$)
SED	Selective Electrochemical Deposition
SEM	Scanning Electron Microscopy
SET	Single Electron Transistor
SGM	Scanning Gate Microscopy
Si	Silicon
STM	Scanning Tunneling Microscopy
STS	Scanning Tunneling Spectroscopy
SV	Single Vacancy
SW	Stone-Wales (defect)
SWNT	Single-Walled Carbon Nanotube
TB	Tight Binding
TDOS	Total Density of States
TEM	Transmission Electron Microscopy
tmAFM	tapping mode Atomic Force Microscopy
TV	Triple Vacancy
UHV	Ultra High Vacuum
VB	Valence Band
VBE	Valence Band Edge
VHS	Van Hove Singularity

Introduction

In december 1959, in his famous lecture "There's Plenty of Room at the Bottom" given at Caltech, Richard Feynman imagined the possibility to manufacture objects at the nanometer scale (1 nm = 10^{-9} m) by maneuvering matter atom by atom. This revolutionary idea paved the way to envision systems designed and engineered at the ultimate length scale relevant to material science. Such systems have become a reality today and the efforts to understand, build and use them encompass what is called nanotechnology. Today, nanoscience and nanotechnology constitute very active and promising multidisciplinary research areas, bringing together engineers and scientists from several fields like physics, chemistry, materials science, electronics, biology and medicine. A strong focus is given to the understanding of the correlations between the structure of a material at the atomic level and its optical, chemical and electronic properties. But nanoscience and nanotechnology also aim at developing and improving techniques for manufacturing nanomaterials for new applications.

When the dimensions of an object are shrunk down to a scale of the order of the Fermi wavelength of the electrons, the said object will behave according to the rules of quantum mechanics, and novel properties will emerge that may be completely different from the bulk properties. One well-known example for this is provided by graphite.

Graphite is a carbon allotrope whose structure consists of a stacking of two-dimensional, sp^2-bonded carbon layers interacting with each other by van-der-Waals interactions. Because of these weak inter-layer interactions, graphite is known as a mechanically soft material which is used in pencil leads or, due to its high melting point and good electrical conductivity, in the electrodes of arc lamps and arc furnaces. Now, if one imagines isolating a small sheet of a graphite monolayer and roll it into a cylinder with nanometer scale diameter, one will obtain a nano-object with amazing mechanical, thermal and electronic properties. Such objects called carbon nanotubes (CNT) have been discovered in 1991 [1] and since then have led to an explosion of research activities in many labs worldwide. In terms of mechanical properties, carbon nanotubes are among the strongest and most

resilient materials known to exist in nature, with a Young's modulus approaching 1.2 TPa and a tensile strength 80 times higher than high strength steel. Their electronic properties are unique in the sense that they are completely determined by the tube geometry, resulting in semiconducting or metallic character, with observed ballistic transport properties up to a few micrometers for the latter [2]. During the last decade, CNT-based device prototypes like single-electron transistors (SET) [3], field-effect transistor (FET) [4], logic gates or memories [5, 6] could be realized. Especially, it was demonstrated that a CNTFET has superior performance over standard Si MOSFETs [7]. CNT based FETs are then very promising to be used as building blocks for future large-scale integrated circuits as the actual silicon technology might soon reach its limits in terms of miniaturization. Recent progress in separation techniques where individual chiralities can be isolated further sustain this assumption [8]. Also, growth techniques got improved with regard to high purity of the raw material [9] and still constitute an active research field towards a highly desired chirality selective growth. Despite all these advances, the development of a reliable and massively parallel integration technology for CNT-based electronic devices that can compete in yield and structure size with silicon technology is still missing and it is not yet clear if such a technology can be established.

Up to now, especially in the worldwide race towards the realization of the most competitive SWNT-based transistor, research focussed on mainly defect free nanotubes. Nevertheless, researchers reported interesting results from the investigation of intrinsic defects. For example, a classical $p - n$ rectifying behavior has been reported for an intramolecular junction in a single-walled carbon nanotube (SWNT), due to a special arrangement of the C-C bonds at a tube kink [10]. Furthermore, two separated intrinsic defects in a metallic SWNT embodied in a source-drain-gate device showed gate-dependent resonant backscattering properties [11]. And more recently, a high gate sensitivity at the position of individual defects of unknown nature in similar devices has been observed [12].

These findings show that whereas a defect can be considered as a nuisance, on the other hand it can be regarded as an opportunity to tailor the electronic properties of CNTs. Thus, the question arises to know how and to which extent different types of defects can change the electronic properties of SWNTs. This is important in view to possibly modify and improve the properties of existing CNT-based electronic devices such as CNTFETs, or even further to define new kind of quantum devices with possibly new properties entirely designed by a controlled creation of specific defects.

The fundamental questions put above constitute the main motivation of this Ph.D thesis. Here, we propose a study of the interplay between artificially created defects and the electronic structure of SWNTs by means

of low temperature scanning tunneling microscopy and spectroscopy (LT-STM/STS). LT-STM/STS constitutes the perfect investigation tool to achieve this goal since it enables us to directly probe the electronic structure of solids with atomic resolution. The defects we investigate here are created by ion bombardment. In order to study the effect of well-defined individual defects, a low invasive method for their creation must be privileged. To serve this purpose, we have chosen an ECR plasma source producing low energy ions of the order of a few eV.

In a first phase, we investigated hydrogen ion-induced defects, motivated by a earlier work on graphite where it was shown that such defects act as scattering centers leading to large momentum scattering. In a second phase, we studied the effects of an exposition of the tubes to nitrogen plasma. This is motivated by the fact that the intrinsic p-type doping of CNTFETs draws up a demand on techniques allowing n-type doping in view to define p-n junctions, which are indispensable key-blocks towards a future SWNT-based technology. Different approaches like deposition of K donor atoms [13] or attempts to create substitutional N sites during the tube growth [14] present inhomogeneity problems. A controlled substitution technique is thus highly desirable.

In the last phase, we were interested to create harsher defects like vacancies and double vacancies, which have shown to largely increase the resistivity of SWNTs [15]. This could be achieved by medium energy argon ions of 200 eV and 1.5 keV produced by an ion gun.

Outline

The present Ph.D thesis is organized as follows:

Chapter 1 gives a brief introduction on the geometrical structure, synthesis and electronic structure of SWNTs. The actual knowledge on the effects of structural defects on the electronic and transport properties of SWNT will be given in the form of an overview of the literature.

Chapter 2 describes the experimental methods used in this work. As the principal investigation tool, the basic theoretical principles of STM and STS will be described, followed by a technical description or our LT-STM/STS setup. A short introduction to tmAFM will also be given. And finally, the basic principles of cold plasma physics will be described, with emphasis on ECR plamsa and DC glow discharge.

Chapter 3 describes in details the different steps involved in the sample preparation, from the SWNT suspension to the defect free SWNT sample characterization by means of tmAFM and LT-STM/STS.

Chapter 4 and 5 present topography and spectroscopy investigations on ECR H- and N-plasma-induced defects. In both cases, new defect-induced gap states in semiconducting SWNTs could be observed. For the ECR-H plasma treatment, STM/STS investigations combined with first principle *ab initio* calculations demonstrated that a correlated chemisorption of H-adatoms on the SWNT wall gives rise to symmetric paired gap states.

Chapter 6 presents topography and spectroscopy investigations on 200 eV and 1.5 keV Ar$^+$ion-induced defects. From first principle *ab initio* calculations combined with our experimental results, we concluded on the formation of two main defect types: vacancies and C-adatoms giving rise to new states in the semiconducting gap. An increase of the complexity of the defect configuration has been observed for 1.5 keV treatement, compared to 200 eV.

Chapter 7 gives an extended discussion on the often observed NDR behavior in the $I - V$ curves recorded at defect sites. Within a simple tunneling model, we could explain this phenomenon by a voltage dependence of the tunneling barrier height.

Chapter 8 describes electronic confinement effects observed between consecutive defects in metallic SWNTs. The capability of our method to create sufficiently strong scattering centers shows the possibility to define room temperature active intra-tube quantum dots. The discussion of the experimental observations mainly based on a Fourier analysis of the spatial variation of the differential conductance is made on the basis of a scattering matrix formalism as well as a geometrical approach within the Fourier projection-slice theorem.

Details on the *ab initio* calculations for different defect structures and additional calculation results are given in Appendices A and B, respectively.

Chapter 1

Single-walled carbon nanotubes

The pure element carbon can exist as several different allotropes. Until the discovery of the fullerenes in 1985 [16], only amorphous carbon, graphite and diamond were known. The most famous of this class of molecules is the spherical Buckyball C_{60}, which has a bond structure analog to the seams of an "old fashioned" soccer ball connecting the 12 heptagonal and 20 hexagonal leather patches. After this discovery, it became evident that sp^2-hybridized graphene layers exist not only as planar honeycomb sheets like in graphite but also as spherically curved and closed cages. Later, in 1991, Sumio Iijima discovered a cylindrical form of the buckyball, known as carbon nanotube. These new members of the fullerene family fall into two broad categories: single-walled carbon nanotubes (SWNT) consisting of one graphene sheet rolled into a cylinder and multi-walled carbon nanotubes (MWNT) made of several concentric SWNTs. The outstanding mechanical and electronic properties of SWNTs have been largely investigated and today still constitute the object of intensive research activities. Notably, a SWNT can be viewed as the prime example for a molecular one dimensional electronic system and can be used for the realization of future SWNT-based quantum devices. In the following paragraphs, we are going to give a short introduction to the structure, electronic properties and synthesis of SWNTs. A more detailed introduction can be found in many textbooks like *i.e.* [17–19] and a recent review article [20].

1.1 Atomic structure of SWNTs

Geometrically, a SWNT can be regarded as a single graphene strip rolled into a cylinder. Its structure is generally indexed by its chiral vector $\mathbf{C}_h$, as defined by the circumferential vector $\vec{AA'}$ which starts and ends on the same lattice site on the SWNT and is brought back to the basic graphene sheet as illustrated in Fig. 1.1. The circumferential vector is expressed as
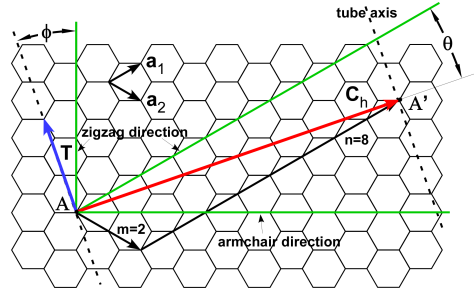
Figure 1.1: *Graphene honeycomb lattice with chiral vector $\mathbf{C}_h = n\mathbf{a}_1 + m\mathbf{a}_2$ and translational vector $\mathbf{T}$. An example for the construction of a $(8,2)$ metallic chiral SWNT is illustrated.*

a linear combination of the two basis vectors $\mathbf{a}_1$ and $\mathbf{a}_2$ of the hexagonal honeycomb lattice with:

$$\mathbf{C}_h = n\mathbf{a}_1 + m\mathbf{a}_2. \tag{1.1}$$

Thus, the geometry of a SWNT is completely defined by the pair of integers (n,m), called chiral indices.

The diameter d_{t} of a SWNT is given by:

$$d_{\mathrm{t}} = \frac{|\mathbf{C}_h|}{\pi} = \frac{a}{\pi} \cdot \sqrt{n^2 + nm + m^2} \tag{1.2}$$

where a is the lattice constant of the honeycomb lattice: $a = \sqrt{3} \cdot a_{\mathrm{CC}}$ ($a_{\mathrm{cc}} \approx 1.42$ Å is the C-C bond length). The chiral angle θ, which is the angle between $\mathbf{C}_h$ and the zigzag direction of the graphene sheet parallel to a_1 can be expressed as:

$$cos\,\theta = \frac{\mathbf{C}_h \cdot \mathbf{a}_1}{|\mathbf{C}_h|\,|\mathbf{a}_1|} = \frac{2n + m}{2\sqrt{n^2 + nm + m^2}} \tag{1.3}$$

Because of the hexagonal symmetry of the graphene lattice, the possible values of θ are in the range $0 \leq |\theta| \leq 30°$. For the experimental assignment of SNWTs (see section 3.4.2), we generally use the complementary angle ϕ ($\phi = 30° - \theta$) between the tube axis and the zigzag direction, as shown in Fig. 1.1. Nanotubes of the type $(n,0)$ with $\phi = 30°$ are called zigzag tubes and nanotubes of the type (n,n) with $\phi = 0°$ are called armchair tubes. Both armchair and zigzag nanotubes are achiral tubes, in contrast to chiral tubes with $(n, m \neq n \neq 0)$ (see Fig.1.2).

The unit cell of a SWNT is defined by the chiral vector $\mathbf{C}_h$ and the translational vector $\mathbf{T}$ perpendicular to $\mathbf{C}_h$. The translational vector $\mathbf{T}$ (see Fig. 1.1) is the smallest graphene lattice vector which defines the translational period t along the tube axis, and can be expressed as $\mathbf{T} = t_1\mathbf{a}_1 + t_2\mathbf{a}_2$ with:

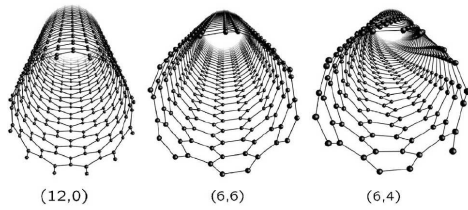$$t_1 = \frac{2m + n}{N_{\mathrm{R}}}, \qquad t_2 = -\frac{2n + m}{N_{\mathrm{R}}} \tag{1.4}$$

Figure 1.2: *Atomic structures of achiral $(12, 0)$ zigzag, $(6, 6)$ armchair and chiral $(6, 4)$ nanotubes. Taken from [20].*

where N_R is the greatest commond divisor of $(2m + n)$ and $(2n + m)$. The norm of $\mathbf{T}$ is given by:

$$|\mathbf{T}| = \frac{3a_\mathrm{CC}\sqrt{n^2 + nm + m^2}}{N_\mathrm{R}} \tag{1.5}$$

The nanotube unit cell is thus formed by a cylindrical surface with height $|\mathbf{T}|$ and diameter d_t, containing a number of atoms:

$$N_\mathrm{c} = \frac{4\left(n^2 + nm + m^2\right)}{N_\mathrm{R}} \tag{1.6}$$

Many effects like optical transitions in semiconducting SWNTs or first-order Raman scattering (phonons) can be treated by means of symmetry line groups. A detailed study on SWNT line groups is given in textbooks cited above.

1.2 Electronic structure of SWNTs

To understand the electronic properties of SWNTs, a simple way is to start with the band structure of graphene, which underlies also the band structure of the nanotubes. Graphene is characterized by two types of chemical bonds which are linked to the sp^2 hybridization of the carbon atomic orbitals. The strong covalent in-plane σ bonds, which connect the carbon atoms to form the honeycomb lattice, have their corresponding energy bands far from the Fermi level and thus do not contribute to the electronic transport properties of graphene (and nanotubes). The remaining p_z orbitals, pointing out of the σ-bond plane, cannot couple with the σ states for symmetry arguments. The lateral interaction with neighboring p_z orbitals creates delocalized π (bonding) and π^* (antibonding) states, which determine the energy bands around the Fermi energy E_F.

1.2.1 Tight-binding model of graphene

The unit cell of graphene (defined by $\mathbf{a}_1$ and $\mathbf{a}_2$), is composed of two atoms A and B, as shown in Fig. 1.3. A and B atoms form two complementary,
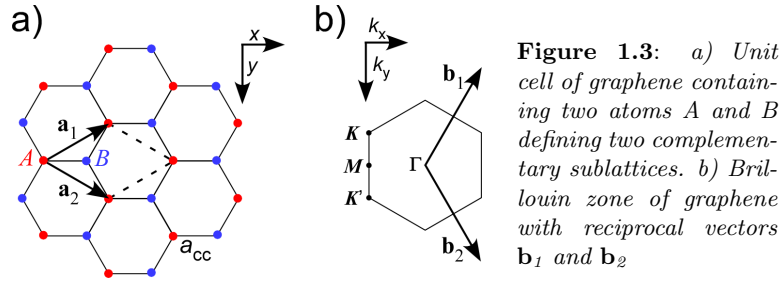
a)

b)

Figure 1.3: *a) Unit cell of graphene containing two atoms A and B defining two complementary sublattices. b) Brillouin zone of graphene with reciprocal vectors* **b**$_1$ *and* **b**$_2$

hexagonal sublattices. The condition $\mathbf{a}_i \cdot \mathbf{b}_j = 2\pi\delta_{ij}$ allows one to obtain the reciprocal-lattice vectors $\mathbf{b}_1$ and $\mathbf{b}_2$. The electronic structure of an infinite extended graphene sheet can be calculated within a tight-binding (TB) approximation, where the p_z electrons can be treated independently of other valence electrons. By considering two independent wavefunctions (obeying to the Bloch theorem) for the electrons corresponding to the two complementary sublattices and neglecting the overlap matrix elements $S = \langle\, p_z^A|\, p_z^B \rangle$ one obtains the following relation for the energy dispersion of the bands in graphene:

$$E^{\pm}(k_x, k_y) = \pm\gamma_0 \sqrt{1 + 4cos\frac{\sqrt{3}k_x a}{2}cos\frac{k_y a}{2} + 4cos^2\frac{k_y a}{2}} \qquad (1.7)$$

where $\gamma_0 = 2.9 \pm 0.2$ eV is the overlap integral between nearest neighbor orbitals. The $\mathbf{k} = (k_x, k_y)$ vectors that belong to the first hexagonal Brillouin zone (BZ), shown in Fig. 1.3, constitute the ensemble of available electronic momenta. Figure 1.4 shows the dispersion relation along the high symmetry directions of the BZ, defined by the Γ, M and K points. The bonding and antibonding bands touch at the six K points at the corners of the first BZ, thus allowing the classification of graphene as a semimetal. Three out of the six K points are equivalent due to the spatial symmetry of the hexagonal lattice, thus two distinguishable points remain called K
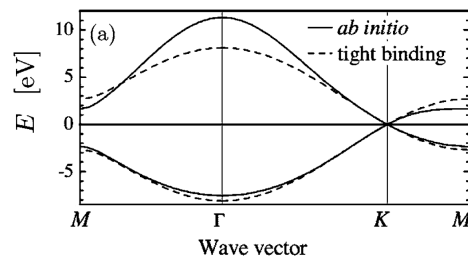

Figure 1.4: *Dispersion relation of graphene calculated from Eq. 1.7, along high symmetry directions of the BZ (dashed line), and* ab initio *calculation (solid line). Taken from [20].*

and K', as shown in Fig. 1.3. At zero temperature, the bonding bands are completely filled and the antibonding bands are empty. The undoped state, where the Fermi surface contains only the six K points is called the charge neutrality point (CNP). As can be seen from Fig. 1.4, the dispersion relation derived from the simple TB approximation shows some deviations as compared to *ab initio* calculations. A considerable improvement can be achieved when considering S to be non zero and if next nearest neighbors are included in the TB model [18].

1.2.2 Zone-folding approximation

Due to periodic boundary conditions along the circumference of a SWNT, the allowed wave vectors in direction perpendicular to the tube axis are quantized. In contrast, the wave vectors in direction parallel to the tube axis remain continuous under the assumption of an infinite length of the tube. The application of periodic boundary conditions around the tube circumference leads to the following restrictions on the allowed wavefunctions:

$$\Psi_{\mathbf{k}}\left(\mathbf{r} + \mathbf{C}_h\right) = e^{i\mathbf{k}\cdot\mathbf{C}_h}\Psi_{\mathbf{k}}\left(\mathbf{r}\right) = \Psi_{\mathbf{k}}\left(\mathbf{r}\right) \tag{1.8}$$

with the vectors $\mathbf{r}$ and $\mathbf{k}$ taken on the tube surface. The first first equality stems from the Bloch theorem. Thus, the electronic states are restricted to $\mathbf{k}$ vectors that fulfill the condition:

$$\mathbf{k} \cdot \mathbf{C}_h = 2\pi q \tag{1.9}$$

with q an integer. Plotting these allowed vectors for a given SWNT onto the BZ of graphene generates a series of parallel and equidistant lines. The distance between lines is found from Eq. 1.9 to be $\Delta k = 2/d_{\mathrm{t}}$. The length, number and orientation of these lines depend on the chiral indices (n, m) of the SWNT, and can be found from Eqs. 1.1, 1.4 and 1.6 with the relation $\mathbf{a}_{\mathrm{i}} \cdot \mathbf{b}_{\mathrm{j}} = 2\pi\delta_{\mathrm{ij}}$ [17]. The length is thus found to be $2\pi/\left|T\right|$, the orientation with respect to the reciprocal lattice is given by θ, and the number of lines is equal to $N_{\mathrm{c}}/2$. The parallel lines shown in Fig. 1.5 a) and b) are examples of allowed $\mathbf{k}$ modes for a metallic $(5, 5)$ armchair and a semiconducting $(10, 0)$ zigzag, respectively. Note that since the nanotubes are one dimensional, their BZ is one dimensional as well, with zone boundaries usually labeled X, namely: $\mathbf{X} = \pm\left(\pi/\left|\mathbf{T}\right|\right)\mathbf{k}_{\|}$, with $\mathbf{k}_{\|}$ being the reciprocal space unit vector along the $\mathbf{T}$ direction.

The basic idea behind the zone-folding approximation is that the electronic band structure of a specific nanotube is given by the superposition of the graphene electronic energy bands along the corresponding allowed $\mathbf{k}$ lines, *i.e.* a pair of conduction (antibonding) and valence (bonding) bands
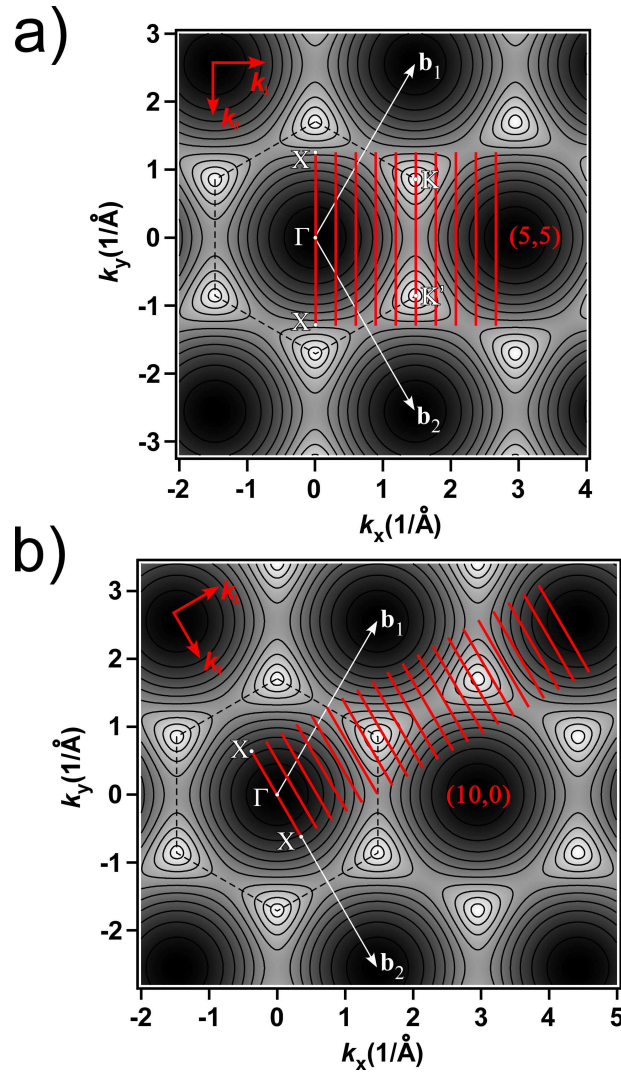
Figure 1.5: *a) Reciprocal lattice of graphene with energy contour plot of the bonding band. The allowed* **k** *lines for a metallic armchair* $(5,5)$ *SWNT arising from the quantization condition around the circumference:* $\mathbf{C}_h \cdot \mathbf{k} = 2\pi q$ *are drawn in red.* $\mathbf{k}_\perp$ *and* $\mathbf{k}_\parallel$ *are the unit vectors in directions of* $\mathbf{C}_h$ *and* $\mathbf{T}$, *respectively. b) the same for a semiconducting* $(10,0)$ *SWNT.*
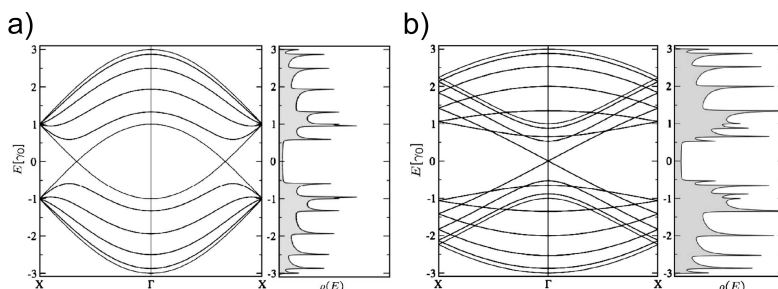
Figure 1.6: *a) Band structure and density of states for a metallic armchair* $(5,5)$ *SWNT within the zone-folding model. The Fermi level is located at zero energy. b) The same for a metallic zigzag* $(9,0)$.

for each $\mathbf{k}$ line. Therefore, if the graphene K point is crossed by an allowed $\mathbf{k}$ line, the SWNT is metallic. With $\mathbf{K} = \frac{1}{3}(\mathbf{b}_1 - \mathbf{b}_2)$, it can be shown that a SWNT is metallic if the condition $n - m = 3l$, with l an integer, is fulfilled. Furthermore, it can be shown that whenever $n - m = 3l$, if $(n - m)$ is a multiple of $3d$, with d being the gcd of (n, m), the bonding and antibonding bands of the metallic SWNT will touch at $k = \pm 2\pi/3T$ with a twofold degeneracy. If $(n - m)$ is not a multiple of $3d$, then the bands will touch at $k = 0$ with a fourfold degeneracy. To illustrate these situations, the electronic structures of metallic armchair $(5,5)$ and zigzag $(9,0)$ calculated within the zone-folding approximation are given in Fig. 1.6 a) and b), respectively. From a perturbation expansion analysis in the neighborhood of the Fermi surface using $\mathbf{k} = \mathbf{K} + \delta\mathbf{k}$, it can be shown that the dispersion relation close to E_{F} can be written as:

$$E^{\pm}(\delta\mathbf{k}) \simeq \pm \left(\frac{\sqrt{3}a}{2}\right) \gamma_0 |\delta\mathbf{k}| = \pm \hbar v_{\mathrm{F}} |\delta\mathbf{k}| \qquad (1.10)$$

where $v_{\mathrm{F}} \simeq 8 \times 10^5$ m·s^{-1} is the Fermi velocity of graphene. This linear energy-momentum relation of electrons has important implications in graphene [21,22] and bears much importance in the Luttinger-liquid behavior for low-energy excitations in nanotubes [23].

When $n - m = 3l \pm 1$, the allowed $\mathbf{k}$ vectors do not cross the K or K' points, making the SWNT semiconducting. The band structure of a semiconducting $(10,0)$ SWNT is shown in Fig. 1.7. By following a similar calculation as for the prior case, the gap opening at the Fermi level can be found to be:

$$\Delta E_{\mathrm{g}} = \frac{2a_{\mathrm{cc}}\gamma_0}{d_{\mathrm{t}}} \qquad (1.11)$$

This $1/d_{\mathrm{t}}$ dependence of the gap on the diameter d_{t} relies on the assumption of a linear dispersion cone around E_{F} for graphene. In reality, this is not the case as can be seen in the energy contour plot around the K points for the bonding band of graphene in Fig. 1.5. An effect called trigonal warping induces a dependence of the bandgap not only on the diameter, but also on the chiral indices (n, m) [24].

Due to its 1D character, the density of states (DOS) $\Delta N/\Delta E$ of SWNTs is proportional to $\left|\frac{\partial E(k)}{\partial k}\right|^{-1}$ and diverges as $|E|/\sqrt{E^2 - E_0^2}$ close to band extrema E_0, as can be seen in the right hand panels of Figs. 1.6 and 1.7. These singularities in the DOS are called Van Hove singularities (VHS). Many experimental investigations based on scanning tunneling spectroscopy (STS) and transport measurements showed very good agreement with the theoretical predictions based on the zone folding theory [25].

In the zone-folding scheme, the selected states are those of a planar graphene sheet and thus curvature effects that occur in real SWNTs are neglected. Curvature induces differences in the hopping term γ_0 between a carbon atom and its three neighbors, due to bond length changes and the formation of an angle for two p_{z} orbitals located on bonds not strictly parallel to the tube axis. This effect induces a shift of the Fermi vector k_{F} of metallic tubes away from BZ corners (K point) of the graphene sheet. For armchair tubes, curvature shifts k_{F} along an allowed k-line in the graphene BZ, thus armchair SWNTs always preserve their metallic character with finite curvature. However, for metallic nonarmchair SWNTs, k_{F} moves out of an allowed k-line, opening a very small bandgap at E_{F}. This so-called secondary gap which scales as $1/d_{\mathrm{t}}^2$ is generally small ($\sim$10 meV for $d_{\mathrm{t}} = 1$ nm). LDOS measurements by STS confirm this expected $1/d_{\mathrm{t}}^2$ dependence for zigzag SWNTs and show that armchair SWNTs remain truly metallic [26]. A second effect is the mixing between π and σ states with the formation of hybrid orbitals that exhibit partial sp^2 and sp^3 character. In the case of small SWNTs, the zone-folding approximation may fail and *ab initio* calculations should be performed to predict the electronic properties. However this effect is unimportant for tube diameter around and larger than
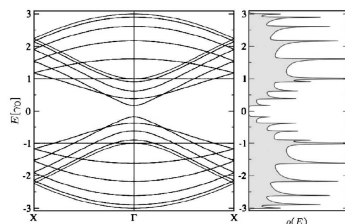

Figure 1.7: *Band structure and density of states for a $(10, 0)$ zigzag nanotube within the zone-folding model. The Fermi level is located at zero energy.*

1 nm [20].

1.3 Synthesis

Carbon nanotubes can be synthesized by various methods with arc-discharge, laser ablation and chemical vapor deposition (CVD) being the principal ones. In these methods, the carbon nanotubes (SWNTs or/and MWNTs) are grown from the condensation of a carbon-containing gas phase in most of the cases in the presence of metallic catalysts like Fe, Ni or Co. The produced SWNTs mostly bunch in the form or ropes with tens of individual nanotubes close-packed via van-der-Waals interactions.

The SWNTs used in this work have been produced by the high pressure CO disproportionation process (HiPco) [9], which belongs to the CVD family. In CVD, a flowing hydrocarbon gas is decomposed at a growth temperature between 500 and 1000°C. The precipitation of carbon from the saturated phase in metal catalyst particles leads to the formation of a tubular carbon solid. In the HiPco technique, the SWNTs are produced by flowing CO, which is the carbon feedstock, mixed with a small amount of iron-containing catalyst precursor $Fe(CO)_5$ through a heated reactor. The diameter of SWNT produced by the HiPco technique are generally smaller (typically ~ 1 nm) than for arc-discharge and laser ablation (typical diameters ranging from 1 to 1.6 nm). The as-produced raw material can contain a high degree of impurities, being mainly metal particles and amorphous carbon. These impurities can be removed to a great extent, *e.g* by metal catalyzed oxidation [9]. Furthermore, recent promising progresses have been made in separating SWNTs according to their chirality (n, m) [8]. This is of prime importance towards the realization of future SWNT-based technologies.

1.4 Structural defects

In the previous sections, we described the geometrical and electronic structures of perfect, infinite SWNTs. In reality, SWNTs have a finite length and their intrinsic honeycomb lattice can contain defects. Depending on the type of defects, these may influence the nanotube electronic properties in different ways and therefore also influence the behavior of CNT-based electronic devices.

1.4.1 Geometric and electronic structure

The ends of real, finite SWNTs can, in a certain sense, be viewed as extreme structural defects in the SWNT lattice. These extremities can remain open

or closed with caps formed by the introduction of pentagons in the hexagonal honeycomb lattice. These topological changes are known to initiate sharp resonances in the LDOS close to E_{F}, with their energy position depending on the relative positions of pentagons and their degree of confinement at the tube ends [27].

Structural defects in carbon sp^2 honeycomb network can occur in various forms. A first example of defect, a vacancy, is shown in Figure 1.8 a). A single vacancy (SV) is simply the absence of a carbon atom in the atomic lattice. The lattice will react to the reduced coordination and a reconstruction will take place where two dangling bonds are saturated by forming a common bond [28]. If one removes the remaining twofold coordinated atom in Fig. 1.8, a double vacancy (DV) is formed, where all dangling bond are saturated [15,28]. SVs and DVs can be created by means of irradiation with high-energy electrons or argon ions [15,29,30]. Such kind of irradiations can also give rise to C-adatoms [31]. Chemisorbed adatoms of different species constitute a second class of defects. Adatoms and SVs have been suggested to induce magnetic properties in carbon nanostructures [32]. Further we can also have substitutional incorporation of atoms in the hexagonal lattice of SWNTs, where B, N and O are the most relevant elements for substitutional doping. Very complex defect structures can of course arise from a local combination of all these type of defects.

Figure 1.8 b) shows the maybe least invasive defect type that can occur in SWNT: the so-called Stone-Wales (SW) structure. A SW defect can be viewed as the result of the rotation of a C-C bond by 90° in the hexagonal network, giving rise to a structure showing two adjacent heptagons surrounded by two pentagons [33]. Such topological configurations can be induced by strain [34,35] or by controlled voltage pulses in scanning tunneling spectroscopy [36]. SW defects keep the chirality of the SWNT unchanged, in contrast to pentagon-heptagon pair defects (consisting of only one pentagon adjacent to one heptagon) which can be at the origin of intramolecular
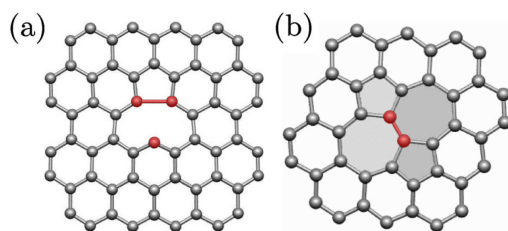

Figure 1.8: *a) Vacancy with reconstruction. The neighboring atoms and the saturating bond are highlighted in red. b) Stone-Wales defect with the rotated bond highlighted in red.*

SWNT junctions (M-S, S-S or M-M) induced by changes in chirality at the position of the defect [10, 37, 38]. Recently, the atomic structure of vacancies, C-adatoms and pentagon-heptagon pairs could be visualized in-situ by means of high-resolution transmission electron microscopy investigation of SWNTs and graphene layers [39].

The effects of specific individual defects on the electronic structure of SWNTs have been studied rather extensively in theoretical investigations, *i.e.* for vacancies and substitutional doping by means of TB and *ab initio* methods [40–42]. From the experimental point of view, the local electronic structure (by means of low temperature STS) of only a few individual defects has been reported. Specifically for pentagon-heptagon defects at intramolecular junctions [10, 38] and SWs [36], further for intrinsic defects of unknown nature [43]. Otherwise, the combined effect of intrinsic defects on the conductivity of long SWNTs has been reported in many transport experiments whose most relevant results are summarized in the following section.

1.4.2 Electron scattering in SWNTs

A generalization on the effects of disorder in nanotube devices is hard to make because of the coexistence of different sources of disorder like structural defects, electrostatic potential fluctuations or even mechanical deformations, each of them having different properties . However, joint intensive experimental and theoretical investigations during the last decade allowed a better understanding.

From the experiment, the effects of disorder on SWNTs can be determined by extracting the corresponding mean-free paths from conductivity measurements. With the considerable improve made in synthesis methods, cleaner nanotubes can be produced and it can be shown that disorder becomes the dominant scattering mechanism only at low temperatures. Mean-free paths of many micrometers are routinely observed from different experimental techniques [2, 44–46]. In contrast, semiconducting tubes show a stronger sensitivity to disorder resulting in shorter mean-free paths [4, 47]. With the assumption of transparent contacts and neglecting electron-phonon coupling, the conductivity in SWNT can vary from the ideal value of $2 \cdot G_0 = 4e^2/h$ (2 conducting channels with twofold spin degeneracy) to lower values due to backscattering of electrons at defect sites.

SWNTs have two degenerate dispersion branches originating from the K and K' points, each with left- and right-moving electrons. As shown in Fig. 1.9 a), two scattering channel can be distinguished: intervalley scattering between K and K' valleys and intravalley scattering where scattered electrons remains in the same valley K or K'. The first involves large

momentum transfer, whereas the latter requires small momentum transfer. Scattering processes can be studied from a $\mathbf{k} \cdot \mathbf{p}$ approximation of the band structure in the vicinity of the K (K') point. In this case, the Hamiltonian reads [48]:

$$H = \hbar v_{\mathrm{F}} \left| \delta \mathbf{k} \right| \sigma_z \tag{1.12}$$

where δk is the wavevector measured relative to the K (K') point and σ_z is the usual Pauli matrix. The eigenfunctions and eigenstates are of the form:

$$|s = \pm 1\rangle = \frac{1}{\sqrt{2}} \begin{pmatrix} s \cdot e^{-i\theta_k/2} \\ e^{i\theta_k/2} \end{pmatrix}; \qquad E = s \cdot \hbar v_F \left| \delta \mathbf{k} \right| \tag{1.13}$$

where θ_k is the angle between $\delta \mathbf{k}$ and the tube axis, and $s = 1$ indicates positive energy, whereas $s = -1$ describes states with negative energy, with respect to the charge neutrality point. The Schrödinger equation described by 1.12 and 1.13 is formally equivalent to the Dirac equation describing a free massless neutrino on a cylinder [49]. Here the spinor is not the electron spin but a pseudospin representing the relative amplitudes on the A and B atomic sites. For a perfect nanotube, the pseudospin is conserved. The mixing of electronic states in the vicinity of K and K' due the presence of impurities can be treated by rewriting the relations 1.12 and 1.13 within a 4×4 perturbation relation, whose symmetry properties result in selection rules for scattering. Following this scheme, Ando and coworkers showed that metallic tubes are affected only by short-range disorder (typical range smaller than a_{cc}), whereas semiconducting tubes are affected by both short- and long-range disorder (slow variation on the scale of a_{cc}) [50, 51]. From an *ab initio* calculation, Choi et al. [41] showed that the conductance of an armchair $(10, 10)$ SWNT remains at its maximal value of $4e^2/h$ around the Fermi level for a SW defect and substitutional atoms (boron and nitrogen),
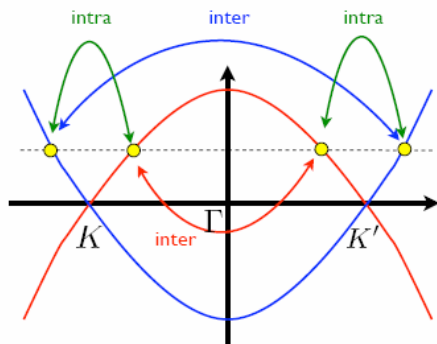

Figure 1.9: *a) Possible scattering channels for a metallic SWNT with short-range impurities.*
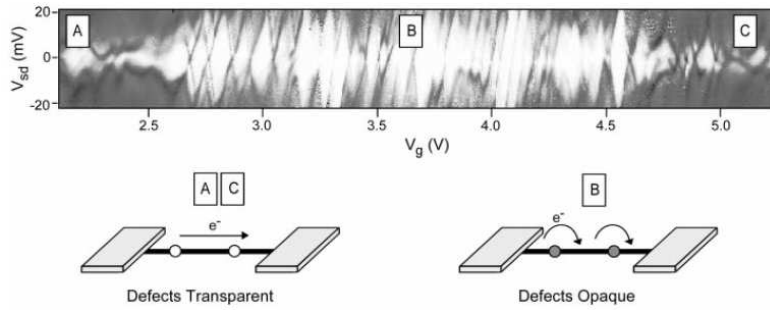
Figure 1.10: *Defect induced intratube quantum dot within a 250 nm long metallic SWNT at $T = 4$ K in a source-drain-gate configuration. The gray-scale plot with white corresponding to zero conductance of the differential conductance $dI/dV_{sd}(V_g, V_{sd})$ shows Coulomb blockade patterns in the gate voltage zone B. The defects appears to be transparent in regions A and C. Taken from [52].*

due to symmetry arguments. However, resonant backscattering of electrons at energies corresponding to defect-induced states in the LDOS result in a decrease in the conductivity of about 1 G_0 at these energies. In contrast, the same calculations for a vacancy and a double vacancy show backscattering around E_F.

A direct experimental verification of these theoretical findings is highly challenging, as one must be able to probe the atomic-scale nature of the defect and to correlate it unambiguously with the observed transport properties. A first step in this direction can be done by means of scanning gate microscopy (SGM) where a biased tip is scanned at fixed height over a SWNT portion between source and drain contacts. The local Fermi level of the tube is shifted due to the local charge accumulation near the tip and thus a map of the variations in the conductance of a device can be established. In the experiment presented in Fig. 1.10, SGM investigations revealed the presence of two scattering centers separated by about 120 nm in a 250 nm long metallic SWNT embedded in a source-drain-gate configuration. The gray-scaled plot of the source drain differential conductance in Fig. 1.10 shows typical Coulomb blockade patterns within a certain gate voltage range and normal conduction besides. This result indicates that the defects in the metallic nanotube define an intratube quantum dot constituted by gate-tunable electron scatterers. This behavior is shown to be due to resonant backscattering.

In a more recent work illustrated in Fig. 1.11, the authors combined both methods of selective electrochemical deposition (SED) and scanning gate microscopy (SGM) to localize and characterize the effects of intrinsic
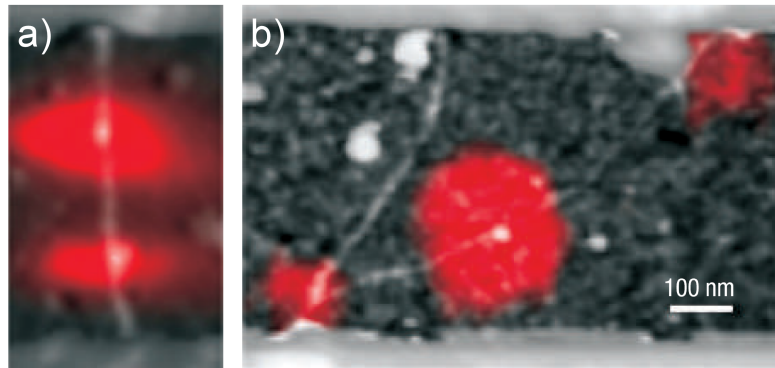
Figure 1.11: *a) Composite image of SGM and noncontact AFM on a metallic SWNT with two defect sites made visible by means of SED between contacts. b) The same for a semiconducting (on the right hand) SWNT with a single defect site in the middle. The SGM spots at both extremities of the tube correspond to Schottky barriers. Taken from [53].*

defects on the transport properties of metallic and semiconducting SWNTs. Figure 1.11 a) shows that the entire effect of gating is localized at two positions along a metallic SWNT. These spots constitute electronic defects in the sense that they disproportionately contribute to the two-terminal transconductance dI/dV_{g} of the device. Subsequent SED testing localizes the position of two chemically reactive defect sites at the same position than the SGM spots. A similar result is obtained in Fig. 1.11 b) where the position of a single defect in the middle of the SWNT is localized by both methods. Note that because of the presence of SGM spots at the contact junctions which can be attributed to Schottky barriers, this tube has been assigned as a semiconducting SWNT. Both examples show transistor-like behavior due, at least in part, to the presence of locally sensitive sites.

In both experiments described above, the nature of the defects could not be identified. Nevertheless, these two findings clearly indicate that SWNT-based electronic devices can be strongly influenced and possibly controlled by the introduction of specific defects.

Chapter 2

Experimental Methods

2.1   Scanning Tunneling Microscopy

Scanning tunneling microscopy (STM) is the only probing technique that allows the investigation of both the topography and the electronic structure of individual objects down to the sub-nanometer scale. STM therefore constitutes the ideal tool for our study of the local modifications of the electronic structure of SWNTs induced by different kind of defects. The basic functioning of a typical STM setup and a theoretical basis to scanning tunneling microscopy and spectroscopy (STM/STS) will be introduced in sections 2.1.1 and 2.1.2. An extensive introduction to STM and STS can however be found in textbooks like [54]. The low temperature UHV STM (LT-STM) used in this work will be described in section 2.3.

2.1.1   General principle of operation

STM is based on the quantum mechanical tunneling of electrons between a metallic, atomically sharp tip and a conductive sample by applying a bias voltage between them. This effect allows us to have a control signal (the tunneling current) related to the relative distance of the tip to the sample, without having physical contact, which means without exerting forces on the sample leading to significant structural changes. STM was developed by G. Binnig and H. Rohrer at the IBM research labs in Zürich in 1981 [55], which was rewarded with the Nobel Prize in physics in 1986. In the so-called constant current mode used throughout this work, the tunneling current is kept constant by means of a feedback loop whose output signal adjusts the vertical z-position of the tip as a function of the $x - y$ position. Here the $x - y$ plane corresponds roughly to the sample surface plane. The x, y and z movements of the tip are realized by means of piezoelectric actuators. The recorded signal $z(x, y)$ reflects a constant current contour map, which can

be interpreted in a first approximation as the topography of the sample.

2.1.2 Theoretical principles

2.1.2.1 One-dimensional tunneling

The electron tunneling between the tip and the sample can be described in a first approximation by a time independent one-dimensional model. The simple case of the tunneling of a single electron through a rectangular shaped potential barrier is treated in quantum mechanics basic textbooks (*e.g.* [56]). Solving the Schrödinger equation for an incoming plane wave $\Psi = e^{ikx}$ results in a transmission coefficient T:

$$T = \frac{4k^2\kappa^2 sinh(\kappa z)}{1 + (k^2 + \kappa^2)^2} \tag{2.1}$$

where z is the barrier width (tip-sample distance), $k = \sqrt{2mE/\hbar^2}$ is the wave vector of the electron and κ is given by $\kappa = \sqrt{2m(V_0 - E)/\hbar^2}$, where $V_0 - E$ is the effective barrier height for an electron with kinetic energy E. For barrier height and width satisfying $\kappa z >> 1$, the last expression can be rewritten as:

$$T \approx \frac{16k^2\kappa^2}{(k^2 + \kappa^2)^2} \cdot e^{-2\kappa z} \tag{2.2}$$

The exponential dependence of the transmission coefficient T is responsible for the high z-resolution of STM. Indeed, it can be shown that for typical barrier heights $V_0 - E$ of a few eV, a variation in z by 1 Å results in a variation in T by about one order of magnitude.

2.1.2.2 Perturbation theory

Although it already gives the exponential dependence on the tip-sample distance of T, which is characteristic for STM, the above described simple one-dimensional model is not sufficient to describe the tunneling of electrons in a three-dimensional tip-sample system. In 1961, J. Bardeen proposed a more detailed model based on time-dependent perturbation theory [57]. He considered the tip and sample as two separated and independent systems whose electronic structure is given by the eigenstates ψ_μ^t and ψ_ν^s with their eigenvalues E_μ^t and E_ν^s. Note that Bardeen performed the original calculations for tunneling between two arbitrary surfaces. The labels t and s for tip and sample are used here because of the application to STM. By solving the time-dependent Schrödinger equation and considering small perturbations and elastic tunneling (energy conservation) the application of the Fermis
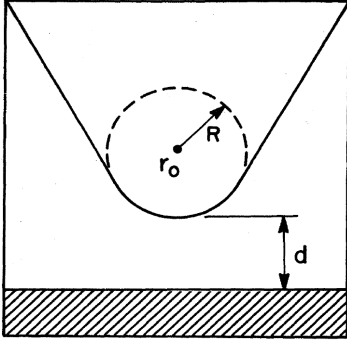
Figure 2.1: *Schematics of the tunneling geometry in the Tersoff-Hamann model. The probe tip is assumed to be locally spherical with radius of curvature R. The tip-sample (dashed) distance is d and the center of curvature of the tip is given by the vector $\vec{r}_0$. Taken from [58].*

"golden rule" results in the following expression for the tunneling current I_{t}:

$$
\begin{aligned}
I_{\mathrm{t}} = \frac{2\pi e}{\hbar} \sum_{\mu,\nu} & \left\{ f\left(E_\mu^t\right)\left[1 - f\left(E_\nu^s + eU\right)\right] \right. \\
& \left. - f\left(E_\nu^s + eU\right)\left[1 - f\left(E_\mu^t\right)\right] \right\} \\
& \cdot |M_{\mu\nu}|^2 \cdot \delta\left(E_\mu^t - E_\nu^s\right)
\end{aligned}
\tag{2.3}
$$

where $f(E)$ is the Fermi-Dirac distribution, U is the applied sample bias voltage, $M_{\mu\nu}$ is the tunneling matrix element between the unperturbed electronic states ψ_μ^t of the tip and ψ_ν^s of the sample surface. The delta function describes the conservation of energy for the case of elastic tunneling. According to Bardeen, the tunneling matrix element is given by the integral of the current operator:

$$
M_{\mu\nu} = -\frac{\hbar^2}{2m} \int \left[\left(\psi_\mu^t\right)^* \nabla \psi_\nu^s - \psi_\nu^s \nabla \left(\psi_\nu^s\right)^* \right] d\vec{S}
\tag{2.4}
$$

where the integral has to be evaluated over any surface lying entirely within the vacuum barrier region separating the two electrodes. To derive the matrix element $M_{\mu\nu}$ from Eq. 2.4, explicit expressions for ψ_μ^t and ψ_ν^s are required. In real experiments, as opposed to theoretical simulations, the generally unknown atomic structure of the tip constitutes maybe the most important obstacle to get a full knowledge of $M_{\mu\nu}$.

Tersoff and Hamann [58] used the simplest possible model for the tip with a local spherical symmetry, see Fig. 2.1. In this model, $M_{\mu\nu}$ is evaluated for an s-type tip wave function. They considered the limits of low temperature and small applied bias for which the expression of the tunneling current

becomes:

$$I_{\text{t}} = \frac{2\pi e^2}{\hbar} U \sum_{\mu,\nu} |M_{\mu\nu}|^2 \, \delta\left(E_\nu^s - E_F\right) \cdot \delta\left(E_\mu^s - E_F\right) \qquad (2.5)$$

Finally, within the s-wave approximation for the tip, the following expression for the tunneling current can be obtained:

$$I_{\text{t}} \propto U \cdot \rho_t\left(E_F\right) \cdot e^{2\kappa R} \cdot \sum_\nu |\psi_\nu^s\left(\vec{r_0}\right)|^2 \, \delta\left(E_\nu^s - E_F\right) \qquad (2.6)$$

with $\rho_t\left(E_F\right)$ the density of states at the Fermi level for the tip, R is the effective tip radius, $\vec{r_0}$ is the center of curvature of the tip. The decay rate κ is given in Eq. 2.1. The quantity

$$\rho_s(\vec{r_0}, E_F) = \sum_\nu |\psi_\nu\left(\vec{r_0}\right)|^2 \, \delta\left(E_\nu^s - E_F\right) \qquad (2.7)$$

can be identified as the surface local density of states (LDOS) at the Fermi level E_F, *i.e.* the charge density from electronic states at E_F , evaluated at the center of the effective tip. Eq. 2.6 is no longer valid for high bias [54]. Therefore, in a first approximation, if U is increased, the voltage dependence of the tip and sample has to be considered and the tunneling current is given by a convolution over energy:

$$I_{\text{t}} \propto \int_0^{eU} \rho_t\left(E - eU\right) \cdot \rho_s\left(x, y, z = 0, E\right) \cdot T\left(E, eU, z = d + R\right) dE \quad (2.8)$$

where T is the transmission coefficient which can be estimated within the WKB approximation:

$$T\left(E, eU, z\right) = e^{-2z\sqrt{\frac{2m}{\hbar^2}\left(\frac{\phi_t + \phi_s}{2} + \frac{eU}{2} - E\right)}} \qquad (2.9)$$

where ϕ_t and ϕ_s are the work functions of the tip and sample, respectively. Finally, we can write the expression for the tunneling current:

$$I_{\text{t}} \propto \int_0^{eU} \rho_t\left(E - eU\right) \cdot \rho_s\left(x, y, E\right) \cdot T\left(E, eU, z\right) dE \qquad (2.10)$$

This last relation is illustrated in the simplified one-dimensional potential energy diagram at zero temperature in Fig. 2.2. The system consists of the tip (left electrode) and the sample (right electrode) which are separated by a small vacuum gap. For zero applied bias (Fig. 2.2 a)), the Fermi levels of both tip and sample are aligned at equilibrium. When a bias voltage
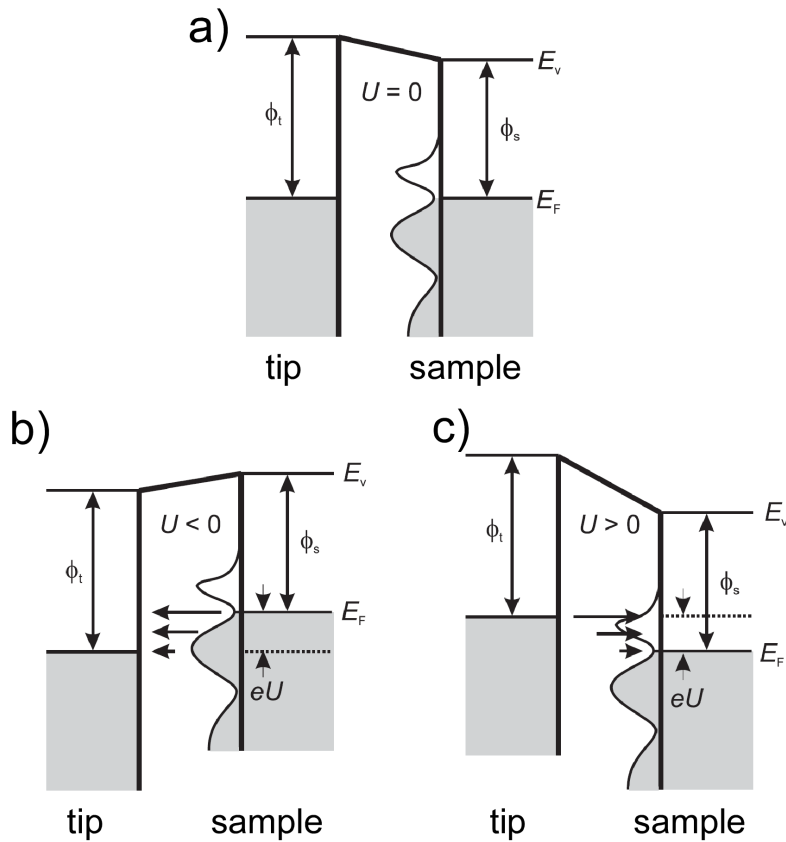
Figure 2.2: *Simplified one-dimensional potential energy diagram at zero temperature for the tip-vacuum-sample system. a) For zero applied bias , the Fermi levels of both tip and sample are aligned at equilibrium. When a bias voltage V is applied to the sample, the main consequence is a rigid shift of the energy levels upward or downward in energy by an amount $e\,|U|$, depending on whether the polarity is negative (b)) or positive (c)). Taken from [59]*

U is applied to the sample, the main consequence is a rigid shift of the energy levels upward or downward in energy by an amount $e\,|U|$, depending on whether the polarity is negative (Fig. 2.2 b)) or positive (Fig. 2.2 c)). Consequently, the bias polarity determines whether unoccupied or occupied sample electronic states are probed.

2.2   Scanning tunneling spectroscopy

The quantity we are interested in to study is the electronic structure of the sample is $\rho_s(x, y, E)$, *i.e.* the LDOS of the sample as a function of the position an energy. Formally, a direct access to $\rho_s(x, y, E)$ is obtained by differentiating Eq. 2.10:

$$
\frac{dI_{\mathrm t}}{dU} \propto e \cdot \rho_t(0) \cdot \rho_s(x, y, E = eU) \cdot T(E = eU, eU, z)
$$
$$
+ \int_0^{eU} \rho_t(E - eU) \cdot \rho_s(x, y, E) \cdot \frac{dT(E, eU, z)}{dU} dE
$$
$$
+ \int_0^{eV} \frac{d\rho_t(E - eU)}{dU} \cdot \rho_s(x, y, E) \cdot T(E, eU, z) dE \tag{2.11}
$$

Generally, one usually neglects the third term by considering a constant DOS of the tip. The second term can be neglected at low biases. We will however see in chapter 7 that this term has to be taken into account for special cases. Thus, as a first approximation one obtains:

$$
\frac{dI_{\mathrm t}}{dU} \propto e \cdot \rho_t(0) \cdot \rho_s(x, y, E = eU) \cdot T(E = eU, eU, z) \tag{2.12}
$$

The important point is that $dI_{\mathrm t}/dU$ is proportional to the LDOS of the sample. The effects of the proportionality to the energy dependence of T will be discussed in detail in chapters 4 and 7. Experimentally, a dI/dU spectrum is obtained by differentiating a I-U curve recorded at a specific spatial location. For this, the tip is positioned above the surface with the setpoint parameters $I_{\mathrm s}$ and $U_{\mathrm s}$. Then the feedback loop is switched off and the bias voltage is ramped from an initial value to a final value. Meanwhile the tunnel current is acquired with a constant z-position. A direct experimental access to dI/dU is possible within the so-called lock-in technique where a lock-in amplifier adds a small AC component $V_{\mathrm{mod}} \cdot cos(\omega t)$ to the DC bias voltage $U_{\mathrm s}$ and the resulting in-phase modulation of the tunneling current is recorded. The frequency of the AC component must exceed the dynamic regulation range of the piezo-driver and is usually set to about 600 Hz in this work. Formally, the in-phase modulation of the tunneling current can be expanded around U as:

$$
I_{\mathrm t}(U) = I_{\mathrm t}(U_{\mathrm s}) + \frac{dI}{dU} \cdot U_{\mathrm{mod}} cos(\omega t) + \frac{d^2 I}{dU^2} \cdot \frac{(U_{\mathrm{mod}} cos(\omega t))^2}{dU^2} + ... \tag{2.13}
$$

$$
\{a\} \tag{2.14}
$$

To select the second term proportional to the wanted quantity dI_t/dU out of the total current, the lock-in amplifier applies a narrow bandpass filter centered at ω. Thus, the dI_t/dU signal can be measured with high accuracy in addition to I_t. Note that for practical applications the measured dI_t/dU systematically contains an offset due to capacitive contributions (cabling and electronic circuitry). This undesired offset can be easily removed by means of comparison with a numerical differentiation of the original *I-U* curve.

2.3 LT-STM setup

The STM setup used in this work is commercial Omicron^{TM} LT-STM. It is mostly operated at a temperature of about 5 K (liquid helium cooling) or 77 K (liquid nitrogen cooling) and in ultra high vacuum (UHV) with a base pressure below 10^{-10} mbar. An efficient thermal shielding concept together with the fact that the whole STM stage (including the vibration isolation elements) is kept at sample temperature results in an outstanding thermal stability (drift $\sim$ 0.3 nm/day at 5 K). The instrument achieves a z-stability in the range of 1 pm allowing high resolution topographic imaging. STM topography images are recorded in the constant current mode. The excellent z-stability is further very beneficial to perform top quality tunneling spectroscopy, which we perform using a lock-in technique (Stanford Research Systems SR 830). The sample bias is the potential difference of the sample with respect to the tip (sample grounded). For all the STM/STS experiments cited in this work, we used tips mechanically cut from a Pt(20%)Ir(80%) wire ($\varnothing$ 0.38 mm), where the metallic nature of the tips was regularly checked on the conductive substrate.

Attached to the STM analysis chamber we have an autonomous vacuum chamber in which the sample preparation can be performed. Specifically for this work, we have a sputter gun and an electron cyclotron resonance (ECR) plasma source attached on different ports of the preparation chamber.

2.4 Atomic Force Microscopy

The atomic force microscope (AFM) is another member of the scanning probe microscopy (SPM) family. This technique was developed in 1986 by Binning, Quate, and Gerber as a collaboration between IBM and Stanford University [60].

In this work, AFM has been used to characterize SWNT suspensions, therefore only a brief introduction will be given in this paragraph. Detailed introductions to AFM can be found in textbooks like [54] or in a more recent
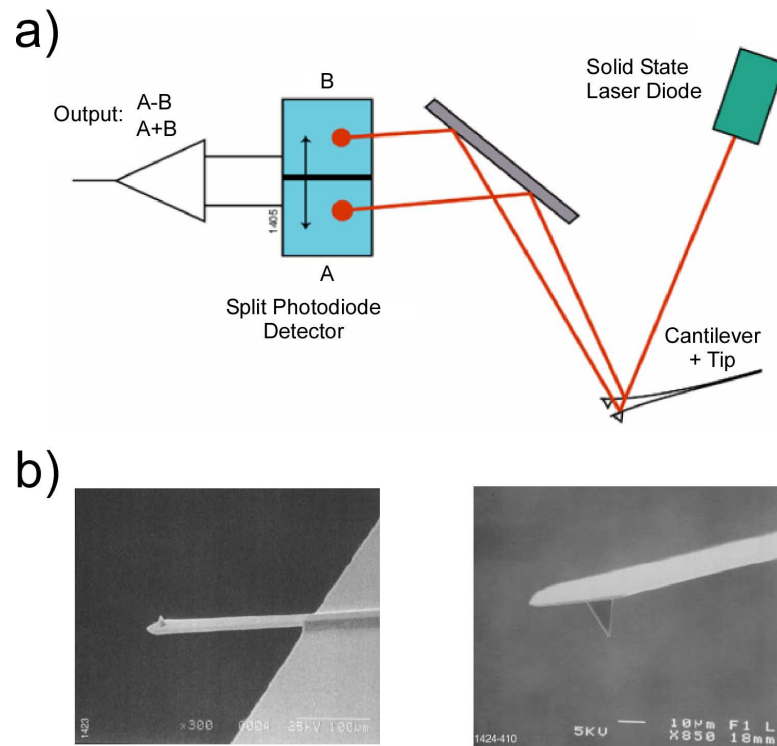
Figure 2.3: *a) AFM beam deflection detection scheme, b) Scanned Electron Microscope (SEM) images of silicon cantilever and tip. Taken from [62]*

review article [61].

The key element of AFM (at least of the standard versions) is a sharp tip which is attached to a stiff cantilever. A typical silicon cantilever with its tip can be seen in Fig. 2.3 b). Whereas in STM the tip-sample tunneling current is measured, in AFM it is the force between the scanning tip and the sample which is detected. Thus, AFM is also operable on insulating surfaces, contrary to STM. In the most basic operating mode, the force can be detected by measuring the static deflection of the cantilever according to Hook's law. Here the cantilever displacement is measured by monitoring the force-induced deflection of a laser beam reflected by the rear side of the cantilever with a split photodiode detector, as shown in Fig. 2.3 a). AFM can operate with three different imaging modes: contact, non-contact and tapping mode. In this thesis, only the latter mode has been used and will be described.

In tapping mode AFM, the cantilever is oscillated at or near its resonance frequency. When the tip is brought into contact with the sample surface, the amplitude of the oscillation is reduced. The feedback loop maintains a constant RMS value of the oscillation signal acquired by the split photodiode detector by adjusting the tip height. Thus a topographic image of the sample surface can be formed by storing the vertical position of the scanner at each (x, y) coordinate. The tip is only intermittently in contact with the sample, resulting in strongly attenuated lateral forces acting on the sample during scanning, in contrast to contact mode AFM. This enables one to image individual SWNTs lying on a surface without moving them.

For the characterization of our SWNT suspensions (see chapter 3), we used a commercial Nanoscope III AFM operating in air.

2.5 Cold plasmas

The local modifications of the electronic structure of SWNTs we want to study are induced by structural defects generated by means of cold plasma treatment of the tubes. A short introduction to plasma physics with an emphasis on two kind of cold plasmas we used in this work, *i.e.* ECR plasma and DC glow discharge will be given in this section. An extensive introduction to cold plasmas and their applications are found in textbooks like [63, 64].

A plasma can be defined as a *quasi-neutral gas* of charged and neutral particles characterized by a collective behavior and constitutes the fourth state of the matter, apart from the solid, liquid, and gas state. A plasma is usually obtained when sufficient energy, higher than the ionization energy, is supplied to the gas atoms. This can be achieved by an electrical discharge through the gas, causing ionization and production of ions, electrons and excited atoms or molecules. Parallel and concomitant to the ionization occurs the opposite process of recombination of electrons with ions to form neutral atoms or molecules. The motion of the particles in a plasma can cause local concentrations of positive and negative charges giving rise to long-ranged Coulombic fields that affect the motion of charged particles far away from the charge concentration. This constitutes the origin of the characteristic collective behavior of a plasma. The local concentrations of charges are confined to volumes of small dimensions typically of orders of tens of micrometers. Outside of these small volumes, the charge density of the ions is equal to the density of electrons, making the plasma electrically neutral. These local concentrations are characterized by the so-called Debye

length λ_D:

$$\lambda_D = \left(\frac{\epsilon_0 k_B T_e}{n_e e^2} \right)^{1/2} \tag{2.15}$$

where ϵ_0 is the permittivity of the free space, k_B the Boltzmann constant, n_e is the electron density (which is equal to the ion density n_i in the quasi-neutral state of the plasma) and T_e is a key plasma parameter called electron temperature. The temperature represents the mean kinetic energy of the particles in a neutral gas in thermodynamic equilibrium. A plasma can be principally characterized by the ion and electron temperatures, T_i and T_e, among other temperatures corresponding to different energies in play in the plasma. All these temperatures must be equal to reach a complete thermodynamic equilibrium (CTE). CTE plasma can only exist in stars or during the short interval of a strong explosion. In certain laboratory conditions, it is possible to achieve local thermodynamic equilibrium (LTE). In low pressure plasmas used in this work, the LTE conditions are generally not achieved and these plasma are therefore called non-LTE plasmas. In the non-LTE plasmas, the temperature of the electrons is much higher than that of the heavy particles and $T_e >> T_i > T_g$, with T_g being the temperature of the gas. The electrons can reach temperatures of 10^4-10^5 K (1-10 eV), while T_g can be as low as room temperature. Therefore, such plasmas are called *cold plasmas*. It can be shown that a plasma is always at a positive potential relative to any surface in contact with it. Because of the so-called Debye shielding effect, the potential developed between the surface and the plasma bulk is confined to a layer of thickness of several Debye lengths called plasma sheath. Because of concentration gradients, the plasma particles tend to move by diffusion toward regions of lower density. It can be shown that the flux of electrons is equal to the flux of the ions.

The cold plasmas have been developed specifically and purposefully based on their nonequilibrium properties and their capabilities to cause physical and chemical reactions with the gas at relatively low temperatures. Applications are widespread and put to use in a variety of fields, from microelectronic fabrication to surface hardening of metals.

2.5.1   DC glow discharge

A DC glow discharge is produced by applying a DC voltage from a high-impedance power supply between two conductive electrodes (anode and cathode) inserted into a gas at low pressure of the order of the mbar. As the voltage is gradually increased, an electron multiplication process takes place due to the ionization of the gas by collisions between accelerated electrons and atoms or molecules of the gas. The current increases steadily while the voltage reaches a limit determined by the output impedance of the

power supply (Townsend discharge). When the applied voltage reaches a certain threshold value, an avalanche process occurs mainly as a result of the emission of secondary electrons from the collision of ions with the cathode. In parallel, electrons are removed from the plasma by drift and diffusion to the walls by recombination with positive ions. When the number of electrons is sufficient to produce just enough ions to regenerate the number of lost electrons, a steady state is reached in which an equilibrium is established between the rate of formation of ions and the rate of their recombination with electrons. At this stage the discharge is self-sustaining. Extensive breakdown occurs in the gas and the glow discharge is thus established. The breakdown voltage is determined by Paschen's law:

$$V_{\mathrm{b}} = \frac{C_1(pd)}{C_2 + ln(pd)} \tag{2.16}$$

where d is the distance between electrodes, p the pressure in the chamber and C_1, C_2 are constants depending on the nature of the gas. Then the gas begins to glow, the voltage drops, and the current raises abruptly. The mode of the discharge at this point is called the normal glow, which is used in our work. Further increase of the power will lead to abnormal discharge where the discharge spreads to cover the whole surface of the cathode. A further increase in power will lead to an arc discharge accompanied with a decreasing of the voltage. The plasma potential continuously decrease between the anode towards the cathode, with a substantial drop at the cathode, called the cathode fall. This cathode fall is a function of the material used for the cathode and the nature of the discharge gas.

2.5.2 ECR plasmas

When an alternating field is applied between the two electrodes, each of them acts alternately as cathode or anode. If this frequency is high enough, the ions created near a momentary anode cannot reach the cathode before the field is reversed. At such frequencies the positive space charge is partly retained between between the two half cycles of the alternating electric field and facilitates the reinitiation of the discharge. If frequencies are in the range from 500 kHz to several MHz, high-frequency discharges are called radio frequency discharges (RF). A RF discharge is more efficient than the DC discharge in promoting ionization and sustaining the discharge. Electron cyclotron resonance (ECR) plasmas we used in this work operates at a microwave frequency of 2.45 GHz (frequency commonly used in industrial applications). The main difference of an ECR plasma with a RF plasma is the additional application of a magnetic field to the plasma system. Under this condition, the charged particles are subjected to a gyromotion around

the magnetic field lines with a radius r_L and an angular frequency ω_c. The radius r_L is called the Larmor radius and is given by:

$$r_L = \frac{mv_\perp}{eB} \tag{2.17}$$

where m is the mass of the charged particle and $v_\perp$ is the velocity component of particle, normal to the magnetic field line. The frequency ω_c is called the cyclotron angular frequency and is given by:

$$\omega_c = \frac{eB}{m} \tag{2.18}$$

For a magnetic field of 875 gauss, the cyclotron frequency of the electrons with $m = m_e$ becomes 2.45 GHz, and if microwaves of frequency ω=2.45 GHz are used to excite and sustain the plasma, the gyromotion of the electrons is in resonance with the microwaves. This is called the electron cyclotron resonance condition, and a plasma excited under these conditions is called an ECR plasma. ECR plasmas have the capability to operate at lower pressures than RF plasmas and to create higher plasma densities.

Chapter 3

Sample preparation

The explanatory power of a physical experiment is fundamentally related to the perfection of the sample under investigation. In this respect STM studies are of no exception, especially if one is interested in the investigation of specific quantum phenomena emerging at the atomic scale. For our work the idealized basis sample would consist of a dispersion of individual, defect free SWNTs with appropriate density on an atomically flat and inert substrate. Inert means in this context that the interaction of the substrate with the nanotubes does not substantially alter their electronic structure.

3.1   SWNT suspension

A first condition for the sample preparation is given by the LT-STM setup which requires an appropriate density of nanotubes on the sample surface since the scan range at low temperature (~ 5 K) is limited to 1 μm^2. Therefore, in order to routinely address different individual SWNTs within a convenient time interval, the required surface density of individual SWNTs should be equal to about one to ten nanotubes per 1 μm^2. The length distribution of the nanotubes also influences the ideal density as the longer the tubes are, the fewer one needs.

High quality STS requires a sharp, metallic and stable tip. Contaminations of the tip, e.g. by undesirable impurities in the SWNT raw material, like catalytic particles or amorphous graphite residua, will ultimately lead to changes of the tip and therefore changes in the STS spectra. Therefore, highest quality SWNT raw material is required. Professor Smalley's group (Rice University, Houston, USA) kindly provided us with SWNT raw material (batch HPR 122.1) produced by the HiPco process. The as-produced SWNT material has undergone a multistage purification process based on metal catalyzed oxidation [9]. The flake-like raw material is shown in Fig. 3.1 a).

Because of their very large length to diameter ratio, SWNTs easily form bundles due to van-der-Waals interactions. In order to study individual tubes, a technique which is able to unravel the bundles and deposit them individually on a flat conductive surface is required. In our case it is especially important that this procedure does not introduce a high density of defects, as it is our purpose to specifically create defects by ion bombardment and investigate them.

Several approaches of unbundling the SWNTs by sonication in a solvent and subsequent drop casting on the desired substrate have been proposed in the literature. In the case of aqueous suspensions, agents preventing reaggregation are required, where fatty acids [65], functionalized polymers [66] and even DNA [67] have been used . All these approaches have the main disadvantage to leave residues of the surfactant on the tube after dropcasting and evaporation of the solvent. In our case, an additional step to remove these residues would be required. Therefore we opted for a suspension without surfactants.

In accordance with many reported STM experiments (and some transport experiments) on carbon nanotubes [25], we found the best results using 1,2-dichloroethane (DCE). Because of the non-polar nature of this organic solvent, the hydrophobic SWNTs can be well dispersed, due to the "like dissolves like" principle [68]. A suitable SWNT suspension is obtained by introducing a flake (~ 50 μg) of raw material in a vial containing 1 ml of DCE. A sonication treatment for about two to three hours in a commercial ultrasonic cleaner (Bandelin Sonorex^{TM}) is carried out, resulting in a stable gray suspension. Fig. 3.1 b) shows a typical SWNT suspension after sonication, contained in a 10 mm inner diameter vial. For each preparation run, the dropcasting procedure has been calibrated by essays on freshly cleaved mica, which have been subsequently characterized by means of tapping mode atomic force microscopy (tmAFM) using a commercial
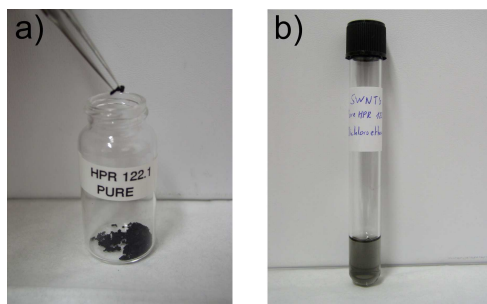

Figure 3.1: *Preparation of the SWNT suspension. a) Highly purified HiPco SWNT flake-like raw material. b) SWNT suspension in 1 ml of 1,2-dichloroethane, with a well-adapted density after about three hours of sonication time. Inner diameter of the vial: 10 mm.*

Nanoscope III instrument from Digital Instruments^{TM}.

An efficient way to obtain a suitable SWNT density on the mica surface is to blow off a suspension droplet deposited from a glass pipette after a few seconds by a nitrogen gas stream. This step must be done shortly after the end of the sonication treatment to avoid a possible reaggregation of the SWNTs. Figure 3.2 displays tmAFM images of optimally dispersed SWNTs on freshly cleaved mica. The sonication times in a) and b) are three and four hours respectively. Note that individual tubes have been already observed after a sonication time of only one hour, but we found the best individual tubes to bundles ratio for about three hours of sonication (see section 3.3). Using the same suspension, the resulting surface density of SWNTs is very sensitive to the time elapsed (generally 1-2 seconds) between the deposition of a droplet on mica and the nitrogen dry blow. This is illustrated in Fig. 3.2, where both depositions have been performed from the same suspension (sonication times are three and four hours for a) and b), respectively). The tube density in Fig. 3.2 a) is markedly higher than in b), by about a factor of two. The tube density can show considerable variations over the whole sample surface ($1 \ cm^2$) due to the uneven spreading of the suspension droplet under nitrogen dry blown. SWNT loops like in Fig. 3.2 a) (black arrows) or rings like in the upper part of b) have been regularly observed. The formation of such structures are a result of van-der-Waals attachment of a single tube or a bundle of tubes to itself [69–72].
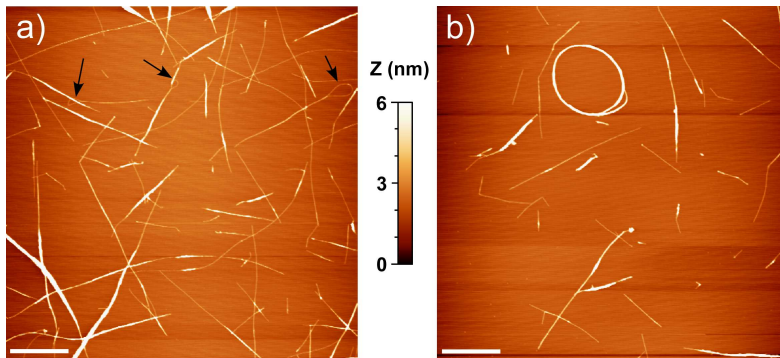

Figure 3.2: *tmAFM images of a dispersion on freshly cleaved mica of highly purified SWNTs from a suspension in DCE, after blowing the suspension droplet with nitrogen. Sonication times are three hours for a) and four hours for b). Black arrows in a) indicate the position of SWNT loops. Scale bar in a) and b): 500 nm*

3.2   HiPco SWNT diameter and length distribution

A statistical analysis of the length and diameter distributions of SWNTs has been performed, where diameters and lengths of SWNTs have been measured on nine different regions (3 μm $\times$ 3 μm) on the same sample by means of tmAFM imaging. Here the suspension has been sonicated for three hours. It is difficult and often impossible to distinguish between individual SWNTs and small bundles of two or three tubes from tmAFM images, due to the limited lateral resolution. Moreover, it is known that tmAFM on SWNTs always yields height values slightly smaller than the effective tube diameter because of deformation of the tube by the tip, as a function of the drive amplitude [70]. In spite of these drawbacks, this method has been judged adequate to get a preliminary characterization of our SWNTs batch. The measured diameter and length distributions are reported in Fig. 3.3 a) and b) respectively.

One can observe from Fig. 3.3 a) that the majority of the tube diameters falls in a range between 0.6 nm and 1.6 nm with a peak occurence between 0.9 nm and 1.1 nm. Transmission electron microscopy (TEM) [9], Raman spectroscopy and X-Ray photoelectron spectroscopy investigations of HiPco SWNTs [73] report diameters between 0.6 nm and 1.4 nm. Taking into account the effects cited above (tapping deformation estimated to be at least 0.1 nm), we considered that measured heights larger than 1.3 nm correspond to bundles with more than three tubes (triangular configuration). Based on these conservative assumptions, we could assign about 40% of the observed structures to be either individual SWNTs or small bundles with two or three tubes.
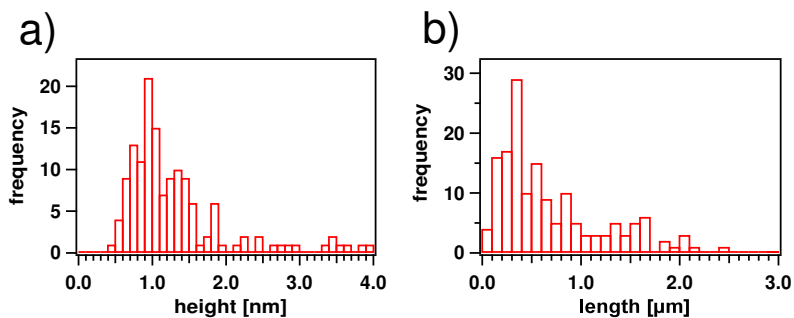

Figure 3.3: *a) Apparent height distribution of SWNTs deposited by dropcasting on mica based on tmAFM imaging at nine different area locations on the same sample. The suspension was sonicated for three hours. b) SWNTs length distribution.*

The SWNT length distribution ranges between 100 nm and about 2 μm, with a maximum probability around 300-400 nm, in good agreement with earlier reported tmAFM characterizations of HiPco SWNTs [68].

It should be noted that no significant variations in the diameter and length distributions have been observed for sonication times between two and six hours. This indicates that the used sonication power is sufficiently low to avoid significant fracturing of the SWNTs. Nevertheless we deemed it important to keep the sonication time as short as possible in order to decrease the risk of introducing defects in the nanotubes.

Based on the diameter distribution and tight binding calculations, values for the bandgap energies of semiconducting SWNTs can be estimated to predominantly lie between about 0.8 eV and 1.2 eV.

3.3 Preparation of gold substrates

Conductive, inert and atomically flat surfaces are a prerequisite for our studies. As the SWNTs are deposited under ambient conditions, these requirements restrict the choice to substrates where oxidation in air does not occur. Actually, only gold and graphite satisfy these requirements. Gold was chosen for the offered advantage that the tip can be quite easily conditioned by means of indentations in the surface. We used commercial gold on glass substrates from the company Arrandee^{TM}. A special borosilicate glass (1.1 mm thickness and 11 mm $\times$ 11 mm in surface) is covered by a thin adhesive chromium layer (2.5$\pm$1.5 nm) and a final 250$\pm$50 nm thick amorphous gold film [74]. First sample preparations by flame annealing with a hydrogen or butane-propane torch (as suggested by Arrandee) were not satisfactory. Although large atomic terraces could be obtained, tmAFM analysis of the flame annealed surface revealed the presence of a large number of small (2-10 nm in height) dot-like features, most probably due to diffusion of chromium from the adhesive layer through the gold layer during the too high temperature flame treatment ($\sim$ 2000°C). The presence of these dots is not acceptable for our purpose since undesirable effects like inhomogeneous charge transfer from the SWNTs to the substrate can occur due to a quite large difference in work functions for gold and chromium ($\Delta\phi \approx 0.9$ eV). The quality of the gold surface has been dramatically improved with a fist gentle ex-situ hydrogen flame annealing (without letting the sample become red) followed by several in-situ argon ion sputtering and heating cycles in the UHV preparation chamber of the LT-STM. The general process consists in three cycles with sputtering times of forty, twenty and finally ten minutes, with each sputtering cycle followed by a five minute annealing at 420°C. For the first two sputtering cycles, the acceleration po-

tential has been set to 1.5 keV, and 1 keV for the last ten minute cycle. The surface temperature has been measured with a IR one-color pyrometer (Raytek Marathon-MA2) with the emissivity tuned on the value $\epsilon = 0.1$. The result of this procedure shows flat monoatomically terraces with sizes between 100 nm^2 to 2000 nm^2, where the typical herringbone reconstruction for Au(111) is regularly observed.

The SWNTs deposition on the well-prepared gold surface has been performed ex-situ, following the same procedure as described above for mica samples. Immediately after the SWNT deposition, the samples are reintroduced in the preparation chamber. Prior to the STM/STS analysis, a last annealing to 390°C for a few minutes is carried out in order to remove the major part of contaminants coming from both DCE and exposure to air.

3.4   STM/STS characterization of the samples

3.4.1   Quality of the surface

Within the variability of the nanotube density inherent to the deposition procedure, differences between the distribution of tubes for the gold and the mica substrates have been observed even when using the same suspension. Indeed, randomly distributed zones with higher densities of tubes could be observed on the Au(111) surface. This could be an effect of different surface tensions for the DCE-mica and DCE-Au(111) interfaces. However, the presence of individual SWNTs and small bundles (two to three tubes) homogeneously distributed on large areas up to about 500 nm × 500 nm has been routinely observed. The quality of the gold surface has been found to be altered by the presence of solvent residues covering parts or nearly entire terraces or/and step edges, even after the additional annealing procedure described above. An STM image of a typical Au(111) surface after the deposition of SWNTs is shown in Fig. 3.4. The inset shows an apparent height profile recorded along the white dashed line. A corrugation of 1-2 Å is typical and is attributed to assemblies of DCE molecules [36]. Some structures with larger apparent heights up to 4-5 Å and diameters of about 1 nm have also been observed on DCE-covered regions (*e.g.* at position x ≈ 6 nm in the inset). Their exact nature could not be identified and has been attributed to impurities present in the suspension, which might also originate from the CNT raw material and which could not be resolved in tmAFM on mica. The presence of these impurities raises the question whether inhomogeneities in charge transfer might result from local thickness variations of the molecular assemblies. This cannot be ruled out completely as we will discuss later in chapter 4.4.1.2, but the effect is not very pronounced. The STM characterization of our HiPco SWNTs showed a very high purity,
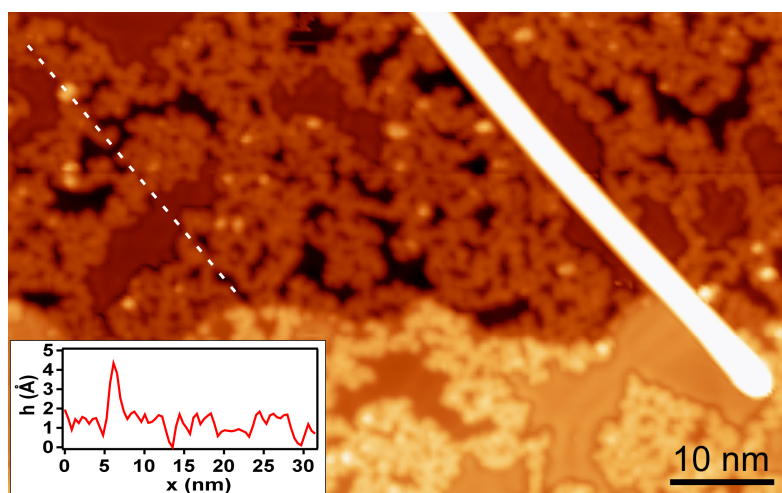
Figure 3.4: *Typical STM image of the gold surface after ex-situ SWNT deposition and in-situ annealing at 390 °C. The full color scale has been limited to the height of the suspension residua (DCE molecules) layers. Inset: Apparent height profile along the white dashed line.*

which means that the SWNTs do not show the residua which are present on the gold surface. Typically, the density of intrinsic defects, which becomes apparent from the topographic imaging are separated by more than 200 nm. From the literature, the presence of intrinsic defects has been reported, but usually very little is known on their exact nature [11, 12, 75].

3.4.2   Chiral assignment of individual SWNTs

The investigation of the modification of the electronic structure induced by defects on a specific SWNT requires that the electronic properties of the pristine tube are known. These are given by the chirality, i.e. the (n,m) indices of the nanotube. Therefore the SWNT assignment is a key issue and can be done by STM/STS measurements. The metallic or semiconducting nature of a given SWNT can already be obtained by a simple measurement of the I-V characteristics. Then the (n, m) indices which fully determine the geometry of a specific SWNT can be obtained experimentally by measuring the chiral angle ϕ between tube axis and zigzag direction from the apparent lattice of the SWNTs, and the diameter d_t from spectroscopy measurements [76, 77]. The practical use of this scheme is however hindered by a number of tip-related effects which can lead to anomalous images of the

hexagonal lattice of SWNTs, *e.g.* multiple tips leading to a superposition of several images (triangular or stripped patterns) [78]. For semiconducting SWNTs, it has been predicted that bandedge states imaged at positive and negative bias can have complementary structures, that is, the superposition of the two images results in a perfect sixfold symmetry, although each image separately breaks the sixfold symmetry (spiral stripes or isolated bonds) [79]. The tube curvature can also distort the hexagonal lattice by overlapping of π-orbitals from neighboring carbon atoms, leading to a triangular pattern for nearly zigzag tubes [80]. These effects can only modulate the contrast of the lattice but do not alter the chiral structure of SWNTs. However, it can be shown that tip-tube convolution effects always lead to a stretching of the hexagonal lattice in the direction perpendicular to the tube axis, by a factor of $(1 + h/r)$ (where r is the tube radius and h the tunneling distance) [80]. The upper panel of Fig. 3.5 a) shows an as measured, high resolution topographic STM image of the hexagonal atomic lattice of a SWNT, where the apparent angle between zigzag and armchair directions is equal to 54.6°. This angle is significantly larger than the expected value of 30°. To recover the real chirality of this tube, we applied the method proposed by Venema et al. [80], where the image is linearly compressed along the direction perpendicular to the tube axis until the angle between zigzag and armchair directions fits to the correct value of 30°. The corrected image can be seen in the lower panel of Fig. 3.5 a). Measurements of the chiral angle ϕ at different locations on the nanotube led to an average value of $\phi = 11.7 \pm 1°$. An error of $\pm 1°$ is typical for this procedure. In this example, the compression factor was 50.5%. This compression factor can vary over a rather large range (10% to 70%), due to different tip structures [80].

In addition to the chiral angle, we need to know the diameter d_t of the SWNT for a complete identification. The most obvious way to determine the real diameter would be to measure the height of the tube from the STM topography image. However, this method appears to be unreliable because it depends on parameters which are difficult to quantify. First, the van-der-Waals distance between the SWNT and the substrate must be known. *ab initio* calculations give a value of about 0.25 nm for an ideal situation where the nanotube is lying on a perfectly flat gold surface [81].
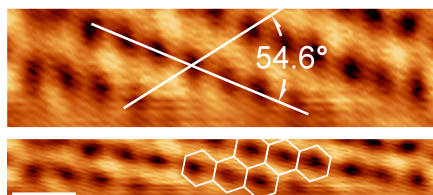

Figure 3.5: *a) Upper panel: topography STM image of a* $(9, 4)$ *SWNT. Lower panel: same image corrected and flattened for better visibility.* $U_s = 1.6$ *V,* $I_s = 0.35$ *nA.*

Then, differences in the electronic structure can lead to different tip-sample distances on the SWNT and on the substrate. Furthermore, it is known that a local mechanical deformation, *i.e.* a compression of the SWNT may arise from forces exerted by the tip on the SWNT during imaging, leading to a lower apparent tube height [80]. A more reliable way to determine the diameter can be obtained from spectroscopy measurements, since the separation between the band edges depends on d_t (and also ϕ for small diameter). In this work, the diameters of semiconducting tubes have been determined from STS measurements which have been compared with tight-binding (TB) calculations taking into account the curvature effects [82].

From spectroscopy measurement, we determined the bandgap of the SWNT displayed in Fig. 3.5 to be $E_g \approx 1.15$ eV. Taking into account the experimentally determined chiral angle $\phi = 11.7 \pm 1°$, we found from the TB calculation that the closest matching tube is a $(9,4)$ SWNT with $\phi = 12.5°$ and $E_g = 0.919$ eV. The difference between calculated and measured bandgap energies could be due to the fact that the TB expression for the calculation of E_g depends on different TB parameters like the hopping integral $V_{pp\pi}$, which has been determined by various experimental and theoretical methods giving values in the range of $V_{pp\pi} = 2.9 \pm 0.2$ eV [80].

In fact, the exact determination of a SWNT is often a difficult task. Indeed, let us consider the following example: assume that we have a semiconducting SWNT with a measured chiral angle $\phi = 10 \pm 1°$. Here two different semiconducting SWNTs can fit this value: $(9,5)$ and $(10,5)$ with $\phi = 9.4°$ and $\phi = 10.9°$, respectively. TB calculation [82] give $E_g = 0.749$ eV and $E_g = 0.788$ eV for $(9,5)$ and $(10,5)$ tubes, respectively. Within the measurement and TB calculation errors discussed above, an exact assignment only based on ϕ and E_g would not be possible in this case. As the electronic structures of both SWNTs examples are quite different, with markedly different positions of the VHS, one should consider higher order VHS in the dI/dV measurement to possibly differentiate them.

In general the assignment of metallic nanotubes is easier since metallic behavior is observed for only one third of all possible (n,m) nanotubes. As for semiconducting tubes, the separation of the bandedges (about 3 times larger than for semiconducting tubes) can be used to determine d_t.

We would like to emphasis at this point that our task is in general not to assign the chiral vector of perfect clean SWNTs, but of tubes exhibiting a relatively high density of defects. This introduces new challenges in (n,m) assignment. First, the presence of defect related electronic states which can lead to a modulation of the band edges can make the determination of E_g difficult. Further, due to scattering of electrons at defects or ends of SWNTs, topography STM images can contain interference patterns which can make the identification of the zigzag direction more difficult.

It is theoretically expected that for a SWNT sample with randomly distributed chiralities, the total number of metallic nanotubes should be one third of the total number of tubes in the sample. This situation would only occur if there was no chiral selectivity at all in the production process and if the purification process did not preferentially alter the abundance of one or the other type of tubes. However, we found that this statistics was not completely correct for our raw material. Indeed, the number of metallic nanotubes in comparison with semiconducting ones has been found to be closer to a fourth of the total number of tubes. This observation of an apparent preferential growth of semiconducting SWNTs in our HiPco sample is sustained by other recent works [83] and references therein, where it is shown that a correlation exists between the diameters of SWNTs and the percentages of metallic and semiconducting tubes. Density functional theory calculations showed that semiconducting tubes are energetically more stable (higher cohesive energy per carbon atom) than metallic tubes, where the difference in cohesive energy scales with $\sim 1/d_t^2$ [83] and is therefore only significant for small diameter tubes with $d_t < 1.1$ nm. Referring to the diameter distribution displayed in Fig. 3.3 a), about 60% of individual tubes and small bundles (2-3 tubes) in our case have a diameter smaller than 1.1 nm and therefore an increased abundance of semiconducting tube can be expected. This unbalanced distribution of nanotube species increases further the difficulties towards a systematic investigation of phenomena specific to metallic nanotubes.

Chapter 4

Hydrogen plasma-induced defects

An in depth understanding of hydrogen interactions with sp^2-bonded carbon is of high importance for applications like hydrogen storage in carbon-based nanomaterials [84, 85], response of graphite tiles fusion reactor walls to hydrogen plasma [86] and more fundamental effects like proton-induced magnetism [87–89] or the formation of hydrogen molecules in interstellar dust clouds [90]. Considerable attention has been given recently to effects of hydrogenation on the electronic structure of nanocarbon [91–95]. Recently, the adsorption of atomic hydrogen onto graphite has been studied by means of ultraviolet photoelectron spectroscopy, high-resolution electron-energy loss spectroscopy and STM methods [96–100]. It has been demonstrated that chemisorbed H atoms are stable at room temperature and that interaction between H-adatoms lowers the adsorption energies, resulting in H-adatom clustering. This is supported by the observation of C-H bonds in hydrogenated SWNTs which can survive heating up to 400-600°C [85]. Theoretical works [91, 92] also predict chemisorption of atomic hydrogen onto nanotubes, with adsorption energies in the range of 1.0-2.5 eV per H atom.

A single hydrogen atom chemisorbed on the wall of a sp^2-hybridized carbon system can be regarded as a defect site, switching a single carbon atom from a sp^2- to a sp^3- bonding configuration and localizing the corresponding π-electron in a σ-bond. The importance of the H-C complex to control the electronic structure can be understood from organic chemistry, where the increasing degree of hydrogenation of a metallic sp^1 carbon chain changes its electronic nature to a semiconductor (polyacetylene) or even an insulator (polyethylene). A similar process was demonstrated in electrical transport measurement of strongly hydrogenated SWNTs [101].

However, the local atomic and electronic structure of adatoms clusters

have never been studied experimentally. Also most of the theoretical investigations focus on individual adatoms on sp^2-bonded surfaces or address the complete hydrogenation limit. In this work, by combining LT-STM/STS investigations with first-principle computer simulations, we studied the effects of individual low-energy and low dose ECR hydrogen plasma-induced defects on the electronic structure of SWNTs.

4.1 Generation of the defects

Typical treatments of the SWNTs with the 2.45 GHz ECR hydrogen plasma source have been performed in-situ with the sample kept at room temperature and hydrogen pressures of about $7 \cdot 10^{-2}$ mbar. Under these conditions, the hydrogen plasmas could easily be ignited with a short high power microwave pulse and then maintained with a constant power of 60 W. The same ECR plasma source has been characterized in an earlier work for hydrogen [98, 102]. The measurement of the H-ion kinetic energy distribution with an electrostatic analyzer showed that 85 % of the hydrogen ions have a kinetic energy below 2 eV, and the maximum detected energy was about 16 eV. A typical ion flux, with the probe sample positioned right under the antenna at a vertical distance of about 6 cm, was of the order of $2 \cdot 10^{13}$ s^{-1}· cm^{-2} [102]. The sample could be positioned laterally 0-7 cm off the center of the plasma glow zone, such that the ion flux on the sample surface could be modified by changing its horizontal position. We considered a mean defect separation of about 10 nm on the SWNTs as being well-adapted to study the long-range modifications of the local density of states induced by individual defects. The appropriate exposure parameters have been calibrated using an ex-situ cleaved HOPG sample where the defect density has been
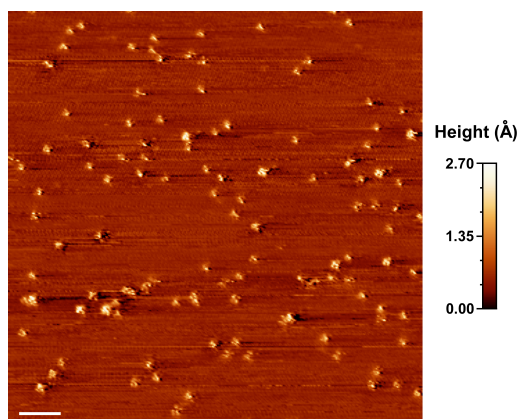

Figure 4.1: *Typical topography STM image of a HOPG surface subjected to a hydrogen ECR plasma at a pressure of $7 \cdot 10^{-2}$ mbar, microwave power of 60W. Exposition time 1 s at a lateral distance of about 3 cm far away from the glow zone. $V_s = -0.47$ V, $I_s = 0.77$ nA. Scale bar: 10 nm.*

evaluated by means of STM topography measurements. HOPG was chosen due to its structural equivalency to the SWNT and due to the simple and fast preparation of the surface, which allowed a rapid screening of different exposure parameters. Figure. 4.1 shows a typical image of a HOPG surface which has been subjected to a hydrogen plasma with the optimized exposure parameters. The tip has been generally primarily conditioned on a clean Au(111) surface, since the indentation method described in chapter 3.4.2 is not applicable on HOPG. A self-correlation analysis has been systematically performed on each image in order to check that the topography has not been recorded with a multiple tip.

It was shown in an earlier work using the same plasma source under similar conditions that only hydrogen ions give rise to local defects on a HOPG surface (as opposed to atomic hydrogen) [102]. However, one can expect that the curvature induced partial sp^3 character in small diameter SWNTs will lead to an increased affinity for H chemisorption of the tubes compared to the flat HOPG [102, 103]. In this context, we need to conclude that the defect density produced on the HOPG can not directly be related to the one on SWNTs for the same exposure parameters. Indeed, a higher defect density is expected for the SWNTs. We found that exposition parameters leading to a surface density of defects on HOPG of about 100 defects for a scanned surface of 100 nm × 100 nm were well-adapted to reach the desired defects separation of about 10 nm on SWNTs. In other words, this means that the number of defects generated on a SWNT sample is about ten times higher than on HOPG for the same exposition parameters, in accordance with the preceding discussion. With the sample positioned directly under the plasma glow zone, even for the shortest possible exposition times of about 1 s, the defect density exceeded considerably the value we were aiming for. This is why the sample has been laterally moved away from the glow zone to reduce the ion flux on it. At a distance of about 3 cm from the antenna axis, the desired defect density could be obtained for an exposure of the sample of 1s. In Fig. 4.1, one can count 107 defect sites on an area of

	d	p_{chamber}	T_{exp}	P_{MW}
Hydrogen	∼ 3 cm	$7 \cdot 10^{-2}$ mbar	1 s	60 W

Table 4.1: *Optimized exposition parameters of the ECR hydrogen plasma source to achieve a defect density of 0.1 nm^{-1} on SWNTs. The nomenclature is d: lateral distance of the sample with respect to the antenna axis , $p_{chamber}$: pressure in the plasma chamber, T_{exp}: exposition time, P_{MW}: microwave power. The plasma treatments have always been performed with the sample at room temperature.*

100 nm $\times$ 100 nm, which corresponds to the stochastic error to the target density of 100 defects per 1×10^4 nm^2. The different exposition parameters are summarized in table 4.1.

4.2 Defect types on HOPG: expectations for SWNTs

The interaction of hydrogen with sp^2-bonded carbon networks, and more specifically the local structural and electronic modification induced by point defects have been investigated earlier in our group using scanning probe and photoelectron spectroscopy investigations of a HOPG surface subjected to the same ECR plasma source, under similar exposition parameters as in the present work [97, 98, 102]. Due to its largely defect-free surface, HOPG represents an ideal system for the study of long-ranged electronic effects of point defects artificially introduced into the sp^2-bonded carbon network. Two types of defects could be distinguished with a combined detection mode of STM and AFM allowing a simultaneous imaging of the rearrangement of atom positions and of the affected LDOS: chemisorption of hydrogen on the basal plane of graphite and carbon vacancies. Whereas the signature in the current signal image of both chemisorption and vacancy defect types was a bright spot localized at the defect position, the topography image revealed local depressions for vacancies [97]. The formation of hydrogen chemisorption defects was observed with about four times higher frequency than that of atomic vacancies. One can expect even more chemisorption sites on SWNTs because of the curvature-induced lowering of the adsorption energy barrier mentioned above [102, 103], allowing also the adsorption of atomic hydrogen present in the plasma.

4.2.1 Vacancy formation mechanisms

The maximum kinetic energy of the hydrogen ions in the plasma chamber is not high enough to explain the formation of vacancies on HOPG by the ejection of a carbon atom. This can be shown by the empirical relation 4.1 which gives the sputtering threshold kinetic energy for low ion energies and target-to-projectile mass ratio $M_2/M_1 \leq 0.3$ [104]:

$$E_{\text{th}} = \frac{E_{\text{B}}}{\gamma(1-\gamma)} \tag{4.1}$$

E_{B} is the binding energy of surface atoms, which can be approximated by the heat of sublimation [104], and $\gamma = 4\frac{M_1 M_2}{(M_1+M_2)^2}$ is the energy transfer coefficient for a head-on binary elastic collision. With $E_{\text{B}} \simeq 7.4$ eV (heat of sublimation of graphite), an energy threshold of $E_{\text{th}} \simeq 36$ eV can be

found for the formation of vacancies by impact sputtering of hydrogen ions on HOPG.

For SWNTs, the minimum kinetic energy needed by a carbon atom to leave its position in the atomic network, called the displacement threshold energy T_d, has been shown to be chirality and diameter dependent [105] for diameters smaller than 1 nm. For the SWNT material we used, the minimal diameter has been estimated to be about 0.5 nm. For such a small diameter, T_d is found to be about 16 eV. If we compare this value with $T_d = 22$ eV for graphene, we can estimate a minimum E_{th} of about 26 eV. Therefore, the maximum kinetic energy of the hydrogen ions of 16 eV (with 85% of ions in the range 0 - 2 eV) is still well below the estimated energy threshold for vacancy formation by sputtering for HOPG as well as for SWNTs.

For sub-threshold energy hydrogen ions, the creation of vacancies in the sp^2 network can occur by surface etching. It has been theoretically shown that vacancies can be formed on graphene within a sequence of hydrogen adsorption processes leading to methane desorption [106]. This has been used experimentally to selectively etch SWNTs with an hydrogen plasma [94,107,108]. However, the formation of only one vacancy needs the adsorption of four hydrogen ions at the same location [106], and etching of SWNTs has been observed for exposition times of the order of several minutes with a one order of magnitude higher hydrogen pressure [108]. Thus, for the very low dose used in our experiments, the probability for vacancy formation from etching is very low.

A more probable explanation for the formation of vacancies by ions of low kinetic energy is the neutralization process of the ions, where the charge transfer from the surface to the approaching ion leads to a weakening of the sp^2 bonds and a finite destruction cross section [109]. The same mechanism is expected for SWNTs, where possibly more vacancy type defects should appear, because of the curvature induced lowering of the C-C bonding energy. As the curvature enhances the probability to form both atomic hydrogen chemisorptions and vacancies on the wall of SWNTs, further *ab initio* calculations are needed to estimate the H-adatom to vacancies ratio as a function of the tube diameter.

4.3   Topography of H-plasma treated SWNTs

4.3.1   Defect distribution

Typical STM topography and current error signal overview images of ECR H-plasma treated SWNTs are shown in Fig. 4.2 a) and b), respectively. In comparison with the SWNTs imaged just before the plasma treatment, one can observe the presence of additional hillock-like features on the nan-
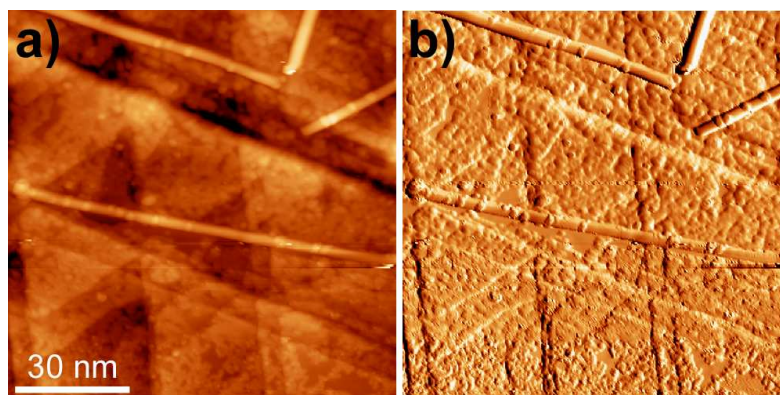
Figure 4.2: *a) Overview STM topographic image of SWNTs on Au(111) exposed to a low dose and low energy ECR hydrogen plasma. $\Delta z = 20$ Å, $V_s = 1$ V, $I_s = 0.1$ nA. b) STM current error image of the same region as in a), $\Delta I = 40$ pA.*

otubes. Note that since only the LDOS (and not the total charge density as for AFM) can be measured within STM, no direct distinction between H-adatoms and vacancies can be made. The average density of hillock-like defects along the SWNTs could be determined to be about one every 8 nanometers, which remains close enough to the desired value of one defect every 10 nanometers we are aiming for. The ratio between artificially created and native defects could be estimated to be larger than 20. These estimations have been made from topography measurements at several locations on different samples subjected to the same treatment.

4.3.2   Defect patterns

Figure 4.3 shows different STM topography images of typical defect features on two semiconducting tubes in a) and b), and an armchair metallic one in c). The tip-tube convolution effect has been taken into account and a corrected image is displayed under each original STM image. The corrected images are line by line flattened in order to increase the contrast and get a better definition of both the defect patterns and the atomic lattice. Height profiles along the black dashed lines parallel to the tube axis are displayed on the right-hand side of each STM image. Here, the apparent height of the defect features is ranging from 0.5 Å to 4 Å, with a lateral extension varying typically between 5 Å and 30 Å.

In order to identify experimentally imaged defects, theoretical constant current STM image predictions of point defects such as atomic mono- and

divacancies, adatoms or Stone-Wales (SW) defects on graphene and carbon nanotubes have been reported in the literature [34, 110, 111]. For example, Figure 4.4 shows a large scale density functional theory (DFT) simulated constant current STM image for an armchair (10,10) SWNT with a single SW defect, for negative and positive bias voltages. However, the determination of the nature of a given defect from a direct comparison of experimental and theoretical STM images is not straightforward since the experimental image is not a one-to-one picture of the charge density. STM images can be strongly affected by various effects due to the convolution of the tip with the sample [78]. This is illustrated for example in Fig. 4.3 a) where a typical tip-related distortion is shown. Here one can observe that four defects (positions indicated by black arrows in the line profiles) present the same pattern in the topography image. However, the spectroscopy analysis showed that all the six defect sites in this image have a different electronic
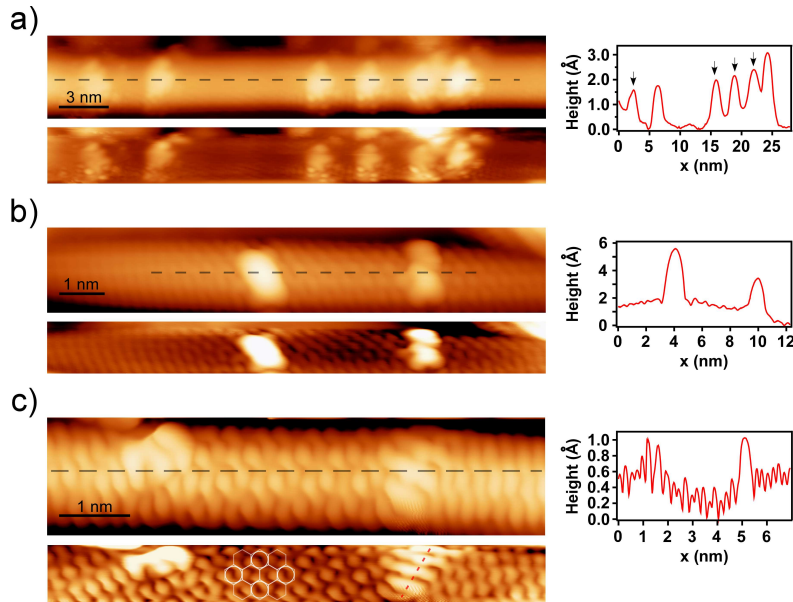

Figure 4.3: *Detailed STM topography image of SWNTs (semiconducting for a) and b), metallic armchair for c)) with typical defect patterns. Under each image in a), b) and c) a corrected and line by line flattened image version is shown. Apparent height profiles along the black dashed lines are displayed on the right-hand side of each STM image. Setpoint parameters: a) $V_s = 1$ V, $I_s = 0.1$ nA, $\Delta z = 10.8$ Å, b) $V_s = 1$ V, $I_s = 0.3$ nA, $\Delta z = 10.6$ Å, c) $V_s = 0.8$ V, $I_s = 0.1$ nA, $\Delta z = 4$ Å.*
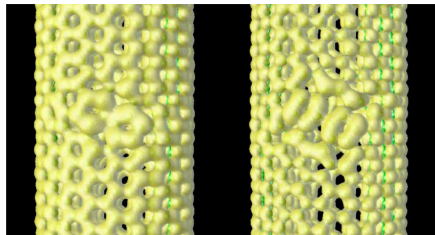
Figure 4.4: *Large scale DFT simulated constant current STM image for an armchair (10,10) SWNT with a single SW defect, for applied external tip-sample bias of -1.5 V (left) and +1.5 V (right), taken from Ref. [112].*

signature in the local density of states. The observed pattern are in fact an image of the tip apex due to the convolution of a relatively flat tip with a very sharp and localized protrusion at the defect position. It means in this case that the identification of the nature of the defects could only be done if one would know the exact tip apex structure and dispose of an extensive set of simulated STM images of different defect structures and combinations of them. As the second condition is today a quite routine task, the first one, on the other hand, is still inconceivable. In many cases, the defect sites show a uniform, structureless and intense hillock as for example in Fig. 4.3 b). The stripe structures and the relatively low apparent height of the defect site on the right of the armchair SWNT displayed in Fig. 4.3 c) show an evident similarity with the *ab initio* simulation for a $(10, 10)$ SWNT with a SW defect presented in Fig. 4.4. Indeed, one can observe that the orientation of the defect-induced stripes in the density of states for both experimentally observed and simulated tubes is the same (zigzag direction highlighted with a red dashed line in Fig. 4.3 c)), but for a clear and unambiguous identification of the nature of this defect, one will need more information on its electronic structure.

It is important to stress here that, similarly to hydrogen ECR plasma treated HOPG [97, 98], a long range redistribution of the electronic density with a period larger than but commensurate to the underlying atomic lattice has been observed near a great majority of defects, *e.g.* in Fig. 4.3 b) and c). The presence of these patterns known as $(\sqrt{3} \times \sqrt{3})R30°$ superstructures has already been observed experimentally on SWNTs [75, 113] and was found to be a signature for large momentum scattering of electronic states at defects, giving subsequent indications for a local modification of the electronic structure [79, 98, 114]. An important observation is that physisorbed adsorbates do not perturb the surrounding charge density (no reconstruction can be observed) [36]. A detailed discussion on the formation of these superstructures will be given in section 4.5.

At this point, we need to conclude that from a pure STM topography investigation, it is very challenging to clearly identify a specific defect configuration. Nevertheless we are able to make some general statements on

the type of defects we can possibly expect to result from the hydrogen ECR plasma interaction with the SWNTs. From the discussions above, it follows that the most probable defect types one would expect on SWNTs subjected to a low-energy and low dose hydrogen ECR plasma treatment are: (i) H-adatoms, (ii) vacancy-types and (iii) combinations of both including hydrogenation of single vacancies by partially or fully saturating the highly reactive dangling bonds (adsorption energy of 4.36 eV for a single vacancy in graphene [89]), and (iv) SW defects.

Thus, in order to get a deeper understanding on the nature of the observed defects, one needs to study the electronic structure of the H-plasma subjected SWNTs. This can be done by means of scanning tunneling spectroscopy (STS), which constitutes the topic of the following chapter.

4.4 Modifications of the local electronic structure of semiconducting SWNTs

The atomic and electronic structures of SWNTs with the most stable defect configurations discussed above were simulated by *ab initio* density functional theory (DFT) calculations and compared with STS measurements. All the DFT calculations presented in this work have been performed at the Helsinki University of Technology, Laboratory of physics (Dr. A. V. Krasheninnikov and Dr. A. S. Foster) and the University of Helsinki, Accelerator Laboratory (Dr. A. V. Krasheninnikov and A. Tolvanen), Finland. Technical details about these calculations are given in appendix A.

4.4.1 Single gap states

4.4.1.1 *Ab initio* calculations

The most probable defect structures discussed above have been calculated for semiconducting $(10,0)$, $(8,4)$ and $(8,0)$ nanotubes with up to 120 carbon atoms in the simulation cell. Most of the experimentally observed SWNTs could not be simulated due to their prohibitively large unit cells. However, the characteristic features of the theoretical simulations can be found in the experimental investigations. We therefore can generalize many of the electronic features observed in the simulations of the three tube species to the experimental results we obtained on tubes of different chiral vectors. Figure 4.5 a) shows different ball-and-stick models of relaxed defect configuration on a $(10,0)$ SWNT. The calculated defect structures are: one H-adatom (H-adatom), a naked single vacancy (S_Vac), a single vacancy with one (S_Vac H), two (S_Vac 2H) and three (S_Vac 3H) chemisorbed hydrogen atoms. The corresponding band structures for an energy range of 1.2 eV

centered on the mid-gap level are displayed in Fig. 4.5 b). In order to make a comparison with experimental spectra easier, the LDOS averaged on atoms within 2 Å from each defect structure presented in Fig. 4.5 are displayed in Fig. 4.6. Here the LDOS is reconstructed from the k-discretized band structure $E(k)$ in Fig. 4.5 b) by means of the "tetrahedron" method [115].

In agreement with previous simulations [91,92,96,116], it has been found that the energetically most favorable position for a H-adatom is on top of a carbon atom. For the studied SWNTs, the adsorption energy varies between 1.5 eV and 2 eV and the C-H bond length is 1.1 Å. The H adsorption energy is higher for nanotubes with small diameters compared to graphene (0.87 eV [89]) as curvature enhances the sp^3 character of the carbon atoms in SWNTs [102, 103]. For all theoretically studied semiconducting SWNTs ((8,0), (10,0) and (8,4)), the H adsorption results in the formation of a new quasi dispersionless state in the middle of the gap, as can be seen in Fig. 4.5 b) for a (10,0) SWNT. This H-adatom-induced flat band results in a very narrow and intense peak at the mid-gap level in the LDOS, which is truncated in Fig. 4.6 a), with a width of ~ 20 meV.

One can observe in Fig. 4.5 a) that a naked single vacancy reconstructs by saturating two dangling bonds and forming a pentagon. This is true for all types of nanotubes, independent of chirality [28,117]. The electronic signature of such a single vacancy in a (10,0) SWNT is a low dispersive state in the middle of the bandgap, with a width of the band of about 180 meV. A careful analysis of this new band reveals the presence of a rising inflection point resulting in a split peak in the LDOS (LDOS $\propto (dE/dk)^{-1}$) shown in Fig. 4.6 b). Simulations of single vacancies in graphene using a simple Hückel model have shown that vacancy-induced states near the Fermi level are spatially localized on the atoms surrounding the vacancies [118]. These localized states provoke an enhancement of the tunneling current at vacancy positions on SWNTs, giving rise to protrusions in TB based simulations of STM images [40,110]. This is supported by STM measurements on graphite and SWNTs [30, 97]. However, TB-based calculations do not show split structures for the vacancy-induced gap state, [110] and references therein. A possible explanation might be derived from previous *ab initio* calculations on the effect of structural defects on the conductance of SWNTs. Here two narrow dips were observed at the Fermi level in the conductance spectrum, originating from two π-like quasibound states originating from the three dangling bonds [41].

Ab initio calculations have also been performed for a naked vacancy on a (8,0) SWNT, where a similar low dispersive band with a rising inflection point is observed, but at a position close to the CBE. This can be seen in Fig. 4.9 d). The width of the split peak structure for the (8,0) is found to be about 110 meV. This observed change in the energy position of the
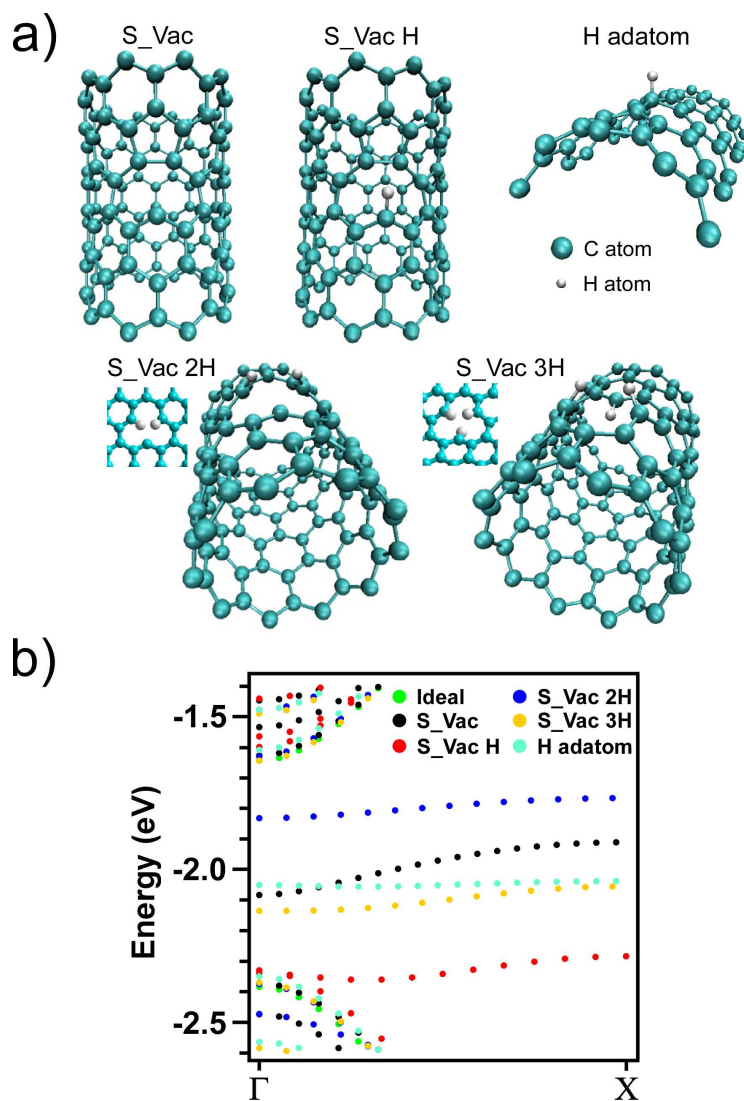
Figure 4.5: *a) Ball-and-stick models of different relaxed defect configurations for (10,0) SWNTs, which are: one H-adatom (H-adatom), a naked single vacancy (S_Vac), a single vacancy with one (S_Vac H), two (S_Vac 2H) and three (S_Vac 3H) hydrogen atom decorations. b) Calculated electronic structure for each defect configuration in a).*
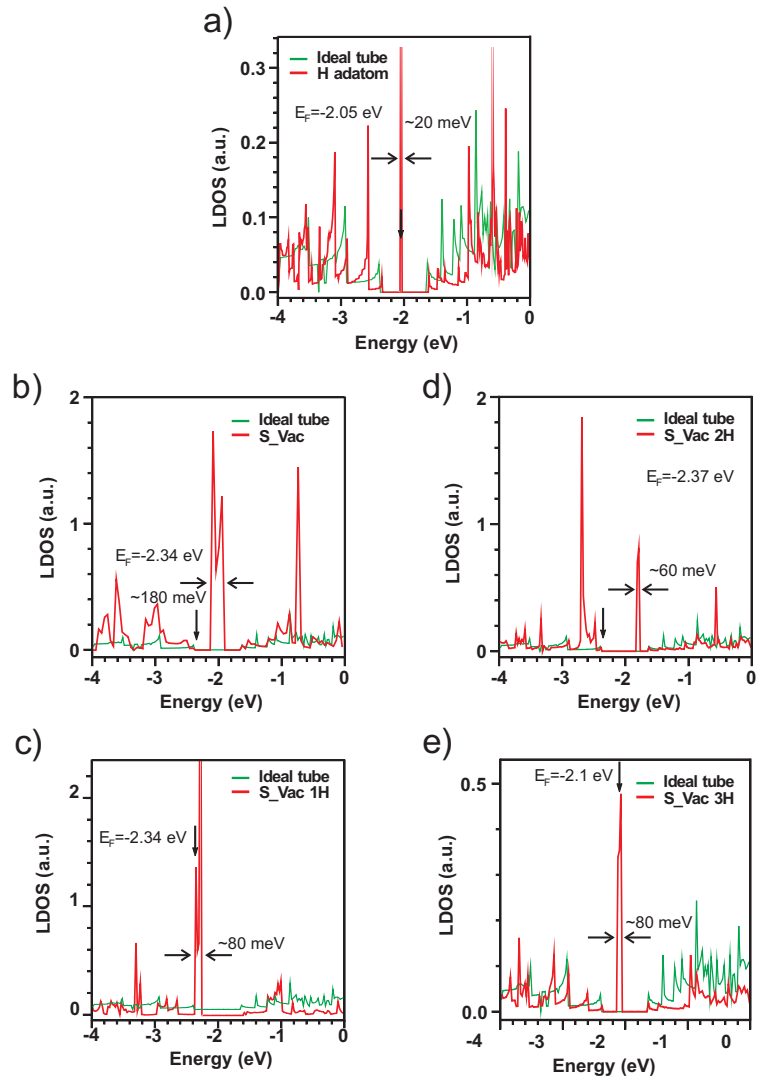
Figure 4.6: *Calculated LDOS averaged on atoms within 2 Å from the defect structures for a (10,0) SWNT: a) a H-adatom, b) naked single vacancy, c) single vacancy with one adsorbed H, d) single vacancy with two adsorbed H, e) single vacancy with three adsorbed H. The position of the Fermi energy and the approximated width of each gap peak are given.*

low dispersive bands for two different semiconducting SWNTs constitutes an important indication for a chirality dependence of the LDOS features for the same defect configuration.

Figures 4.5 b) and 4.6 show that low dispersive states with a rising inflection point are still observable for hydrogen-decorated single vacancies, but their position in the bandgap depends on the number of chemisorbed hydrogen atoms for the same SWNT.

A similar effect has been theoretically reported for vacancies in graphite, where the naked vacancies-induced peak in the total density of states (TDOS) is shifted above the Fermi level for a hydrogenation of the vacancies [118]. In our case, however, the observed dependence on the number of decorating hydrogen atoms on the gap state position is not yet understood and will need more theoretical investigations. For the $(10, 0)$ SWNT, the state associated with the single vacancy is located at the mid-gap level, whereas the one of the single decorated vacancy is at the VBE. The doubly decorated vacancy produces a state in the upper quarter of the band gap, whereas the fully decorated one is in the mid-gap region again, see Figs. 4.5 and 4.6. The same calculation has been performed for the single decorated vacancy on a $(8, 0)$ SWNT. Here the single vacancy related state is located close to the CBE, whereas the single decorated vacancy produces a state in the lower quarter of the bandgap (see Appendix B).

The widths of the different defect-induced gap peaks for a $(10, 0)$ are given in Fig. 4.6. One can observe that the calculated width of hydrogenated vacancy-induced peaks is reduced by more than a factor of two compared to the naked vacancy. The same observation can be made for a $(8, 0)$ SWNT, where the width of the single decorated vacancy induced state is found to be about 40 meV, in comparison with the 110 meV calculated for the naked single vacancy induced state. It is however important to note that in the supercell DFT calculations, the peak width may depend on the system size, details of integration procedure over the BZ and other simulation parameters.

Furthermore, it can be observed that the different defect structures do not only give rise to intense peaks in the bandgap or at the band edges, but also inside the conduction (S_Vac) or valence band (S_Vac 1H, S_Vac 2H), as can be seen in Fig. 4.6.

To summarize the results of the *ab initio* calculations, we point out the following important observations:

(i) The general behavior is that for the presented defect structures, the electronic signature is dominated by a single peak (with a split substructure), which can have a certain width due to the dispersion of the corresponding state.

(ii) The energy position of vacancy-related peak structures is in the bandgap region and is found to be chirality dependent.

(iii) A single adatom is found to produce a very narrow state in the mid-gap region.

4.4.1.2 Spectroscopy measurements

In the following paragraphs, we are going to discuss a first set of experimental results on the basis of the *ab initio* simulations presented above. In order to study the spatial evolution of the defect-induced modifications of the LDOS, consecutive STS measurements have been performed as a function of the tip position x along the tubes axis. Typical data sets consist of 100 or 150 dI/dV spectra recorded with the lock-in technique on one or more topography line scans of 300 pts along the tube axis. The spacing between two spectra is 1.5 Å or less, which yields typical line scans of 5-20 nm. Such $dI/dV(x,V)$ data sets are called dI/dV-scans in the following. The scan window for the spectroscopy is usually chosen in such a way that two or more defects can be measured in the same data set. Note that the spatial range of a dI/dV-scan acquired within about 30 min is always observed to be slightly larger (typically of the order of 5%) than the spatial range of the following (or preceding) topography lines acquired within about 0.5 s. This is due to a dependency of the piezoelectric voltage constant on the scan velocity. In all combined STM/STS images presented in this work, this effect has been systematically corrected by means of a compression of the x-scale of the dI/dV-scan in order to be able to compare the topography and the spatially resolved spectroscopy of the same nanotube.

In comparison with unperturbed regions in semiconducting SWNTs, single point spectroscopy measurements on defect sites revealed dramatic changes in the dI/dV spectra, which can be associated with changes in the LDOS [58]. A large number of defect sites has been investigated and for the great majority of the defects, dI/dV spectra revealed the appearance of new gap states present as single or double intense and very narrow peaks. A pair of peaks symmetrically positioned relative to the mid-gap level is the most commonly observed feature. Single peaks could be found at different positions in the bandgap, either in the mid-gap region or close to (or even at) the VBE or CBE.

Figure 4.7 shows a first example of a defect-induced single peak structure in the LDOS of a semiconducting SWNT. The dI/dV-scan recorded along the horizontal dashed line in the STM topography image in Fig. 4.7 a) is
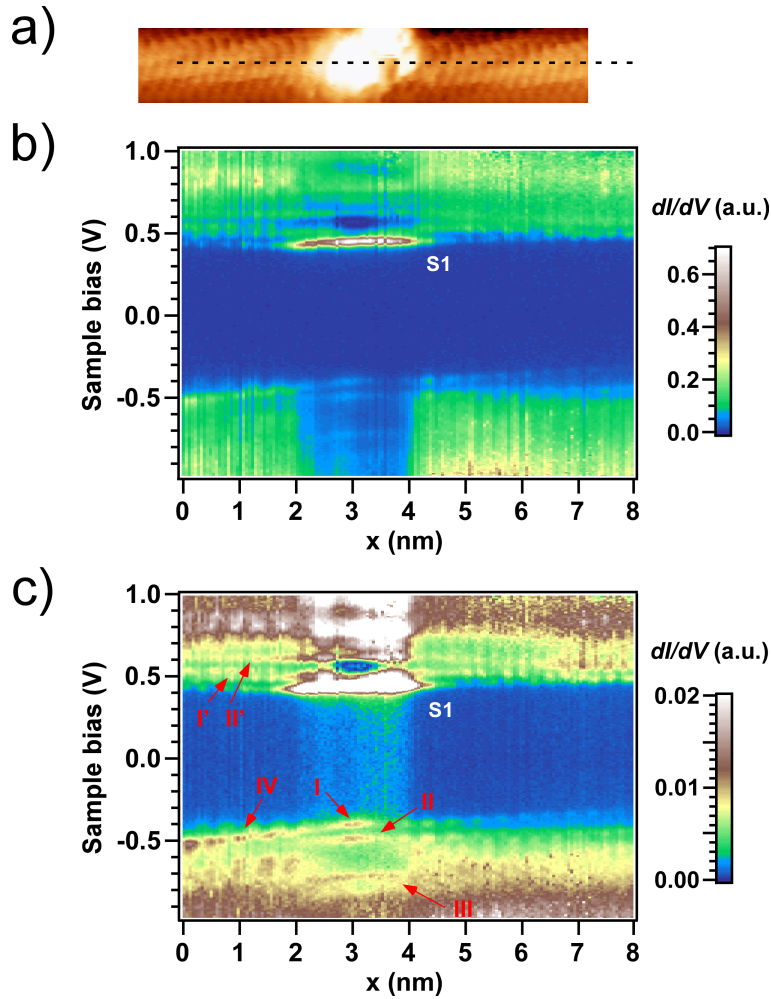
Figure 4.7: *a) STM topography original image of a portion of a semiconducting SWNT with a H-plasma-induced defect site. Possible chiral indices are: $(4,8)$, $(5,9)$ or $(6,10)$. b) Spatial variation of dI/dV as a function of the sample voltage recorded along the horizontal dashed line in panel a). The defect structure gives rise to an intense peak S1 at the CBE. c) Normalized map where each dI/dV spectrum curve in b) has been divided by the area computed between 0 V and -0.972 V. Measurement parameters are: $V_S = 1$ V, $I_S = 0.2$ nA, $T = 5.2$ K, $V_{mod} = 10$ mV, $x_{res} = 0.53$ Å.*

displayed in b). For this tube, no unambiguous assignment on the (n, m) indices could be performed and the three possible chiral indices are $(4, 8)$, $(5, 9)$ or $(6, 10)$. The dI/dV-scan clearly reveals the presence of a very intense and narrow peak positioned at the CBE, labeled S1. The FWHM of S1 is about 47 meV. We will consider peak shapes and widths in more details later in this section. The new defect-induced electronic state S1 is spatially extended on about 2 nm, which corresponds approximately to the lateral extension of the defect site imaged in a). Based on the *ab initio* calculations presented above, we can conclude on the formation of a vacancy-related (possibly with H atom adsorbates) defect structure induced by the interaction of a low energy hydrogen ion with the wall of a semiconducting SWNT, giving rise to a low dispersive state at the CBE.

A substantial drop in intensity of the differential conductance can be observed in the VB in the spatial range the defect-induced peak. This is a measurement artifact due to the choice of the setpoint voltage in the positive range above the energy position of the peak. One can understand this effect by considering the simple model shown in Fig. 4.8. Panel a) displays the real variation of the LDOS along the axis of an hypothetical semiconducting SWNT with four point defects producing different electronic states in the bandgap. Panel b) shows a simulation of the corresponding dI/dV scan with the setpoint voltage chosen at $+1.2$ V. Without altering the qualitative understanding of the effect, we consider the transmission coefficient T to be energy and bias voltage independent. We can then write the expression for
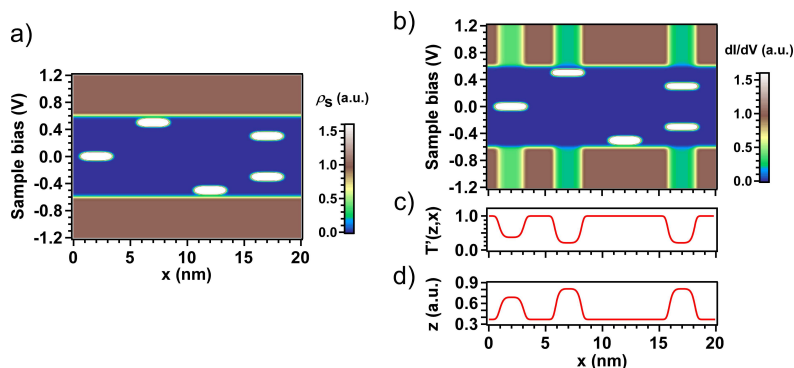

Figure 4.8: *a) Simulation of the real LDOS along the axis of an hypothetical semiconducting SWNT with 4 defects at positions $x = 2$ nm, 7 nm, 12 nm and 17 nm, giving rise to different electronic states in the bandgap. b) Simulation of the measured LDOS of the same SWNT as in a), with the setpoint voltage chosen at $+ 1.2$ V.*

the constant tunneling current as following:

$$I = I_\mathrm{s} = T(z,x) \cdot \int_{E_\mathrm{F}=0}^{eV_\mathrm{S}} \rho_\mathrm{s}(E,x)dE \qquad (4.2)$$

with $\rho_\mathrm{s}(E,x)$ being the LDOS at the position of the tip. It is obvious from Eq. 4.2 that for any increase of the integrated $\rho_\mathrm{s}(E,x,z)$ in the energy range running from 0 (E_F) to the setpoint bias voltage V_s, a corresponding decrease of $T(x,z)$ must occur to maintain the tunneling current I at the constant value I_s. The behavior of T as a function of the position x along the tube axis is plotted in Fig. 4.8 c). Now, from Eq. 4.2 and by considering the electron charge $e = 1$, the simulated dI/dV-scan can be formulated by the simple relation:

$$\frac{dI}{dV}(E,x) = T(z,x) \cdot \rho_\mathrm{S}(E,x) \qquad (4.3)$$

showing that the dI/dV-scan will show a drop in intensity on the whole bias range along the spatial location of new gap states positioned between 0 V (E_F) and V_s, as Fig. 4.8 b) shows. A local depression in $T(x,z)$ corresponds to an increase of the tip-tube distance z, since $T(z) \propto e^{-z}$. This makes sense since the LDOS at the position of the tip is decreasing as the tip-tube distance z increases. $z(x)$ is plotted in Fig. 4.8 assuming $T(z) \propto e^{-z}$. From the same argumentation above, it also follows that the corrugation induced variations of $z(x)$ recorded during the acquisition of a dI/dV-scan on a SWNT will result in the superposition of an additional topographic signal on the electronic structure information. This effect is responsible for the presence of a modulation in x-direction in the intensity of the VB and CB structures in the dI/dV-scans in Fig. 4.7.

The values of the voltage and current setpoints for the measurement presented in Fig. 4.7 have been set to $V_\mathrm{s} = +1$ V and $I_\mathrm{s} = 0.2$ nA, respectively. Based on the model presented above and under the condition that the signal to noise ratio is sufficiently high, it is generally possible to partially recover the strongly attenuated dI/dV features. This can be achieved by performing a normalization of the recorded spectra where each individual spectrum curve is normalized by the value of its area computed between 0 V and the final voltage value opposite to the setpoint voltage V_s. Figure 4.7 c) shows a normalized dI/dV-scan where each dI/dV spectrum curve in b) has been normalized by the integral between 0 V and -0.972 V. This constitutes an approximation of the experimental dI/dV-scan one would obtain with the setpoint voltage V_s set to -0.972 V. Note that the non-zero differential conductance observed below S1 in the bandgap is due to the amplification of the residual offset mentioned in section 2.2.

To enhance the details of the low lying dI/dV structures in the normalized dI/dV -scan, the full color scale has been limited to the maximum recorded intensity in the VB. It results that besides the intense peak at the CBE discussed above, one can clearly distinguish line structures in the VB, labeled I-IV. Similar structures labeled I' and II' in c) could already be distinguished in the CB on both sides of S1 in Fig. 4.7 b) before the normalization. In the following paragraphs, we are going to describe the behavior of the VB structures I-IV. The same analysis can be carried out for the CB structures I' and II'.

The single line structure IV in Fig. 4.7 c) is seen to split into two further line structures I and II clearly distinguishable in the spatial range of the peak S1. The energy splitting is found to be about 90 meV. One can observe that for $x > 4$ nm, I and II do not merge together as it is the case in $x < 2$ nm, but seem to remain separated on the visible x-range with approximatively the same splitting energy. The line structure III is clearly distinguishable in the spatial range of S1 and is located about 0.24 eV lower in energy than structure II.

In order to understand the origin of the observed line structures, one needs to analyze the modifications induced by specific defect configurations on the band structure of SWNTs in the VB and CB. Until here, we have studied the defect-induced changes in the bandgap region with emphasis on new low dispersive electronic gap states. Figure 4.9 shows calculated $E(k)$ band structures for different defect configurations on a large energy scale of 4 eV. For each defect configuration (also for other single adatom- and single vacancy-related structures not shown in this figure), the twofold degeneracy of the bands plotted in green in panels a) - d) of both highly symmetric zigzag $(8,0)$ and $(10,0)$ SWNTs is lifted. The energy splitting varies up to about 0.4 eV for the different calculated structures.

To study the degeneracy of the electronic structure of the SWNT shown in Fig. 4.7 a), we computed the band structures $E(k)$ for the possible corresponding SWNTs, *i.e.* $(4,8)$, $(5,9)$ and $(6,10)$ within a TB zone folding scheme. The results for $(4,8)$ and $(6,10)$ nanotubes are shown in Fig. 4.9 e) and f). Remarkably, the plotted bands in the VB and CB are twofold degenerated at the Γ-point. This is also the case for the $(5,9)$ nanotube (not shown). On this basis, we can identify the line structures I an II in Fig. 4.7 c) as two single bands resulting from the splitting of an initial twofold degenerated band (IV), induced by a local symmetry breaking related to the presence of the structural defect in the initial perfect periodic lattice of the SWNT in Fig. 4.7 a).

Two other examples of defect-induced single peak structures in the LDOS of a semiconducting SWNT are shown in Fig. 4.10. Panel a) shows the topography image of a semiconducting $(5,6)$ or $(6,7)$ SWNT with two
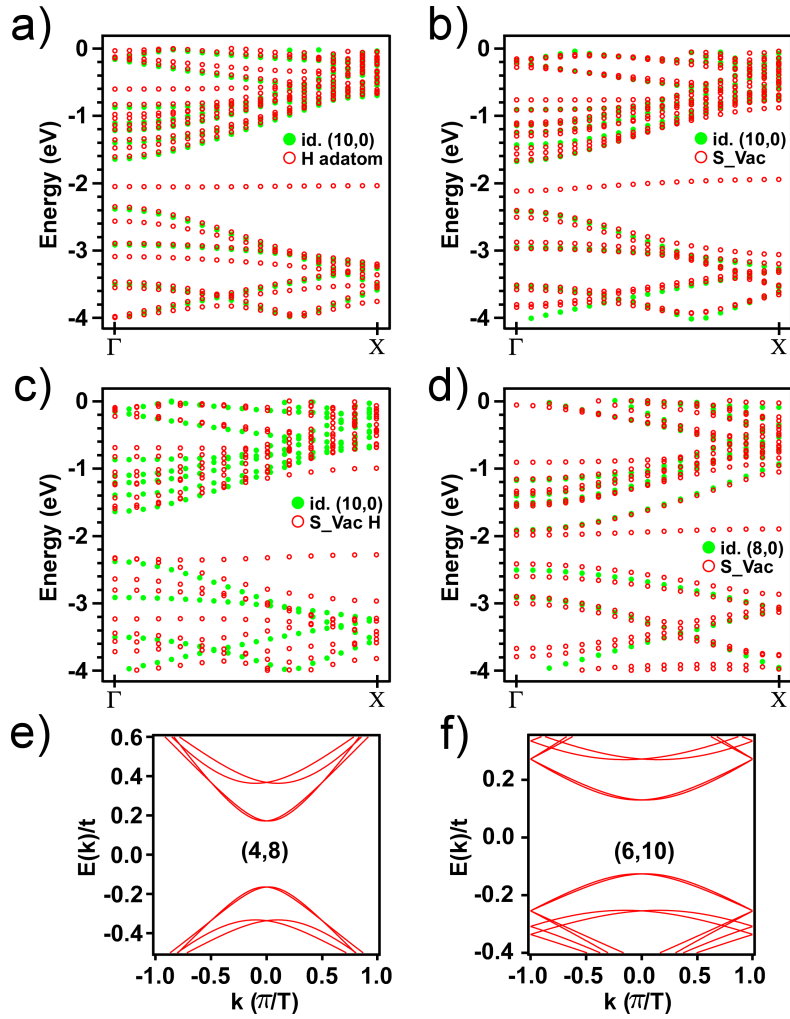
Figure 4.9: Ab initio *calculations of the electronic structure for different defect configurations and SWNTs. a) (10, 0) nanotube with one H-adatom, b) (10, 0) nanotube with a single naked vacancy, c) (10, 0) nanottube with a single vacancy decorated with one hydrogen adsorbate, d) (8, 0) nanotube with a single naked vacancy. For the (10, 0) nanotube, defect atomic structures are shown in Fig. 4.5 a). e), f) Electronic structure of pristine (4, 8) and (6, 10) nanotubes, derived from a simple zone folding scheme with overlap integral s = 0.13 and hopping integral t = 2.9 eV.*
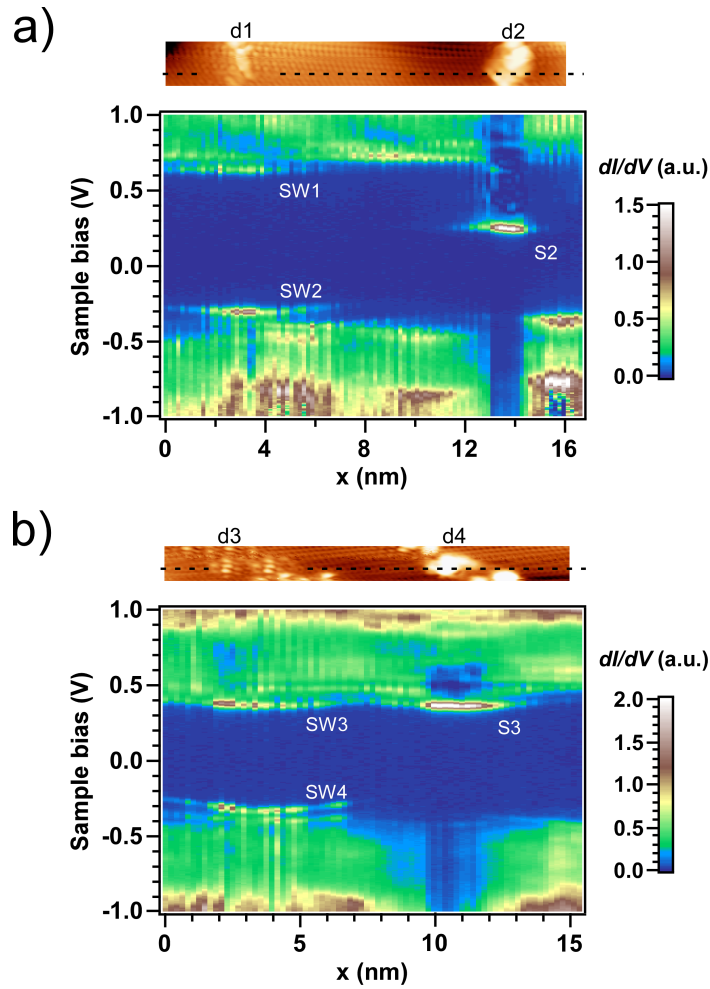
Figure 4.10: *STM topography images of SWNTs treated with low-energy hydrogen plasma and corresponding dI/dV-scans (lower panels) recorded along the horizontal black dashed lines for two nanotubes. a) Semiconducting SWNT ((6,5) or (7,6)) with two defect sites d1 and d2 giving rise to structures SW1-SW2 and S2, respectively. b) Semiconducting SWNT ((7,5) or (8,6))with two defect sites d3 and d4 giving rise to the dI/dV structure SW3-SW4 and S4, respectively. Measurement parameters in a) are $V_s = 1$ V, $I_s = 0.3$ nA, $T = 5.3$ K, $V_{mod} = 15$ mV, $x_{res} = 0.16$ nm, b) $V_s = 1$ V, $I_s = 0.3$ nA, $T = 5.8$ K, $V_{mod} = 15$ mV, $x_{res} = 0.2$ nm.*

defect sites labeled d1 and d2, separated by about 11 nm. The dI/dV-scan displayed in the lower panel has been recorded along the horizontal black dashed line running through the defect sites. The defect pattern d2 has a spatial extent of about 2.5 nm and gives rise to a sharp peak labeled S2 in the mid-gap region, with a FWHM of about 45 meV. The above discussed normalization process (see Fig. 4.7 c)) has been performed on the dI/dV spectra but no significant additional information resulted. We would like to stress here that the structures in the differential conductance visible in the energy range above S2, *i.e.* for energies larger than 0.26 eV are to a considerable degree due to a measurement artifact resulting from a voltage dependent tunneling barrier height inducing a negative differential resistance (NDR) behavior in the recorded *I-V* curve. The origin of the NDR related to sharp unoccupied states will be discussed in details in chapter 7. We found a FWHM of about 44 meV for S2. From *ab initio* calculations for $(8,0)$ and $(10,0)$ nanotubes, we know that several defect structure show the appearance of a sharp peak in the mid-gap region, as for example hydrogen chemisorption or the formation of a single vacancy decorated with three hydrogen adsorbates shown in Fig. 4.6 a) and e). Because of the chiral dependence of the position of vacancy-related electronic states, it is however not possible to determine if the peak S2 is a consequence of chemisorption of an H-adatom or a vacancy-related defect. A one-to-one comparison between experiments and simulations could be done on the basis of *ab initio* DFT calculations for the experimentally investigated SWNTs, *i.e.* $(6,5)$ and $(7,6)$ in this example. As mentioned earlier, the large number of atoms in the unit cells of these nanotubes (364 and 508 for $(6,5)$ and $(7,6)$, respectively) is however not adapted for a standard DFT calculation.

Figure 4.10 b) shows another semiconducting SWNT ($(7,5)$ or $(8,6)$) with two defect sites d3 and d4 separated by about 8 nm. Like in panel a), the original image has been corrected to compensate the tip-tube convolution effect. Although the topography image in the upper panel clearly reveals a multiple tip artifact, consistent spectroscopy analysis could be carried out. Similarly to the vacancy-related defect site in Fig. 4.7, the defect structure d4 gives rise to a sharp state at the CBE with a FWHM of about 48 meV, labeled S3. The normalization process revealed degeneracy breaking effects at the VBE, similarly as in Fig. 4.7.

4.4.2 Stone-Wales type defects

Peak structures S1, S2 and S3 in Figs. 4.7 and 4.10 have a spatial extent which matches approximatively the lateral extent of the corresponding defect structures observed in the topography images. However, the defect structures labeled d1 and d3 in Fig. 4.10 a) and b), respectively, show a

different behavior. Topography images of the defect structures d1 and d3 both reveal a pattern which is spatially localized along the main axis of the nanotube and extended along its circumference. The apparent height of these structures has a maximum value of about 0.8 Å for d1 and 0.5 Å for d3, and the lateral extent is about 0.5 nm for both patterns. By way of comparison, the maximum apparent heights of defect patterns d2 and d4 recorded with the same setpoint parameters are 2.5 Å and 1.2 Å, respectively. As can be seen in the dI/dV-scan of Fig. 4.10 a), the defect-induced pattern d1 clearly shows extended electronic states at the VBE and CBE regions. The peak structures labeled SW1 and SW2 have a spatial extent of about 7 nm. While SW1 has a quite constant energy of 0.64 eV, SW2 shows a parabolic-like shape around -0.27 eV. A similar behavior can be seen with the electronic states SW3 and SW4 induced by the defect site d3 in Fig. 4.10 b). Although one has to consider the lateral extent of SW3 and SW4 by taking into account the multiple tip effect visible in the topography image, the dI/dV spectra clearly show two parabolic-like structures for SW4, split by about 85 meV along the full spatial extent.

A detailed analysis of the structures SW1-SW4 is carried out in Fig. 4.11. Upper panels in a) and b) show detailed topography images of d2 and d4 which have been line by line flattened to get a better contrast of the defect patterns. The honeycomb lattice is indicated in white on both topography images. dI/dV-scans recorded along the horizontal dashed lines drawn in the upper panels of a) and b) are shown in the corresponding lower panels. To get a better insight into the behavior of the peak structures SW1-SW4, we plotted individual dI/dV spectra recorded along the vertical white dashed lines labeled with roman numerals on the right hand sides of panels a) and b). These spectra show clearly double peak structures labeled 1-4 and 1'-4' for SW1 - SW4. For the parabolic-like structures SW2 and SW4 the average energetic positions are indicated as 3-4 and 3'-4'. The energy splitting of the double peaks are 98 meV for 1-2, 86 meV for 3-4, 120 meV for 1'-2' and finally 58 meV for 3'-4'.

These splittings at the CBE and VBE are very similar to what we have discussed before as a result of the lifting of the degeneracy due to the presence of a defect. However, here we do not observe any strong single peak in dI/dV which can be associated to a new low dispersive state, and also the apparent height of the defects is below 1 Å. This is in contrast to what we would expect from a vacancy, H-chemisorption or H-decorated vacancy type defect. Therefore we might have a purely structural defect keeping the threefold coordination of the C atoms of the tube, *e.g.* a SW defect.

To compare our observations, we calculated the electronic structure of a SW defect in a $(10, 0)$ SWNT. Ball-and-stick models of both ideal $(10, 0)$ SWNT (green) and the same nanotube with a SW defect (red) are presented
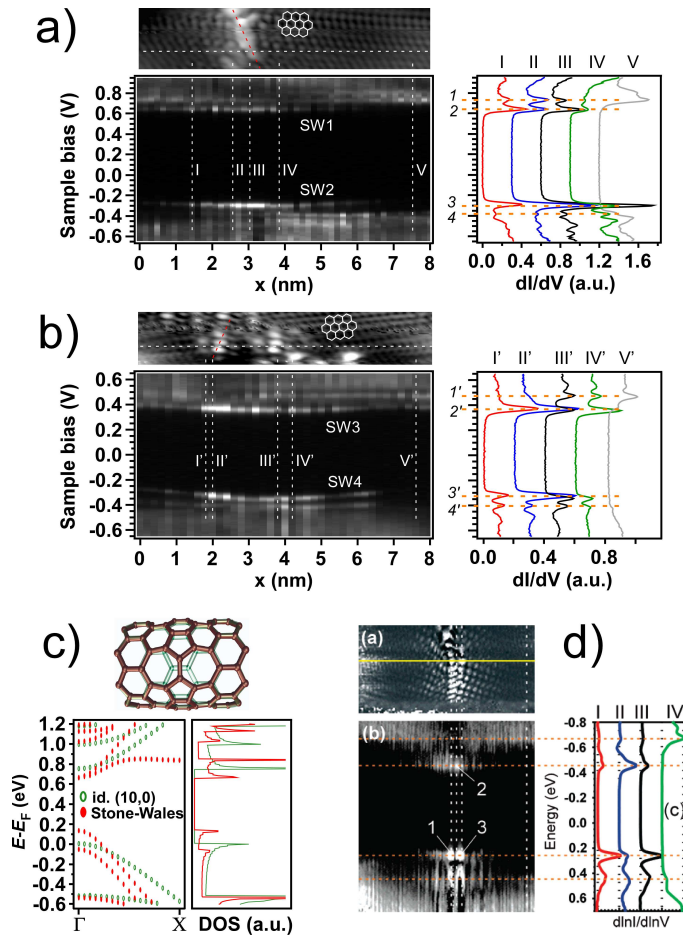
Figure 4.11: *a) and b) Upper panel: detailed flattened and topography image of defect site d2 (d3) from Fig. 4.10 a)(b)) with superimposed honeycomb lattice. Lower panel: spatial evolution of the differential conductance recorded along the horizontal dashed line drawn in the upper panel. Right hand side: dI/dV spectra recorded along the vertical white dashed lines labeled I(I') to V(V'). c) Topography dI/dV image and spatial evolution of dI/dV of a (9,5) SWNT with suggested SW defect, taken from [36]. d) Upper panel: ball-and-stick models of an ideal (10,0) SWNT (green) and with a SW defect (red). Lower panel left:* ab initio *calculation of the electronic structure of the ideal (10,0) SWNT (green) and the SW defect (red), right: corresponding TDOS.*

in the upper panel of Fig. 4.11 c). The corresponding electronic structure displayed in the lower panel clearly shows a splitting of the twofold degenerated bands corresponding to the first VHS of the non-perturbed nanotube, giving rise to double peak structures at the CBE and VBE, with energy separations of 180 meV and 210 meV, respectively.

Our results are further supported by the recently reported observation of shallow levels in dI/dV-scans for suggested SW defects created by the application of a voltage ramp at constant tunneling current between a STM tip and semiconducting nanotubes [36]. For comparison, the cited results are displayed in Fig. 4.11 d). The reported defect pattern shown in a dI/dV map acquired at $V_s = 0.4$ V in the upper panel of Fig. 4.11 c) present a strikingly similar shape with the observed patterns for d2 and d4.

Although we cannot rule out that the observed defects d2 and d4 may have been produced during the growth process of the nanotubes, it is fully plausible that the interaction of low energy hydrogen ions with the wall of a SWNT may result in the rotation of a C-C bond within the neutralization process of the ions discussed in section 4.2.1.

4.4.3   Symmetric paired gap states

In the following paragraph, we are going to describe the most commonly observed feature for H-plasma-induced defects, *i.e.* the appearance of paired gap states positioned symmetrically with respect to the mid-gap level. Then the nature of these paired states will be studied on the base of *ab initio* calculations.

4.4.3.1   Spectroscopy measurements

Figures 4.12 a) and b) show dI/dV-scans for two semiconducting SWNTs with a series of defect sites, recorded along the horizontal dashed lines. The topography image in panel b) has been corrected to compensate the tip-tube convolution effect. The assignment procedure has given three possible sets of chiral indices (8,1), (9,1) or (11,1) for a) and (6,2) for b). Note that the original topography image in the upper panel of Fig. 4.12 shows a double tip artifact. Here the same nanotube is imaged twice as we can judge from the atomic resolution where both nanotube images show the same chirality, and also from the fact that the relative position of the two defects remains the same. We have recorded several dI/dV-scans along different horizontal lines and on both nanotube images the spectroscopy shows identical features. Since we have actually imaged the same nanotube with two different protrusions of the tip, the spectroscopic features are indeed intrinsic to the nanotube itself and not to the tip.
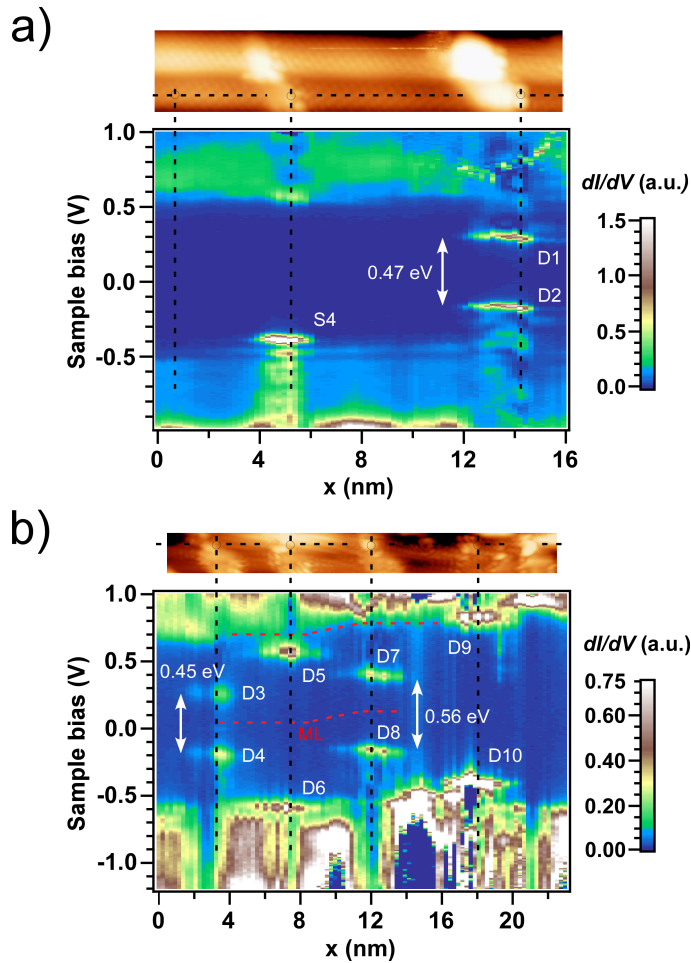
Figure 4.12: *STM topography images of semiconducting SWNTs treated with low-energy hydrogen plasma and corresponding dI/dV-scans (lower panels) recorded along the horizontal black dashed lines for two nanotubes. Possible chiral indices for the SWNT in a) are (8,1), (9,1) or (11,1), and (6,2) for b). A sharp single peak (S4) at the VBE and a pair of peaks (D1-D2) positioned symmetrically relative to the bandgap edges are visible in a). b) shows four defect-induced symmetric double peak structures with different energy separations (D3-D4, D5-D6, D7-D8 and D9-D10). Measurement parameters in a): $V_s = 1$ V, $I_s = 0.6$ nA, $T = 5.56$ K, $V_{mod} = 6$ mV, $x_{res} = 0.21$ nm, b): $V_s = 1$ V, $I_s = 0.3$ nA, $T = 5.36$ K, $V_{mod} = 10$ mV, $x_{res} = 0.22$ nm.*

A further example of a defect-induced single peak structure labeled S4 lying now slightly above the VBE can be seen in Fig. 4.12. A comparison with *ab initio* simulations suggests that the defect structure giving rise to the peak S4 is a single vacancy-related configuration (possibly with hydrogen atom adsorbates). On this basis, we attribute the oscillations in dI/dV below the peak S4 along the vertical dashed line to a local band splitting due to a defect-induced symmetry breaking. These oscillations are better evidenced in Fig. 4.13 a) where the dI/dV single spectrum recorded along the vertical black dashed line running through S4 is plotted.

On the right hand side of Fig. 4.12 a), one can observe a double peak structure labeled D1-D2, with an energy separation of 0.47 eV. Such pair of peaks symmetrically positioned relative to the mid-gap level with an energy separation of about half an electronvolt is the most commonly observed feature for low energy hydrogen ions-induced defects, as can be observed from analogous features as D3-D4 and D7-D8 in Fig. 4.12 b). However, larger energy separations can also occur, as D5-D6 and D9-D10 in Fig. 4.12 b) shows, where we measure an energy difference of 1.15 eV and 1.2 eV, respectively. The same differential conductance map of Fig. 4.12 b) shows a rigid shift of the band edges towards higher energy. This band shift is highlighted by the dashed red lines denoting the CBE and the midgap level, respectively. As can be clearly seen, the energetic positions of the two double peak structures D3-D4 and D7-D8 are symmetric with respect to the SWNT midgap level and not to the Fermi energy from which we can deduce that they are intrinsic to the electronic structure of the modified nanotube and do not result from interaction with the substrate.

A height profile of the Au(111) substrate recorded along a line parallel to the tube axis (not shown) indicates that the $(6, 2)$ SWNT is suspended between a terrace edge at the position $x \approx 9$ nm and another SWNT crossing at the position $x \approx 19$ nm. This induces an inhomogeneous charge transfer between the SWNT and the substrate, which explains the band shift. A similar behavior has already been observed for crossed SWNTs on gold and has been attributed to an effective hole doping in the suspended region, resulting from a reduced screening of the charge accumulation layer by the gold substrate [119, 120].

As already observed above for the single peak structures S1, S2 and S3 in Figs. 4.7 and 4.12, the spatial extent of the measured structures S4 and D1-D2 to D9-D10 in Fig. 4.12 matches approximatively the lateral extent of the defect patterns observed in the topography images and is generally of the order of 1-3 nm. This small spatial extent of the new electronic states indicates the effectiveness of our method to produce very localized and intense modifications of the electronic structure of SWNTs, yet without excessively damaging their structure. Both features, the strong modification
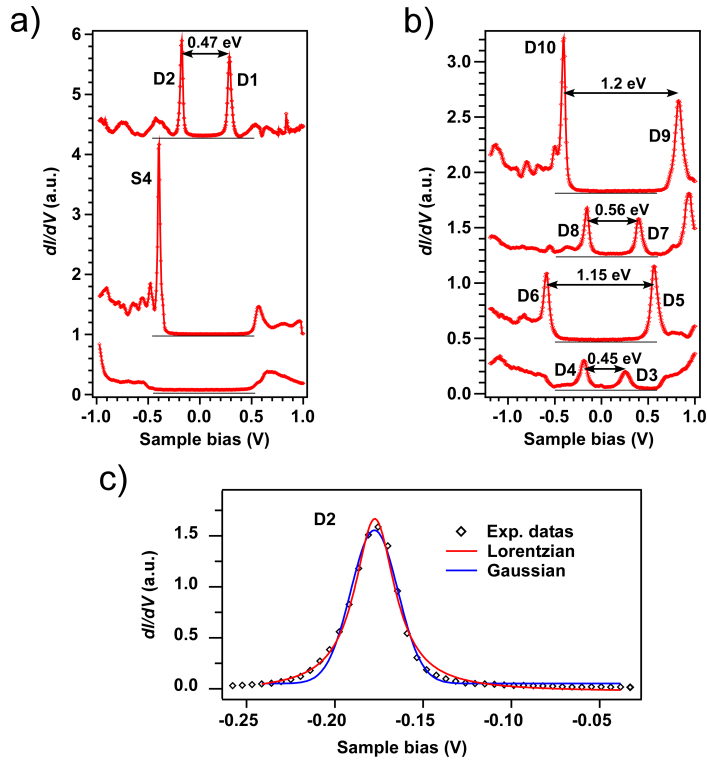
Figure 4.13: *Comparison of spectroscopic signatures of individual point defects. dI/dV plots in panels a) and b) correspond to the positions indicated by small circles for the SWNTs shown in Figs. 4.12 a) and b), respectively. c) Detail of the peaks D2 with Lorentzian and Gaussian fits.*

of the electronic structure and the relatively low structural damage, are prerequisites from the perspective of using this method to specifically alter the transport properties of SWNT-based devices.

Before going more into details on the origin of the frequently observed double peak structures, we will consider more precisely the shape and widths of the typically encountered defect-induced peak structures.

Figures 4.13 a) and b) show dI/dV plots versus bias voltage recorded at the positions corresponding to the intersection of the vertical and horizontal dashed lines shown in Figs. 4.12 a) and b), respectively. We would like to stress here that due to the voltage dependent tunneling barrier height we briefly mentioned in section 4.4.1.2, the intensity of peaks positioned below the Fermi level is systematically underestimated with respect to peaks lying

above the Fermi level. Thus, if the real intensity of a double peak structure is the same for each individual peak, the measured dI/dV signal will always give a smaller intensity for the peak lying below the Fermi level. More details on the voltage dependent tunneling barrier height will be given in chapter 7, where the NDR is discussed. The energy resolution of our STS measurements can be estimated with the following relation [121]:

$$\delta E = \sqrt{(3.3 \cdot k_B T)^2 + (2.5 \cdot V_{\mathrm{mod}})^2} \qquad (4.4)$$

where k_{B} is the Boltzmann constant and V_{mod} is the RMS value of the lock-in ac voltage component. For the STS parameters used to record the data presented in Fig. 4.12 a): $T = 5.56$ K, $V_{mod} = 6$ mV, and b): $T = 5.36$ K, $V_{mod} = 10$ mV , we find energy resolutions of $\delta E \approx 15$ meV and $\delta E \approx 25$ meV for a) and b), respectively. The narrowest measured FWHM in Fig. 4.12 a) and b) are found for D2 with 26 meV and D8 with 67 meV. The measurement energy resolutions are then found to be about two times smaller than the narrowest measured peaks for Fig. 4.12 a) and this ratio is found to be about 2.7 for Fig. 4.12 b). We have characterized a large number of peak structures and found FWHMs generally situated between 25 meV and 90 meV. A maximum value of 125 meV was measured for D3 in Fig. 4.12. In most of the cases, the measured peak shapes could be well fitted with a Lorentzian function. However, the best fits have always been obtained with Voigt functions, which are obtained by the convolution of a Lorentzian and a Gaussian function. For example, both Gaussian and Lorentzian fits of the the peak structure D8 give the same chi-square value of 0.0075. Figure 4.13 c) shows a detail of the peak D2 fitted with both Lorentzian and Gaussian functions. The chi-square values are 0.066 and 0.074 for the Lorentzian and Gaussian fit, respectively.

From a general point of view, the main observation is that the relatively small measured values of the FWHM indicate that the hydrogen plasma-induced new electronic states are characterized by a very low dispersion. From the discussions on the energy resolution above, we estimate the real FWHM to be about 10-15 meV for the smallest measured features.

4.4.3.2   *Ab initio* calculations: adatom-adatom interaction

As discussed above, we attributed the origin of single gap peaks as S1, S3 and S4 to vacancy-H complexes. The single peaks observed in the middle of the gap, as S2, could be related to the chemisorption of a single adatom or to a vacancy-H defect configuration. None of the simulated single vacancy- or single adatom-related defects gave rise to paired peaks positioned symmetrically with respect to the mid-gap level. From the discussions in subsec. 4.2.1, we think that the probability for vacancy-type defects to appear
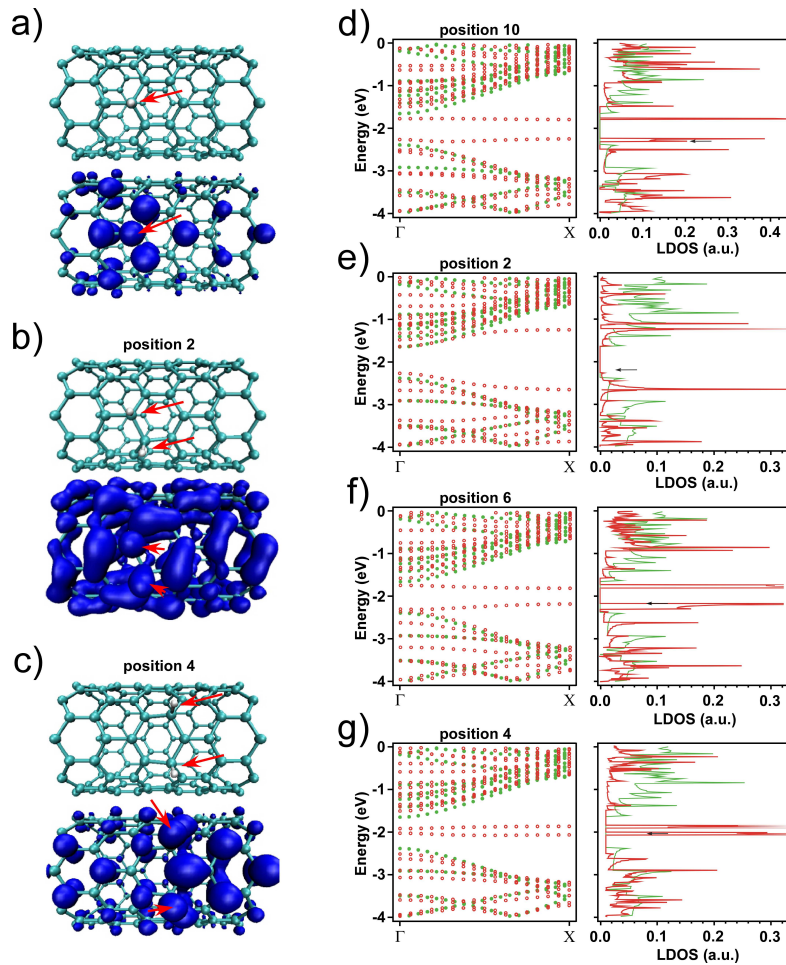
Figure 4.14: *Electron densities and band structures for a $(10,0)$ nanotube with one and two H-adatoms. a) Atomic structure with a single H-adatom, top view with electron density near the Fermi level (density $= 0.02$ $e/Å^3$ for energy interval -2 eV to -2.7 eV) for the same tube (lower panel). The position of the H-adatom is highlighted by a red arrow. b) and c) Atomic structures with two nearby adatoms for positions 2 and 4 (top view), respectively. Corresponding electron density near the Fermi level (energy interval -2 eV to -2.7 eV with densities 0.005 and 0.1, respectively). The positions of the H-adatoms are highlighted by red arrows. d)-g) Band structures and LDOS of a $(10,0)$ SWNT with two adatoms in positions (see Fig. 4.15 a)) 10, 2, 6 and 4, respectively.*
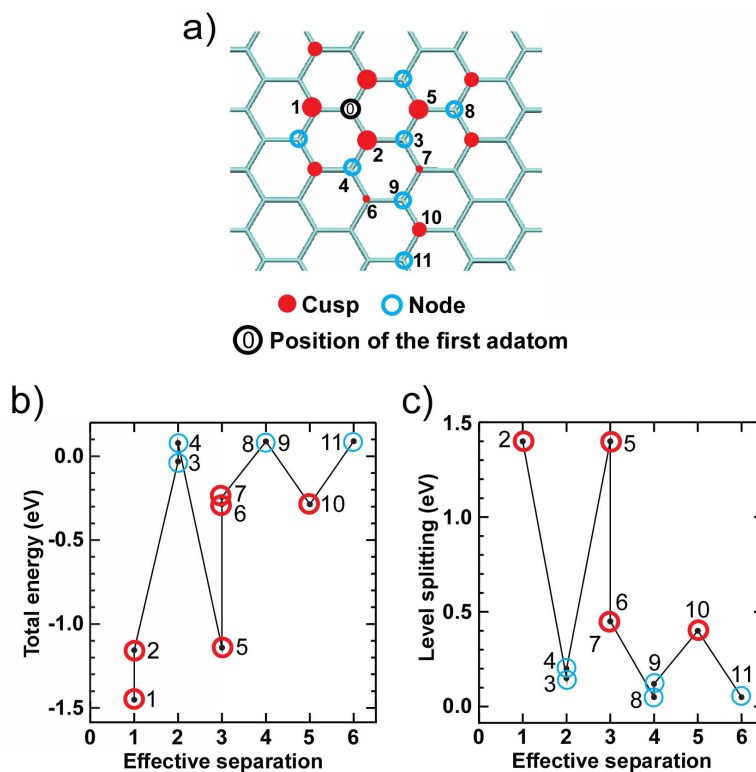
Figure 4.15: *First-principles simulations for a* $(10, 0)$ *SWNT with H-adatoms. a) The adsorption sites of H-adatoms. All positions are metastable (separated by energy barriers from each other) so that all of them can exist at low experimental temperatures. The red and blue circles reflect the nodal structure of electron density oscillation near the Fermi energy when there is a single adatom on site labelled "0". b) Total energy of the system for different positions of the second adatom. The separation between H-adatoms is defined as the number of bonds in graphene lattice on the migration path of the second adatom to arrive at site "0". c) Splitting of the H-induced levels in the gap due to adatom-adatom interaction.*

is smaller than for adatoms. Thus, we calculated the total energy and the electronic structure of SWNTs with configurations of two adatoms, as shown for example in Figs. 4.14 b) and c). Figure 4.14 a) displays an iso-charge density plot of the $(10, 0)$ SWNT with a single H-adatom near the Fermi level (energy range from -2.7 eV to -2 eV, density = 0.020 $e/\text{Å}^3$). Interestingly, one can observe that the electron density of the perturbed lattice

presents a nodal structure with a minimal density on the carbon atoms of the sublattice on which the H-adatom lies (nodes) and a maximal density on the atoms of the complementary sublattice (cusps). As we will show in the following, this sublattice dependent charge distribution is also reflected in the adsorption energy of a second H atom as a function of its adsorption site.

The different positions for two adatoms are schematically shown in Fig. 4.15 a). The first H-adatom is fixed on the position labeled "0" while the second is positioned above nearby atoms as shown in Fig. 4.15 a). The total energy of the system as a function of separation between the adatoms is presented in Fig. 4.15 b). Zero energy corresponds to infinite separation of adatoms. The lowest energy configuration has been found to be two adatoms on the adjacent sites.

It is evident from Figs. 4.15 a) and b) that the energy depends non-monotonously on the adatom separation, with the minima at the sites corresponding to the cusps in the electron density near single adatom, as shown in

Pos.	Eff. dist.	Ads. En.* (eV)	Rel. En.** (eV)	E_F (eV) (eV)	splitting (eV)	c/n
0	0	-2.33	1 x Single H			
		-4.66	2 x Single H			
1	1	-6.111	-1.45088	-2.078	-	c
2	1	-5.816	-1.15598	-2.264	1.4	c
3	2	-4.691	-0.03138	-2.033	0.15	n
5	3	-5.800	-1.14078	-2.298	1.4	c
8	4	-4.572	0.08802	-2.042	0.05	n
4	3	-4.581	0.07852	-2.021	0.2	n
6	3	-4.946	-0.28638	-2.169	0.45	c
9	4	-4.571	0.08802	-2.014	0.12	n
10	5	-5.061	-0.28638	-2.238	0.4	c
11	6	-4.653	-0.08932	-2.020	0.05	n
12	7	-4.903	-0.24338	-2.091	0.45	c

Table 4.2: Calculated adsorption energies, Fermi levels and level splittings for adatom-adatom configurations as a function of the position (Pos.) of the second adatom w.r.t the position "0" of the first adatom in Fig. 4.15 a). The separation between-adatoms (Eff. dist.) is defined as the number of bonds in graphene lattice on the migration path of the second adatom to arrive at site "0". * The adsorption energy (Ads. En.) is calculated with respect to the system nanotube + H + H (all isolated), and ** The relative energy (Rel. En.) is calculated with respect to nanotube + two separated H-adatoms. c/n is used for cusp/node.

Figs. 4.15 a) and 4.14 a). The difference in energies corresponding to different adsorption positions was more than 1 eV at small separations (positions "0-2" and "0-5", in agreement with recent results for graphite [99,100]). The difference clearly originates from electronic effects, as (i) H-adatoms do not give rise to a large distortion of the lattice, so that interaction through strain fields can be excluded; (ii) the maxima- minima structure perfectly matches the cusp-node pattern in the electron density near a single adatom. The saw-tooth dependence can be understood in terms of the different amount of π-electron density available near the Fermi level for making a bond between the nanotube atom and the second H-adatom.

A similar phenomenon of substrate mediated long-ranged oscillatory interaction was previously reported for adatoms on metal surfaces [122]. However, such a result is somewhat unexpected for a semiconducting system, as the new states should be more spatially localized near the defect than in a metal system. Although the simulated nanotubes were too small to quantitatively extrapolate the dependence to large adatom separation, one can assume from tight-binding simulations for bigger systems [110] that the interaction is effective in a range of up to dozen nanometers, coinciding with the extension of electronic superstructures near the defects.

Adatom-adatom interaction gives rise to another salient feature: the H-adatom-induced states split into two peaks in the LDOS which are symmetric with the mid-gap level, as shown in Figs. 4.14 d)-g). Depending on the adatom-adatom separation, the position of the peaks can be in the middle of the gap (deep levels), Fig. 4.14 g), close to the band edges (shallow levels), Figs. 4.14 d) and f), or at the band edges, Fig. 4.14 e). All these positions are metastable (separated by energy barriers from each other) so that all of them can exist at the experimental temperature of about 5 K. The structures presented in d), f) and g) are in very good agreement with the measurements, and can be associated with the double peak spectra D1-D2, D3-D4, D7-D8 (deep levels, g)) and D5-D6, D9-D10 (shallow levels, d) and f)) presented in Fig. 4.12. An important feature can be seen in Fig. 4.15 c): the splitting energy is proportional to the adsorption energy for the second adatom and thus to the strength of the adatom-adatom interaction. In a certain way, the double peak structure can be understood in analogy to the bonding-antibonding orbital splitting of the H_2 molecule, where in our case the interaction between the two H atoms is mediated by the SWNT electrons. All the calculated energy values (adsorption energy, splitting energy and Fermi energy) for each H adatom-adatom configurations presented in Fig. 4.15 a) are summarized in Table 4.4.3.2.

Our results indicate that the H-adatom adsorption energy is different if there is already another adatom nearby, with the interaction being non-monotonously dependent on the separation. As adatom-adatom interaction

changes the sticking coefficients for H on graphite [100], this is also likely to happen in SWNTs, thus explaining the abundance of double-peak structures. The interaction should also affect adatom diffusion[1] and hydrogen desorption (e.g., due to additional barriers for diffusion from site "5" to site "0" via site "3"). Assuming that the chemisorption mechanism is more important than molecular physisorption [85], the adatom-adatom interaction should also affect the maximum hydrogen uptake in nanotubes. Note that this effect is not taken into account in numerous Monte-Carlo simulations of hydrogen-nanotube interaction.

4.4.4 Other defect structures

As we pointed out in the previous sections, the most commonly observed electronic signatures for low energy H-plasma-induced defects are single states in the bandgap or at the band edges and paired, mid-gap symmetric states. However, in some rare cases, we observed defect-induced electronic signatures which are markedly different from the standard ones.

A first example is shown in Fig. 4.16 a) with a dI/dV-scan recorded along the horizontal dashed line running over three defect sites (d1-d3) on a semiconducting $(8,4)$ SWNT (upper panel). The defect site d1 gives rise to two narrow and intense peaks P1 and P2 in the VB region, with energy positions E(P1) = -0.29 eV and E(P2) = -0.63 eV. The dI/dV spectrum recorded at the position indicated by the black circle on d1 is displayed in c). The measured FWHM is ∼50 meV for both peaks. From *ab initio* calculations, we found a similar electronic signature for a single vacancy with its saturating bond nearly parallel to tube axis, decorated with one hydrogen atom. The ball-and-stick model of this structure for a $(10,0)$ SWNT is shown in Fig. 4.4.4 d) with the saturating bond highlighted in red, and the corresponding LDOS is displayed in Fig. 4.4.4 b). The origin of this double peak structure is due to a dispersive band a the VBE (see appendix B). The same defect configuration for for a $(8,0)$ SWNT shows a similar feature, but positions and intensities of the peaks are slightly different, indicating a chirality dependence. Note that vacancy configurations with the saturating bond nearly parallel to the tube axis are energetically less favorable than the "perpendicular" configuration described earlier. The differences in the

---

[1]The desorption barrier for the H-adatom on graphite is slightly lower than the diffusion barrier [100], implying that the adatom will desorb rather than diffuse upon heating. At the same time, it is well known that nanotube curvature increases the adsorption energies [102, 103] and makes the diffusion of adatoms anisotropic [31]. Although one may expect that the barriers for diffusion perpendicular to the tube axis will increase, the diffusion parallel to the tube axis should be roughly the same as in graphite. Thus, the diffusion mechanism for adatoms on nanotubes should be active and could explain the abundance of dimers with low hydrogen irradiation doses.
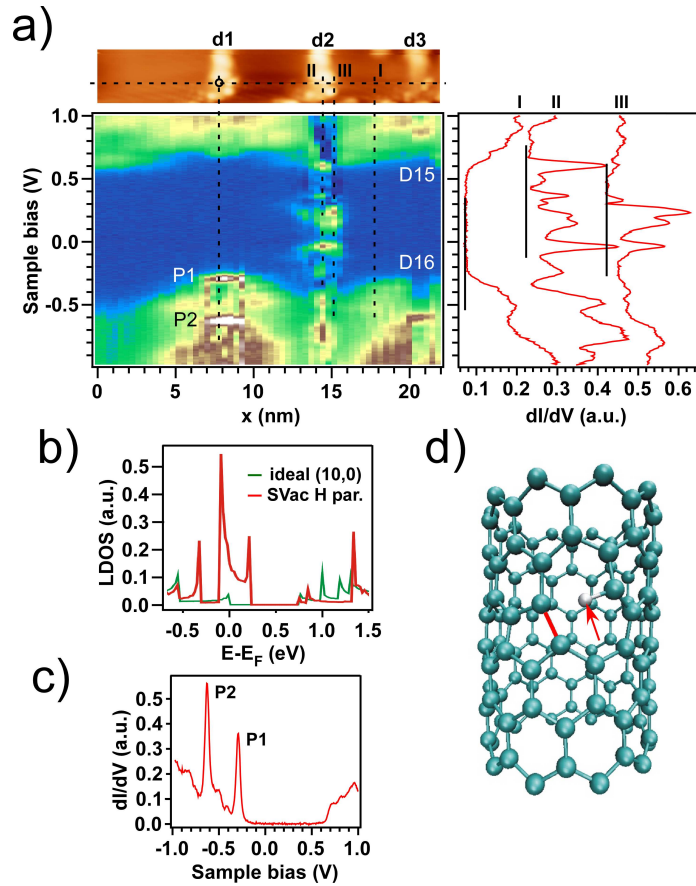
Figure 4.16: *a) STM topography image of a (8, 4) semiconducting SWNT treated with low-energy hydrogen plasma and corresponding dI/dV-scan recorded along the horizontal black dashed line. Three dI/dV spectra recorded on and near d2 are displayed on the right hand side. b) Calculated LDOS for SV decorated with one H-adatom. c) dI/dV spectrum recorded on d1. d) Ball-and-stick model of a (10, 0) SWNT with a SV decorated with one H-adatom.*

total energy between "parallel" and "perpendicular" configurations are 0.27 eV and 0.15 eV for the (10, 0) and (8, 0) tubes, respectively. Ball-and-stick models, band structure and LDOS for different "parallel" configurations with 0, 1 and 2 decorating H are given in appendix B.

The electronic signature in the differential conductance for the defect site d2 shows a quite complex structure with several peaks distributed in

the whole bandgap. To get a better insight into the behavior of this features, we plotted the dI/dV spectra recorded along the vertical black dashed lines, labeled with the roman numerals I to III, over and near d2. Interestingly, one can observe that d2 also induces a metallization in the band gap. However, care must be taken because of the NDR-induced artifact. Indeed, an analysis of the I-V curves at the x-positions corresponding to the defect site d2 shows a NDR behavior at the energy positions above the intense peaks positioned at about 0.35 eV and 0.7 eV. The NDR behavior strongly hinders a correct interpretation of the dI/dV curves above these energy values. Nevertheless, as we will see in chapter 7, for a generally accepted flat DOS of the tip, the NDR behavior only occurs above the Fermi level and thus the metallization in the bandgap below the Fermi level is considered as real. To be able to identify the nature of the defect giving rise to such a complex electronic signature, one must now consider stable configurations of combinations of vacancy and H-adatom defect types. Since this type of electronic signature has been observed only one time among more than a hundred of investigated H plasma-induced defect sites, we did not judge indispensable to perform such calculations in the framework of this thesis.

A double peak structure D15-D16 appears at the position of the defect site d3, with each individual peak located inside the bands, *i.e.* in the CB for D15 at $E = 0.87$ eV and in the VB for D16 at $E = -0.61$ eV. This electronic signature for d3 is in good agreement with the calculated electronic signature for a H dimer with a separation of one bond length corresponding to the configuration shown earlier for the $(10,0)$ SWNT in Fig. 4.14 e) (position 2 in Fig. 4.15 a)).

4.4.5 Spatial intensity modulation and peak shift

Up to this point, we have discussed the local modifications of the defect-induced electronic structure of semiconducting SWNTs on the basis of dI/dV-scans recorded on x-intervals ranging typically from 10 nm up to 30 nm. In this paragraph, we will succinctly describe two effects which can be observed from spectroscopy analysis concentrated on the spatial extent of the defect site. Figure 4.17 a) shows topography and current error signal images of a defect site on a $(10,0)$ semiconducting SWNT. A detailed image (line by line flattened), 5 nm $\times$ 3.3 nm in size, of the defect site pattern is displayed in Fig. 4.17 b). Ten single point dI/dV spectra have been recorded at the positions indicated by the black triangles, on three well separated regions showing particular topographic features. The corresponding spectra, vertically offset for clarity, are displayed in Fig. 4.17 c). The spectra recorded at different locations on the same defect site individually show quite complex features with one to three pronounced peaks located
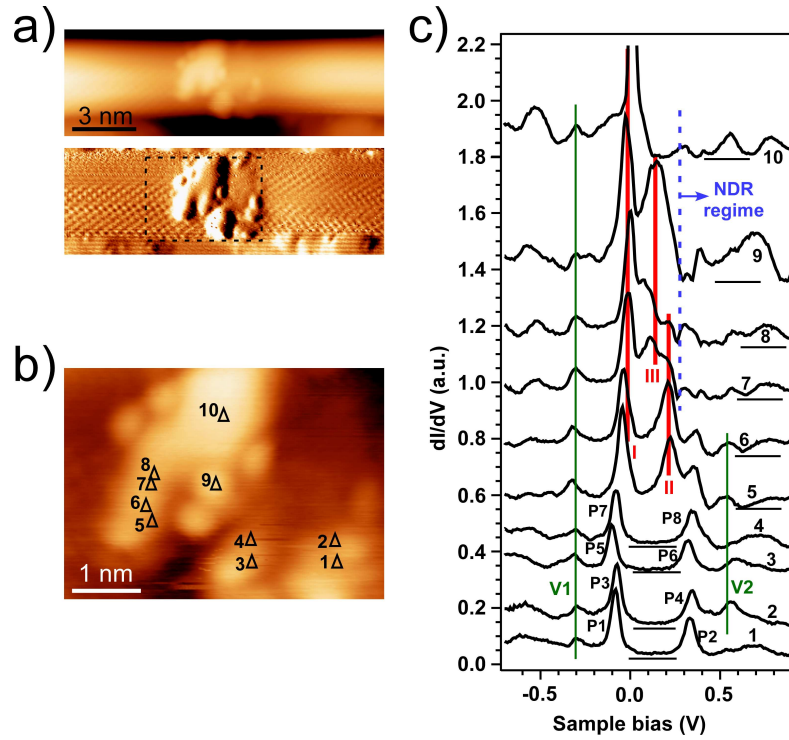
Figure 4.17: *a) upper panel: Topography STM image of a semiconducting $(10,0)$ SWNT, $\Delta z = 0.8$ nm, $V_s = 1$ V, $I_s = 0.3$ nA, $T = 5.28$ K, lower panel: current error signal image. b) Line by line flattened image of the zone inside the black dashed square drawn in a), single dI/dV spectra have been recorded at the locations of black triangle 1-10. c) Recorded dI/dV spectra vertically offset for clarity.*

at different energy positions between about -0.1 eV and +0.4 eV. Before discussing this behavior in more details, let us remind some fundamental theoretical principles. In any quantum-mechanical system, the spectrum, *i.e* the position of the energy levels, contains the information of the whole system, and the local density of states as measured in STS can be written by [58]:

$$\rho_{\mathrm{s}}(\vec{\mathbf{r}}, E) = \sum_{\nu} |\psi_{\nu}(\vec{\mathbf{r}})|^2 \, \delta(E - E_{\nu})) \qquad (4.5)$$

where the delta function defines the positions of energy levels. The square of the wave function defines the amplitude of the density of state at the energy E_{ν} and the coordinate $\vec{\mathbf{r}}$. To illustrate this, Fig. 4.18 shows the
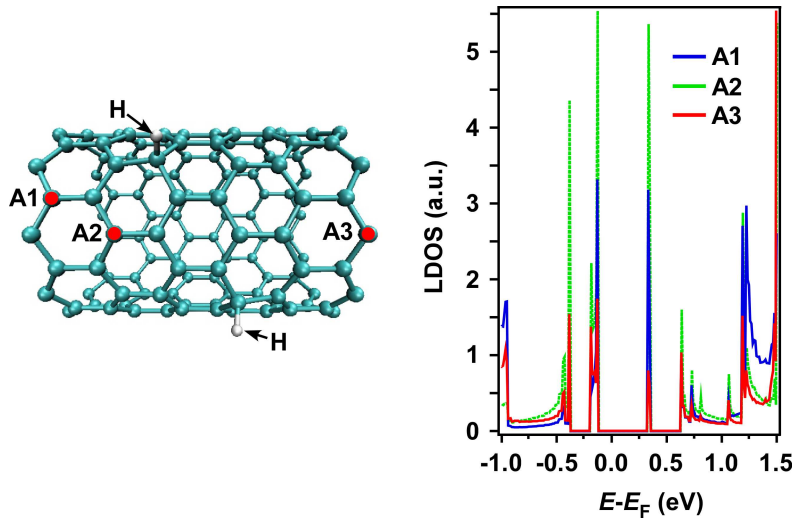
Figure 4.18: *Left panel shows a ball-and-stick model of a* (10, 0) *SWNT with two adsorbed H atom corresponding to the configuration presented in Fig. 4.15 a), position 10. The LDOS on atoms highlighted in red, A1-A3, was calculated and displayed in the right panel.*

LDOS calculated at different spatial locations on a (10, 0) SWNT with two H-adatoms corresponding to the configuration presented in Fig. 4.15 a), position 10. The intensity of the typical mid-gap paired peaks pair is clearly modulated as a function of the atomic position on which the LDOS is calculated, with a maximum intensity at position A2 close to the dimer structure (3 bond lengths from the upper H-adatom) and a decrease of the peak intensity by more of a factor 3 at position A3 (7 bond lengths from the upper H-adatom). Whereas the intensity of the features in the LDOS changes as function of the position, the characteristic energies remain unchanged.

Now, if we look at the position of the different measured peaks on the defect site in Fig. 4.17 b), we can make the following observations:
(i) Spectra 5-10 each show an intense peak with its position slightly oscillating around the position of the red line I at E_{avg} = -17.3 meV with E_{max} = 10.7 meV for spectrum 10 and E_{min} = -42.7 meV for spectrum 5.
(ii) Spectra 5 and 6 each show an intense peak and spectra 7 and 8 a shoulder with their position slightly oscillating around E_{avg} = 209 meV, highlighted by the red line II.
(iii) Spectra 7 and 9 each show a peak and spectrum 8 a shoulder with their position slightly oscillating around E_{avg} = 0.1175 eV, highlighted by the

red line III.

(iv) Spectra 1-2 and 3-4 individually show a pair of peaks symmetrically positioned w.r.t. the first VHS highlighted by green vertical lines V1 and V2.

Note that the line V2 is drawn only on the six first spectra because I-V curves for spectra 7-10 show a NDR behavior above 0.25 V, hindering a correct interpretation of the dI/dV features above 0.25 V (blue curve).

On the basis of Eq. 4.5, we can attribute the intensity modulation of the peaks at positions II and III to the same effect of the spatial modulation shown in Fig. 4.18. This means that the defect structure is composed by a combination of defects, vacancies or/and adatoms spatially separated such that the tip can more or less "feel" the different defect-induced states as a function of its position on the whole defect site.

Note that a shift of the same order of magnitude of about 0.02 eV is also observed between peaks P1-P3 and between P2-P4 from the pattern on the bottom right (1-2) of Fig. 4.17) and between peaks P5-P7 and P6-P8 from the pattern at the bottom in the middle (3-4). Such small peak shifts were often observed for single point spectra recorded at different locations on adatom-adatom-induced defect patterns.

Another more significant example of energy position shift of defect-induced peaks can be seen in Fig. 4.19. Here a dI/dV-scan has been recorded on a range of about 3 nm along the long black dashed line running over a defect site on a $(4, 8)$ semiconducting SWNT displayed in a). Figure 4.19 b) shows the recorded corrugation of the defect site. Since the modulation in x-direction of the dI/dV features follows the corrugation, it can be attributed to the same corrugation-induced artifact discussed in section 4.4.1.2. The important observation here is the strong spatial shift in energy of one single feature in the dI/dV-scan. Other features are energy split peaks at the band edges, which are reminiscent of the earlier discussed lifting of the band degeneracy. Further, we have a state with rather constant (0.1 eV) energy position close to the Fermi energy and the state with varying energy (0.25 eV) in the negative bias range for $x < 1.5$ nm.

The observed energy position shifts of defect-induced peak structures as a function of the position in Figs. 4.17 and 4.19 can not be explained within Eq. 4.5. A possible explanation could originate from taking into account the influence of the tip on the geometrical structure of the defect. Since we know that nanotubes experience a local mechanical compression arising from forces exerted by the tip on the SWNT wall [80], a local deformation of the defect structure like *e.g* a change of the bond angle of a H-adatom or the change of the bond lengths around a vacancy type defect as a function of the tip position can be expected. In this respect, one could tentatively
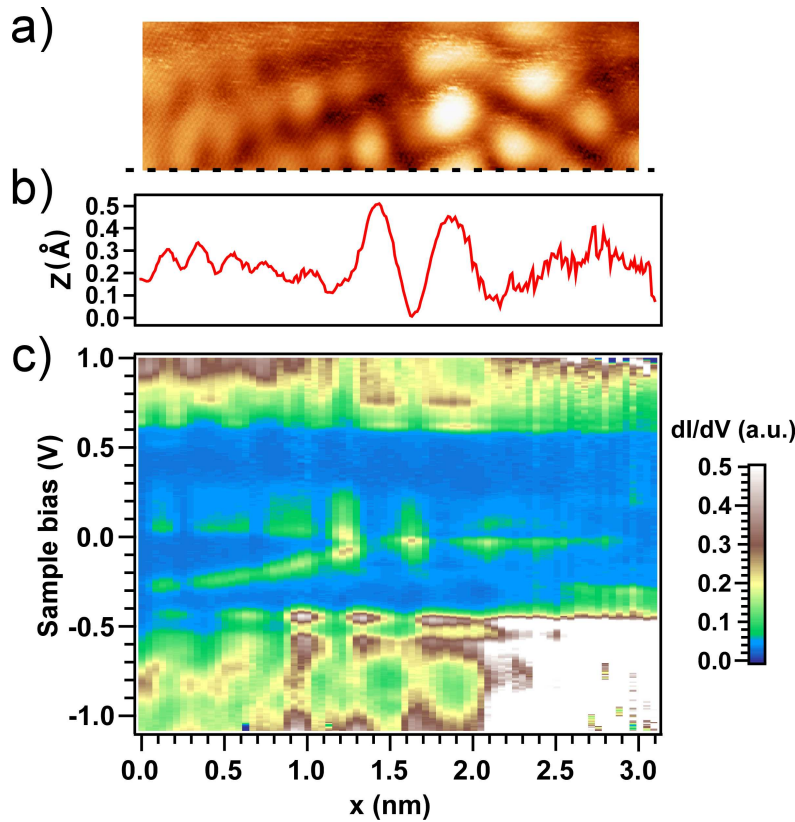
Figure 4.19: *a) Detail togography STM image of a defect site on a (4, 8) semiconducting SWNT. b) Tip-tube distance z recorded along the horizontal dashed line drawn in a). c) dI/dV-scan recorded along the horizontal dashed line. $T = 5.25$ K, $V_s = 1$ V, $I_s = 0.25$ nA, $x_{res} = 0.1$ Å.*

interpret the measurement displayed in Fig. 4.19 as showing a binary defect system (giving rise to two low dispersive states), where only one component strongly experiences the tip interaction during the recording of the dI/dV-scan. It would be worth investigating this idea further, *e.g* carrying out spectroscopic investigations of defects as a function of the STM setpoint parameters and therefore varying the tip-sample distance and interaction. These experimental investigation should be accompanied by DFT calculations taking into account the STM tip-defect interaction as a function of the tip position.

4.4.6   Metallic SWNTs

For hydrogen ECR plasma treated SWNTs, we observed the most interesting effects on semiconducting tubes. From the theoretical point of view, metallic tubes with defects have not been studied at length in this work, as accurate calculations of metallic systems require a finer grid of k-points near the Fermi level for BZ integration, which results in a prohibitively high computational cost. Spectroscopy measurements on defects often revealed the presence of peak structures (single or multiple) close to the Fermi level. Figure 4.20 a) shows a STM topography image of a metallic $(13, 4)$ SWNT with two defect sites d1 and d2. A detailed image of the defect site d1 is displayed in panel b). Eight single point dI/dV spectra have been recorded on the same tube at the positions indicated by black triangles. The corresponding spectra, vertically offset for clarity, are shown in panel c) and d). Spectrum 1 represents the LDOS of the clean tube with a non-zero LDOS at the Fermi energy, indicating the metallic character of the tube. The onsets of the first VHS are spaced by about 1.05 eV. At different positions on the defect site d1 (2-5), the corresponding dI/dV spectra show different peak features, with a common intense peak close to E_{F}, at -0.03 eV, in each spectrum. These peak signatures in the LDOS are confined on the defect site, which is also corroborated by the fact that very close to the defect, the LDOS returns to normal as evidenced by spectrum 1. Another electronic signature is shown in panel d) by spectra 6 and 7 recorded on the defect site d2. Here a single pronounced peak appears above the first VHS. A simulation of the LDOS based on a TB Green's function technique for the tip positioned on a single vacancy in a metallic $(10, 10)$ SWNT was reported in the literature [40] and is presented in Fig. 4.20 e). As explained above in sect. 4.4.1.1, the calculated increase in the LDOS near E_{F} is due to the dangling bonds states close to E_{F}, spatially localized on the atoms surrounding the vacancy [118]. The result of this simple TB calculation is close to what is observed in spectrum 2. However, further ab initio calculations of possible defect structures on metallic SWNTs, *i.e.* H-adatoms and vacancies, are needed to identify the exact nature of d1 and d2, and also to understand the nature of the satellite peaks below E_{F} in spectra 4 and 5. Note that these occupied states show up at different energy positions for the two spectra 4 and 5 recorded at close spatial locations on d1.

4.5   Superstructure patterns

Figure 4.21 a) shows a STM topographic image at $V_{\mathrm{s}} = 1$ V and $I_s = 0.3$ nA of a semiconducting SWNT in a bundle with three defect sites labeled d1-d3. Figure 4.21 b) displays a detailed image at $V_{\mathrm{s}} = 0.63$ V in the region
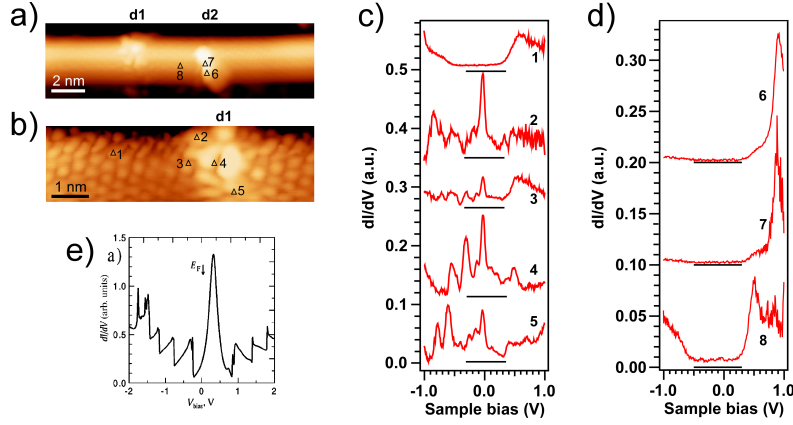
Figure 4.20: *a) Topography STM image of a metallic* $(13, 4)$ *SWNT with two defect sites d1 and d2,* $V_s = 1$ *V,* $I_s = 0.1$ *nA,* $\Delta z = 7$ *Å. b) Detail topography STM image of d2,* $V_s = -0.05$ *V,* $I_s = 0.1$ *nA,* $\Delta z = 3.2$ *Å. c) and d) Single point dI/dV spectra recorded at positions 1-8 in a) and b). Spectra are vertically offset for clarity. e) LDOS for a single vacancy in a* $(10, 10)$ *tube, based on TB Green's function calculation, taken from [40].* $T = 77$ *K.*

between defects d2 and d3, separated by about 6 nm. The image is corrected in order to compensate tip-tube convolution effects (this is performed for all STM images in Fig. 4.21). A $\left(\sqrt{3} \times \sqrt{3}\right) R30°$ superstructure of the local density of states, indicated by the large unit cell (blue), is clearly visible. To the left-hand side of d3, the superstructure contribution decays with a characteristic length of about 5 nm and the usual graphene unit cell is visible again. A second example for a semiconducting SWNT with two defect sites d4 and d5 is shown in Fig. 4.21 c). The setpoint parameters are $V_s = 1$ V and $I_s = 0.3$ nA. A very similar pattern for the $\left(\sqrt{3} \times \sqrt{3}\right) R30°$ reconstruction is clearly visible on the right hand side of d5 and the left hand side of d4, with characteristic extends of about 4 nm and 2 nm, respectively. The reconstruction is also present on the entire region of about 2.5 nm between the defects, but shows a different pattern.

In Fig. 4.21 d), we can see two metallic tubes in a bundle, presenting two different $\left(\sqrt{3} \times \sqrt{3}\right) R30°$ reconstruction patterns on both sides of defect zones. On both tubes, the superstructure continuously evolves into the primitive lattice beyond about 8 nm. On HOPG [98], the different observed $\left(\sqrt{3} \times \sqrt{3}\right) R30°$ reconstructions patterns could be reproduced by a linear combination of six plane waves having vectors $\mathbf{k}_j$ corresponding to the six
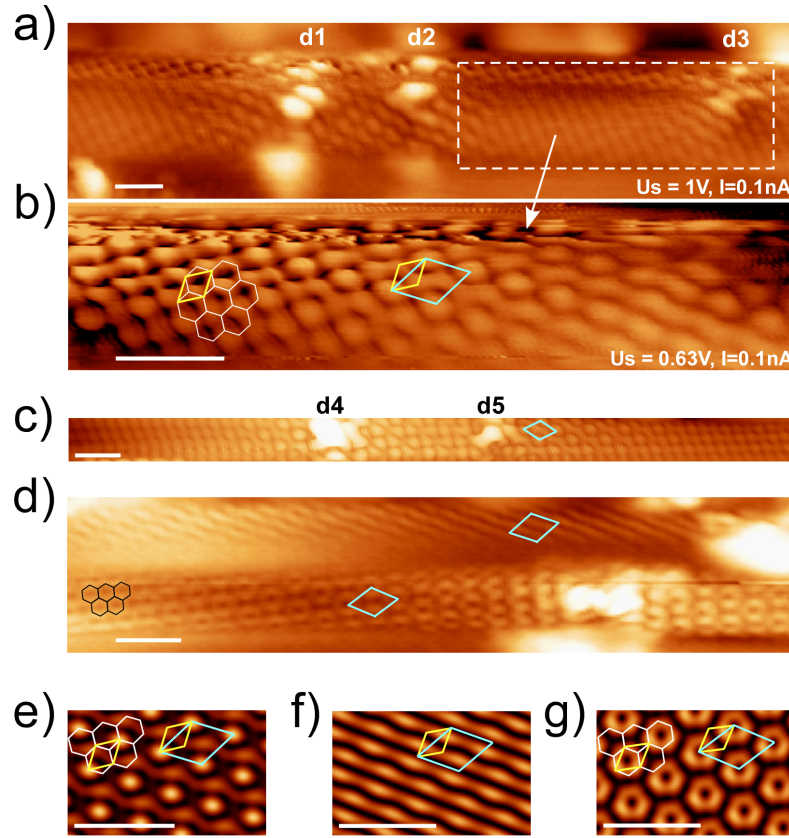
Figure 4.21: *a) STM topography image of a semiconducting tube in a bundle, with three defect sites labeled d1-d3, $V_s = 1$ V, $I_s = 0.1$ nA, $\Delta z = 2.4$ Å. The image is flattened line by line for better contrast and corrected to compensate tip-tube convolution effects (this is made for all following images). b) Detail STM image showing the region inside the dashed rectangle in a), between d2 and d3, $V_s = 0.63$ V, $I_s = 0.1$ nA. The 1×1 (yellow), $(\sqrt{3} \times \sqrt{3})R30°$ (blue) unit cells and the unperturbed honeycomb lattice (white) on the left hand side are evidenced. c) Semiconducting SWNT with 2 defect sites d4 and d5, $V_s = 1$ V, $I_s = 0.1$ nA. d) Two metallic SWNTs in a bundle, $V_s = 1$ V, $I_s = 0.1$ nA. e)-g) Calculated spatial maps of $|\psi(\mathbf{r})|^2$ according to Eq. 4.6. Appropriate values of the complex numbers ϕ_j have been selected to match the experimentally observed patterns in b) and d). The measurement temperatures are 77 K for a), b) and d), 5.3 K for c). The scale bar in each image is 1 nm.*
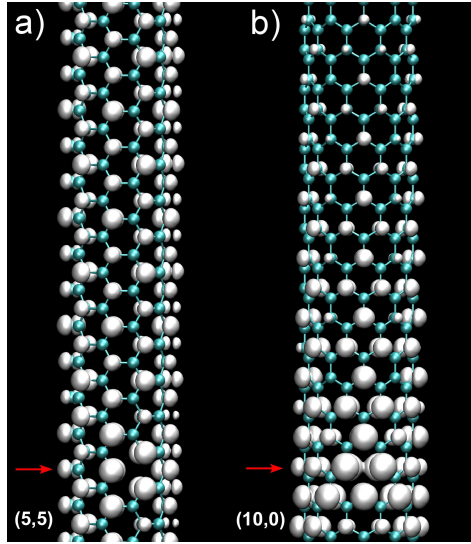
Figure 4.22: *a) Isosurface of the HOMO in a metallic (5,5) SWNT with a SV at the position of the red arrow. b) The same for a semiconducting (10,0) SWNT.*

Fermi vectors of the first BZ:

$$\psi\left(\mathbf{r}\right) = \sum_{j=1}^{6} \phi_j \cdot e^{i\mathbf{k}_j \cdot \mathbf{r}} \tag{4.6}$$

It could be concluded that the interference patterns originate from large momentum scattering of the electron wave functions at the defects, where the scattering vector of $2\mathbf{k}_F$ is reduced to k_F by an Umklapp process [98]. The expression given by Eq. 4.6 can also explain the reconstruction patterns on metallic SWNTs because of the band crossing at the Fermi points. In Figs. 4.21 e) and f), appropriate values of the complex coefficients ϕ_j in Eq. 4.6 have been selected so that $|\psi\left(\mathbf{r}\right)|^2$ matches the experimentally observed $\left(\sqrt{3} \times \sqrt{3}\right) R30°$ reconstruction patterns on the metallic SWNT in Fig. 4.21 d). For semiconducting tubes such as in Fig. 4.21 b) and c), theoretical investigations report the presence of hillock-like features and superstructures near vacancies due to the contribution of the band edges [40]. Even tough the model described by Eq. 4.6 must be modified to take into account the nature of the wave functions present at the band edges, it is possible to simulate the reconstruction pattern observed on the semiconducting SWNTs in Fig. 4.21 b), as shown in e). The patterns observed between d4 and d5 in c) could also be reproduced (not shown). All these observations lead to the conclusion that the plasma-induced defects act as in the case of HOPG as large momentum electron scatterers on the SWNT.
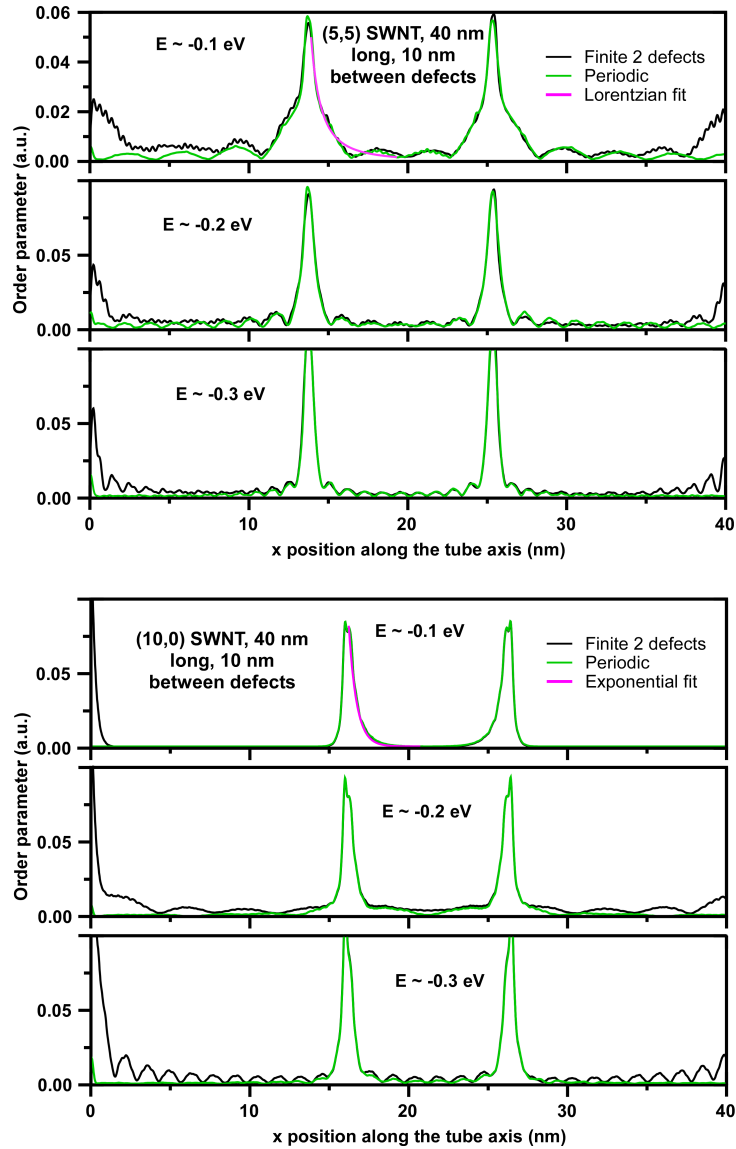
Figure 4.23: *Behavior of the order parameter O(x) (averaged around the tube at position x) along the tube axis for the (5,5) (upper panel) and the (10,0) (lower panel) and for different bias along the occupied states.*

In order to understand the different decay lengths for semiconducting and metallic nanotubes, we performed simple orthogonal TB simulations on extended systems, using the program TBPW [123] with simple nearest-neighbor interaction and a single hopping parameter t. This approximation is valid in particular close to the Fermi level, as shown for example in [124] or in [17]. For the simulation we considered different SWNTs chiralities. Here, we show results on a $(5,5)$ metallic SWNT and a $(10,0)$ semiconducting one. Our simulation cell included more than 3000 atoms for a total length of the tubes of around 40 nm. We considered both infinite tubes (with the use of periodic boundary conditions) and finite ones (with no boundary conditions). We created simple topological defects by removing a single carbon atom in two equivalent positions along the tube at a mutual distance of about 10 nm. After diagonalization of the secular TB matrix, we obtained a set of eigenvalues (the energy levels) and eigenvectors (the states). The electronic density pertinent to the different states can then be plotted in form of charge density isosurfaces for single states or for an integral over a range of energies, thus mimicking the outcome of an STM measurement in the Tersoff-Hamann approximation [81]. In Fig. 4.22 we show an isosurface for the highest occupied molecular orbital (HOMO) in the metallic (a)) and semiconducting (b)) cases.

As can be seen from Fig. 4.22, the presence of a vacancy-type defect breaks the symmetry of the two sublattices and an enhanced charge density on the the sublattice complementary to the one on which the vacancy is located can be observed. This is analog to the results of the *ab initio* calculation of a single H-adatom. This charge redistribution has a certain range which is markedly different for the HOMO of the metallic and semiconducting tubes displayed in Fig. 4.22. In order to characterize the decay of this charge redistribution as a function of the distance from the defects, we introduced an order parameter based on the charge unbalance between atoms lying in different sublattices. This "antiferromagnetic" order parameter is defined as:

$$O(i) = \frac{1}{3} \cdot \sum_j |(q(i) - q(j)|$$
(4.7)

with j ranging on the 3 nearest neighbors of atom i, and $q(i)$ the electronic charge on atom i. This parameter reaches its maximum when one has a maximum of charge on one sublattice, and no charge on the other. Figure 4.23 shows the behavior of $O(x)$ (averaged around the tube at position x) along the tube axis for the $(5,5)$ and the $(10,0)$ and for different bias along the occupied states (please note that in this orthogonal TB approximation, occupied and unoccupied states are equivalent). We note that the range of the charge redistribution is larger in the metallic case than in the semi-

conducting one. We found a best fit with a Lorentzian for the $(5, 5)$ tube and with an exponential for the $(10, 0)$. This finding is in good qualitative agreement with the presented experimental observations in Fig. 4.21, in the sense that the range of the electronic charge redistribution is smaller for semiconducting than for metallic tubes. At this stage the TB model for a SV does not reproduce a very pronounced $\left(\sqrt{3} \times \sqrt{3}\right) R30°$ reconstruction. Nevertheless, this reconstruction is present for the metallic tube in Fig. 4.22 a). Further development of the model, *e.g.* by including next nearest neighbors hopping in a non-orthogonal TB and taking into account the tube-substrate interactions [75], as well as different tubes and defect configurations will be needed to hopefully achieve a quantitative agreement of the simulation with the experiment.

4.6   Summary and outlook

By combining LT-STM/STS with first principle computer simulations, we have shown that ECR hydrogen plasma treatment of SWNTs induces dramatic local changes in the LDOS, with the observation of new single or paired electronic states in the nanotube bandgap. Moreover, our results provide a direct evidence that the most often observed paired states originate from a correlated chemisorption of H-adatoms on the tube walls and that the energy splitting is governed by the adatom-adatom interaction.

The interplay between sticking, desorption and diffusion could be used to control the distribution of H-H-adatoms. Thus our results point out that partial hydrogenation of carbon nanotubes by using, e.g. masks, followed by annealing at pre-determined temperatures can be employed for engineering the electronic structure of nanotubes and creating paired states in the semiconducting gap. This has important implications in, for example, optoelectronics [125] where the gap states can act as local recombination centers for electrons and holes by emission of photons of well-defined energy.

A more general study of the interactions between adatoms can be performed with higher hydrogen coverage with the expectation to form clusters with more than two H-adatoms, like observed on HOPG by means of high resolution electron-energy loss spectroscopy (HREELS) [96]. However, to avoid the formation of vacancies and thus increase the risk to locally etch the SWNTs [94, 106, 107], the hydrogen ECR plasma source should be replaced by an atomic hydrogen source [102]. Such kind of experiments are of great interest to study the hydrogen uptake as a function of the tube chirality and diameter. A recent theoretical work reported that hydrogen atoms prefer to form chains on the the tubes wall [126].

Chapter 5

Nitrogen plasma-induced defects

In analogy to silicon-based microelectronics, achieving substitutional doping in SWNTs is a key issue towards a future SWNT-based nanoelectronics. N/B atoms are good candidates to achieve this goal since they have roughly the same atomic radius as C, while they possess one valence electron more/less. Recently, N implantation has been reported from X-ray photoemission and EELS investigations on 3 keV N_2^+ bombardment of SWNTs. Although signatures of substitutional N incorporation in the tubes could be found, this high energy implantation process leads to an undesirable high amount of additional structural damage. Here we study the effects of low energy ECR N-plasma exposure of SWNTs on the electronic structure with the hope to find signatures of local doping of the tubes.

5.1   Generation of defects

Similarly to the case of hydrogen plasma exposure, we first calibrated the optimal exposition parameters for a desired defect separation in SWNTs of about 10 nm on a freshly cleaved HOPG surface. At a horizontal distance of about 3 cm from the antenna axis, the desired defect density could be obtained for an exposure time of about 4-5 s at 7×10^{-2} mbar N_2 pressure and 60 W microwave power. Note that for the same position of the sample and a similar defect density, the exposition time for the hydrogen plasma is 1 s. The difference between exposure times for both plasma species is given by the complex interplay between recombination processes in the plasma and the interaction probability of the active plasma species with HOPG and SWNTs.

5.2   Semiconducting SWNTs

Figure 5.1 a) shows a line by line flattened STM topography image of a semiconducting SWNT after ECR nitrogen plasma treatment. Five defect sites labeled d1-d5 are visible in the imaged tube section of 30 nm in length. Generally, the observed shape, apparent height and spatial extent of the defect sites is similar to what we observed for H-plasma treatment. dI/dV-scans have been recorded along the two horizontal dashed lines labeled line0 and line1, and are displayed in Fig. 5.1 b) and c). Each defect site gives rise to new states at both VBE and CBE or/and inside the bands. We often observed such signatures in the differential conductance for N-plasma treated SWNTs. Note that the modifications of the electronic structure induced by defect sites d2 and d5 are visible in the dI/dV-scan recorded along line0 (b)) but not in the one recorded along line1 (c)) shifted about 5 Å upwards. This observation points out the very localized nature of the modified electronic structure.

Two other examples of N-plasma treated semiconducting SWNTs are displayed in Fig. 5.2. The upper panel shows the topography image of a $(8,0)$ SWNT with 6 defect sites labeled d1-d6. In the corresponding dI/dV-scan recorded along the horizontal dashed line, one can see that three defect sites (d1, d4 and d6) give rise to new gap states which are single peaks in the mid-gap region. For d1, two lower satellite peaks near the CBE are also visible. The FWHMs of the narrow gap states for d1, d4 and d6 are 68 meV, 78 meV and 58 meV, respectively. Defects d2 and d5 show new states at about 1.1 eV (in the CB) and -0.7 eV (in the VB), respectively. The electronic structure at d3 does not show dramatic changes compared to non-perturbed regions. In Fig. 5.2 b), the SWNT shows five defect sites d7-d11 distributed on a 40 nm long section. From the corresponding dI/dV-scan, it can be seen that d7-d9 show single states at the CBE (d7 and d9) or inside the CB (d8). On the other hand, d10 and d11 each give rise to a pair of intense and narrow peaks, one at the mid-gap region and the second one inside the VB. Note that the non-zero intensity features above both mid-gap peaks are dominated by the NDR behavior ($|dI/dV|$ is recorded). We identify the mid-gap peak visible at $x = 0$ to be a cap-induced state, as reported in an earlier theoretical work [27].

To summarize, for all the investigated semiconducting SWNTs exposed to a low dose ECR N-plasma, the observed defect-induced modifications of the electronic structure can be classified in two categories:

(i) Single states at the band edges (CBE or VBE) or inside the bands. On 51 defects investigated, this kind of feature occurred 34 times, *i.e.* in about 67% of the cases.
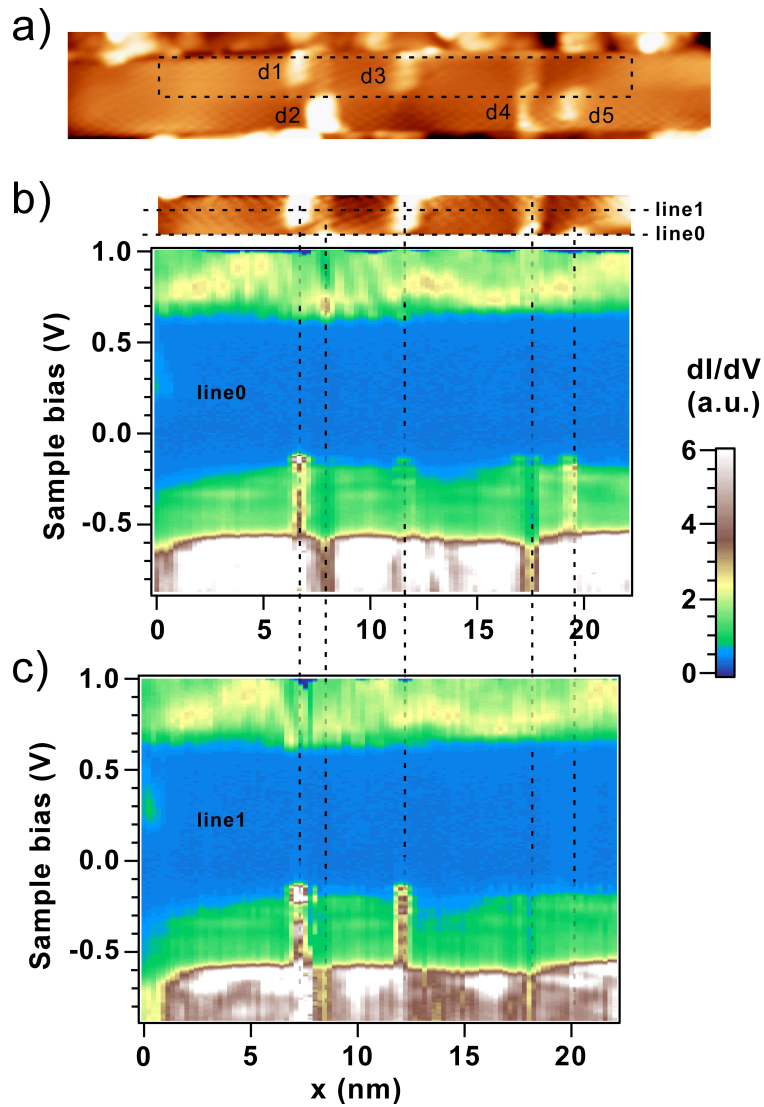
Figure 5.1: *a) Topography image of a semiconducting* $(8,6)$ *or* $(9,7)$ *SWNT, line by line flattened with five defect sites labeled d1-d5. The dI/dV-scans recorded along the horizontal dashed lines line0 and line1 in the detail image inside the dashed rectangle in a) are displayed in b) and c), respectively.* $U_s = 1$ *V,* $I_s = 0.35$ *nA,* $T = 5.22$ *K,* $U_{mod} = 13$ *mV,* $x_{res} = 0.22$ *nm.*
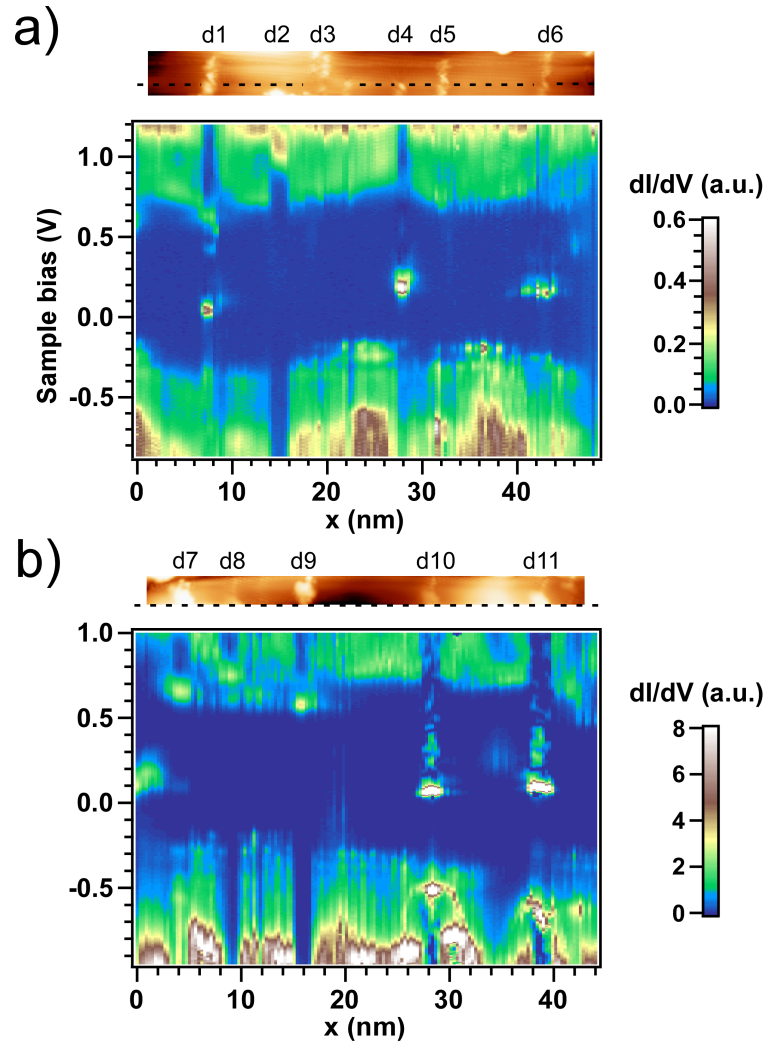
Figure 5.2: *a) Topography image of a semiconducting $(8, 0)$ SWNT with six defect sites labeled d1-d6. The corresponding dI/dV-scan recorded along the horizontal dashed line is displayed in the lower panel. $U_s = 1.2$ V, $I_s = 0.2$ nA, $T = 5.24$ K, $U_{mod} = 15$ mV, $x_{res} = 0.3$ nm. b) Topography image of a semiconducting $(4, 8)$ or $(5, 9)$ SWNT. The corresponding dI/dV-scan recorded along the horizontal dashed line is displayed in the lower panel. $U_s = 1$ V, $I_s = 0.3$ nA, $T = 5.2$ K, $U_{mod} = 15$ mV, $x_{res} = 0.28$ nm.*

(ii) gap structures mostly consisting of a single narrow and intense peak in the mid-gap region, with a frequency of about 33%.

We would like to point out that there is a significant difference between the ECR N- and H-plasma induced defects in the sense that for the nitrogen case we never observed the mid-gap symmetric paired gap states, which are so characteristic for the hydrogen case.

Ab initio simulations for the bombardment of SWNTs with N ions have been reported in [127, 128]. There, the threshold value of the kinetic energy needed to create a vacancy is calculated to be about 30 eV. Thus, for lower energies and without taking into account the neutralization process of the ions, only N-adatom defect types should occur. We have not measured the energy distribution of the N ions at the sample position, but we expect similar sub-threshold values as for hydrogen.

The electronic structures of different N-related defect configurations have been calculated for a $(10, 0)$ SWNT in a recent theoretical work [42]. The relaxed configurations with their corresponding band structures are reproduced in Fig. 5.3. For N-adatoms, the most stable configuration with an adsorption energy $E_a = 2.4$ eV is shown in e). The N-adatom is positioned above the middle of C-C bonds (bridgelike structure) oriented mostly perpendicular to the tube axis. The corresponding electronic structure is characterized by a new flat band at the Fermi level, similar to the case of a H-adatom. A less stable configuration with $E_a = 1.77$ eV is shown in d). Here the N-adatom is positioned above C-C bonds oriented in parallel with the tube axis. The corresponding band structure also shows a flat band at the Fermi level, but other bands crossing the Fermi level locally change the character of the tube to metallic. The "perpendicular" N-adatom configuration in e) is the most likely to explain the presence of mid-gap single peaks in our measurements.

The direct N substitution site shown in Fig. 5.3 b) gives rise to a new band located just above the Fermi level which exemplifies an *n*-type doping. The formation probability for a N substitution site is found to reach a maximum for a kinetic energy of the ions of about 50 eV. This probability falls abruptly for smaller energies and reaches zero for about 20 eV [127,128]. In our case, we never observed a clear rigid band shift towards lower energies, characteristic of a *n*-type doping. However, it is worth noticing that in the *ab initio* calculation above, the concentration on substitutional N is of the order of 1 per 80 C atoms, whereas the defect concentration we have investigated so far is about 1 per 1000 C atoms. As a consequence, even if sub-threshold processes could give rise to substitutional doping, it is not guaranteed that a local band shift will be observed for such a low defect
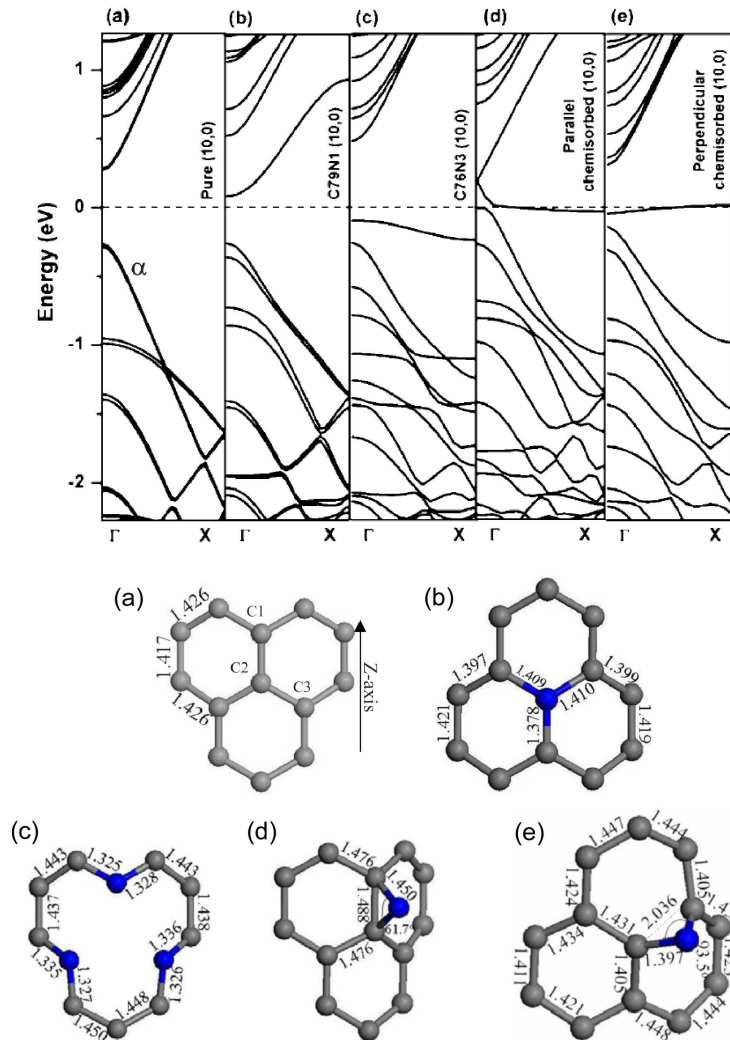
Figure 5.3: *Band structures of a semiconducting zigzag* $(10,0)$ *SWNT with 80 atoms/cell with different nitrogen related defect configurations. (a) Pure (10,0), (b) direct substitution of one N atom, (c) N substitution into the carbon framework with the formation of a vacancy: pyridinelike doping (d) chemisorption of one N-adatom in parallel position, (e) Chemisorption of one N-adatom in perpendicular position. Taken from [42].*

concentration.

The structure presented in Fig. 5.3 c), the so-called pyridinelike doping, gives rise to a flat state just below the Fermi level. However, its formation energy of about 6.5 eV makes it unlikely to occur in our case.

None of the configuration presented in Fig. 5.3 gives rise to flat bands at the band edges or inside the bands, which could explain the most commonly observed feature in the experimental dI/dV-scans. However, numerous energetically favorable structures with only one N atom are likely to appear [127], but their electronic structures have not been yet calculated.

Furthermore, it has been theoretically shown that N-adatoms are mobile at room temperature [127, 128] and thus the formation of N-clusters is possible. A detailed study on the structural stability and coalescence of two neighboring chemisorbed N-adatoms on a $(10, 0)$ SWNT based on *ab initio* calculations is given in [42]. The formation of N-N bonds can occur, resulting in different stable defect configurations like *e.g* pentagon-heptagon pairs. It has further been shown that the coalescence of two neighboring N-adatoms into a N_2 molecule needs to overcome an energy barrier in the range between 0.9 eV and 3.4 eV, depending on the N-chemisorption configuration and tubular diameter.

Thus, the electronic structure of many stable defects structures mentioned above must be calculated for different tube chiralities in order to find an explanation to the high abundance of experimentally observed peak structures at the band edges or inside the bands.

5.3   Metallic SWNTs

Figure 5.4 a) shows a STM topography image of a metallic SWNT exposed to low dose ECR N-plasma. A detailed image with seven defect sites d1-d7 is displayed in the upper panel of b). The corresponding dI/dV-scans recorded along the dashed horizontal lines labeled line0 and line1 are shown in b) and c), respectively. Similarly to semiconducting tubes, one can observe that each defect site modifies the electronic structure of the tube on a region corresponding to the spatial extent of the hillock features in the STM topography image. In general, each defect site gives rise to a quite pronounced peak just below (d2-d4,d6-d7) or just above (d1) the Fermi level with a modulation of the density of states on the entire bias range. Furthermore, some defect sites like d3, d4, d6 and d7 show the appearance of an intense and quite broad peak around 1 eV. Both features constitute the most commonly observed modifications of the electronic structure for SWNTs exposed to ECR N-plasma treatment. Band structure calculations from [42] for some typical defect configurations on a metallic $(5, 5)$ SWNT
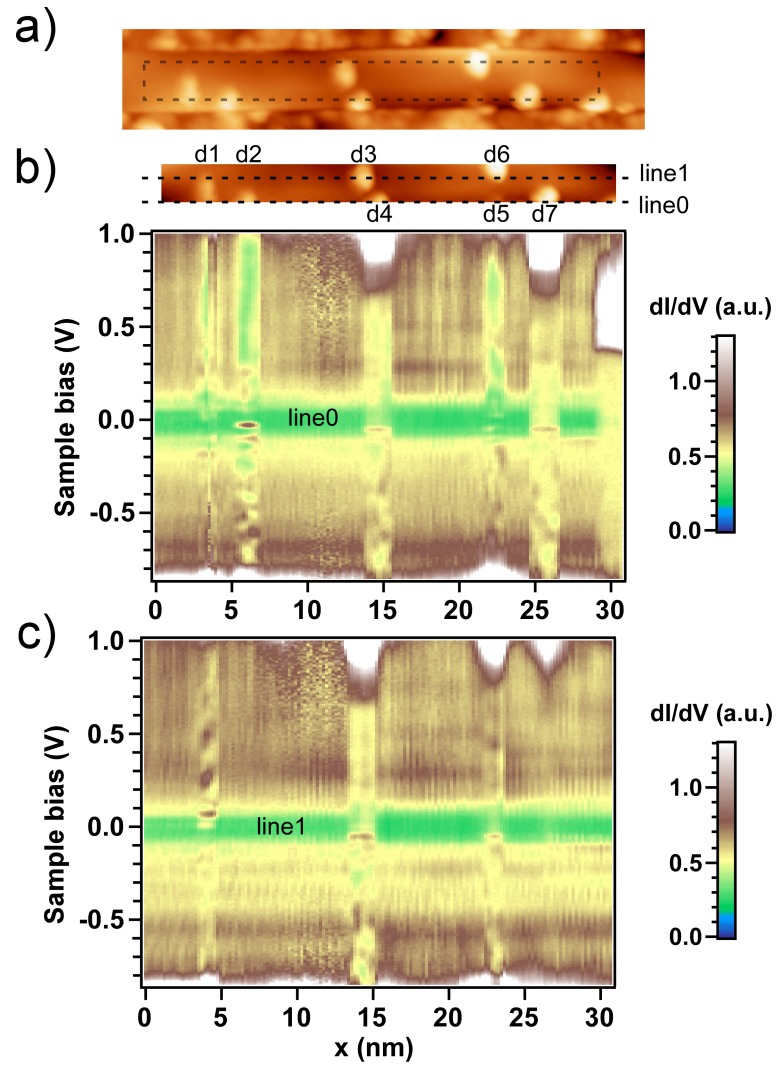
Figure 5.4: *a) STM topography image, line by line flattened, of a metallic ((8, 2) or (12, 3)) SWNT subjected to ECR N-plasma treatment. b) Detailed image of a zone in a) with seven defect sites d1-d7 and corresponding dI/dV-scans displayed in the lower panel and in b), recorded along the horizontal dashed lines line0 and line1, respectrively. $U_s = 1\ V$, $I_s = 0.4\ nA$, $T = 5.2\ K$, $U_{mod} = 15\ mV$, $x_{res} = 0.2\ nm$.*

are displayed in Fig. 5.5.

Interestingly, one can observe that both chemisorption defect types ("parallel" in (d) and "perpendicular" in (e)) show a flat band at the Fermi level, in good agreement with our observations. Furthermore it is known that naked vacancies give rise to a pronounced peak at the Fermi level [110] and we expect a similar behavior for possible N related vacancy-type defects. Gap opening, characteristic for N substitutional defects shown in Fig. 5.5 b) was not observed but their presence cannot be completely ruled out, according to the discussion on the defect density in section 5.2. Like for semiconducting tubes, band structure calculations for other possible defects like dimer configurations are needed in order to fully identify the structural nature of the observed defects.
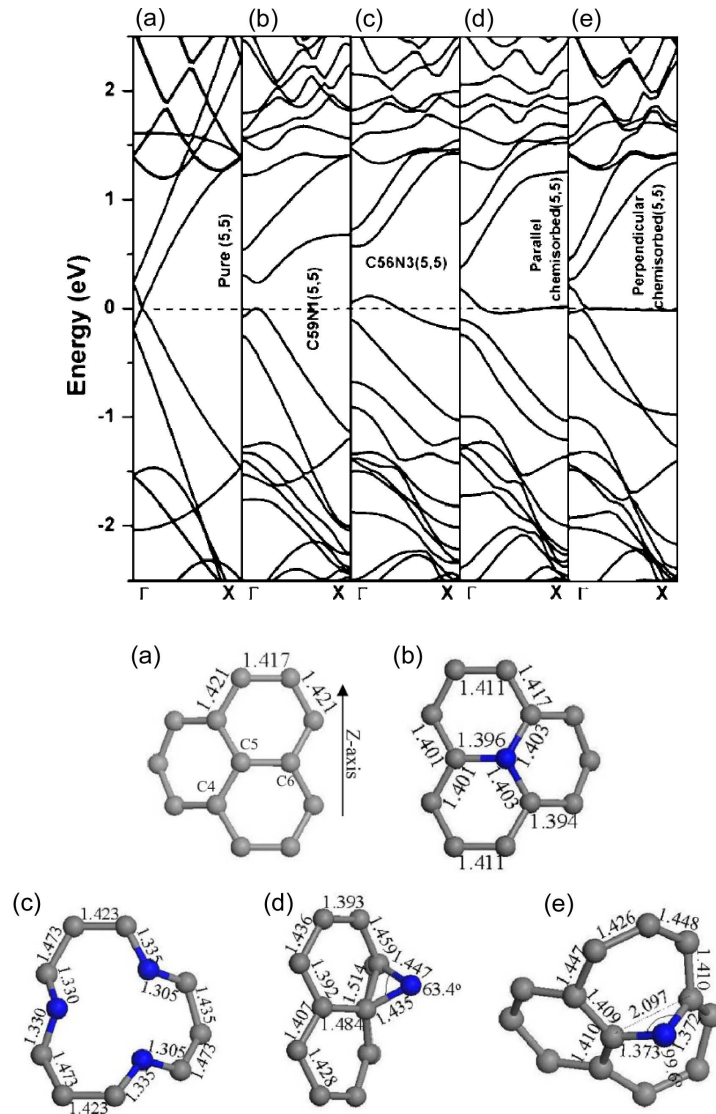
Figure 5.5: *Band structures of a metallic armchair $(5,5)$ SWNT with 60 atoms/cell with different nitrogen related defect configurations. (a) Pure $(5,5)$, (b) direct substitution of 1 N atom, (d) chemisorption of one N-adatom in parallel position, (e), chemisorption of one N-adatom in perpendicular position. Taken from [42].*

Chapter 6

Defects produced by Ar^+ ion bombardment

From the previous chapters, we could conclude that SWNTs exposed to low-energy ECR H and N plasma essentially give rise to adsorbate-type defects. The kinetic energy of the ions has been estimated to lie below the threshold value needed to create harsher defects like vacancies by sputtering off one or more C atoms. Our motivation to study vacancy-type defects has been further increased by a recent experimental work where the authors show that the creation of vacancy-type defects by medium energy argon ion irradiation on metallic SWNTs strongly increases their resistivity. Furthermore, it has been predicted that single vacancies (SV) only have a weak effect on the conductivity, whereas a concentration of only 0.03% of double vacancies (DV) produces an increase in the resistance of a 400 nm SWNT of three orders of magnitude [15]. This behavior could have important consequences in way to define confined electronic states in SWNTs (see chapter 9).

The experimental study of the local electronic structure of carbon nanotubes exposed to particles having a kinetic energy above the sputtering threshold energy has only been performed on MWNTs by means of STM/STS investigations in air and at room temperature [30]. From the theoretical point of view, a considerable number of computer simulations have been reported, especially concentrating on the formation mechanisms of heavy ion-induced defects and their mechanical and magnetic properties [129]. In this chapter, we report on LT-STM/STS investigations combined with *ab initio* calculations of medium energy Ar ion-induced defects on SWNTs.

6.1   Defect generation

The treatment using medium energy noble gas ions, in our case argon, allows a tuning of the amount of damage created in the defect zone by means of variation of the kinetic energy of the ions. We have investigated defects created by Ar ions with kinetic energies of about 200 eV and 1500 eV. It should be noted here that the ion gun we used in this study does not dispose of an energy filter and the stated ion energies are given by the acceleration voltage with respect to the DC glow discharge potential. This means that a considerable energy spreading of about 50-100 eV has to be expected. We used a standard Leybold^{TM} ion gun dedicated for UHV sputter cleaning of surfaces, which delivers a rather broad ion beam of about 15 mm in diameter on the sample position. Typical operating parameters of the ion gun are summarized in table 6.1. These parameters lead to an ion current of 1-2 μA·cm^{-2} at the sample position, corresponding to an ion flux of the order of 10^{13} ions·cm^{-2}·s^{-1}. Based on the desired ion flux on the sample of about 0.1 ion·nm^{-2}·s^{-1}, an exposure time of the order of 0.1-1 s should be required to achieve a target density of 0.01-0.1 defect sites per nm^2. These very short exposure times can however not be set by electronically switching on and off the ion gun. As in the case of the ECR plasma, the switching of the ion gun requires a few seconds during which the gun parameters vary and therefore no stable operation conditions are present. We therefore also opted for a scheme where the sample has been moved in and out of the continuous ion beam, making use of the rotational motion of the sample holder. Analog to the case of the ECR plasma treatment, the optimal procedure for the irradiation has been calibrated by tests on a HOPG substrate at room temperature. Optimized parameters for both kinetic energies of the ions, 200 eV and 1.5 keV, are summarized in table 6.1. For both cases, the angle between the ion beam axis and the vector normal to the sample surface has been varied from 0° to about 160° and back to 0° after $T_{\text{exp}} = 2$ s.

6.2   Defect formation mechanisms

Changes in the structure of carbon nanotubes induced by energetic ions are dominated by knock-on atom displacements [29]. Computer simulations of ion irradiation of nanotubes showed that if the kinetic energy of the incident particle is higher than the carbon displacement energy T_{d}, which is always the case for the energy range we used [1], the head-on collision of an Ar ion with a carbon atom of the SWNT will result in the formation of vacancy-

---

[1]Using Eq. 4.1: $T_{\text{d}} = \frac{4m_{\text{c}}m_{\text{ion}}}{(m_{\text{c}}+m_{\text{ion}})^2}E_{\text{th}}$, with $T_{\text{d}} = 16$ eV, we find $E_{\text{th}} \approx 23$ eV

	I_d	V_d	V_p	p_prep	T_exp
Standard	5 mA	600 V	1.5 keV	$\sim 6{\cdot}10^{-6}$ mbar	-
200 eV	4 mA	400 V	0 keV	$6.1{\cdot}10^{-5}$ mbar	≈ 2 s
1.5 keV	1 mA	380 V	1.3 keV	$1.1{\cdot}10^{-5}$ mbar	≈ 2 s

Table 6.1: *Exposition parameters of the argon ion gun for standard surface clean-ing (Standard), defect generation on SWNTs with kinetic energy 200eV (200eV) and 1.5 keV (1.5 keV). The nomenclature used for the parameters is: discharge current (I_d), discharge voltage (V_d), discharge potential (V_p), pressure in the preparation chamber (P_{prep}), exposition time (T_{exp}). The irradiation processes have always been performed with the sample at room temperature.*
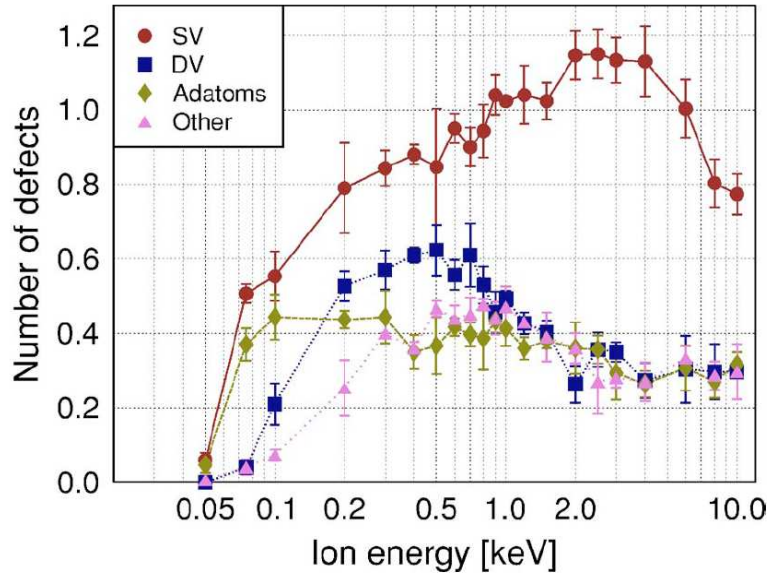
Figure 6.1: *Average number of single and double vacancies, C-adatoms, and other defects per Ar ion impact as a function of the Ar ions energy. The symbols are simulation results, lines are guides for the eye. Taken from [130]*

type defects such as single- or multi-vacancies, and a number of primary recoil atoms which leave the tube. The displaced carbon atoms can adsorb onto the tube walls and form a Frenkel pair with the created vacancy, or otherwise be sputtered from the tube [131]. Figure 6.1 a) shows results of molecular dynamics based calculations of the average numbers of single (SV)

and double vacancies (DV), adatoms, and more complex defects (including multi-vacancies) per Ar ion impact on a $(8,8)$ SWNT as function of the ion energy [130]. Similar plots are obtained for $(12,0)$ and $(10,4)$ SWNT, which have typical ($\sim$1.1 nm) diameters for SWNTs produced by HiPco process. From the diagram in Fig.6.1 a), it can be seen that SVs are created with the highest yield in the whole energy range from 50 eV to 10 keV. The maximal number of defects is found at an ion energy of about 0.7 keV. The ratio of SVs to DVs, N_{SV}/N_{DV}, has its minimum (1.5) at ion energies of about 0.5 keV, and with increasing ion energy, it saturates towards 3. The fraction of multi-vacancies is found to be less than 10% for all ion energies. Note that multi-vacancies normally appear when the ion tangentially hits the sides of the tubes. At room temperature, it was theoretically found that adatoms (on the outer surface of the SWNT) recombine very slowly with vacancies, *i.e.* several hours after irradiation [130]. Since our sample remains at room temperature for only five minutes before being cooled down to ~ 5 K, we expect a concentration of about 25% of adatom related defects on our samples.

6.3 Modifications of the local electronic structure of semiconducting SWNTs

6.3.1 *Ab initio* calculations

In contrast to the observations made for hydrogen plasma where the great majority of defect sites are composed of H-adatoms, SVs and combinations of them, the complexity of the defect configurations will be considerably increased for SWNTs exposed to medium energy ions with the expected SVs, DVs, multi-vacancies and carbon adatoms. To experimentally identify the observed defect types, or at least to classify different corresponding spectra, we calculated the electronic structures and the TDOS of individual defects species (SV, DV, triple vacancy (TV) and C-adatom) and simple combinations of them for a $(10,0)$ semiconducting SWNT. Calculations for vacancy-type defects are presented in Fig. 6.2. SVs have already been studied in section 4.4.1.1 (Figs. 4.5 and 4.6 b)). The upper panel in Fig. 6.2 a) shows a ball-and-stick model of the relaxed structure of a DV (red) superimposed on the honeycomb lattice structure of the ideal $(10,0)$ SWNT (green). Unlike SVs, which always have a remaining dangling bond excluding a perfect reconstruction, DVs reconstruct by saturating all the dangling bonds. This results in a DV formation energy E_{DV} smaller than the SV formation energy E_{SV}, as shown in [28]. The calculated band structure $E(k)$ for a DV, plotted in the lower panel of Fig. 6.2 a), shows a similar behavior as for a SV (Fig. 4.6 b)) with a rather flat new band in the mid-gap region,
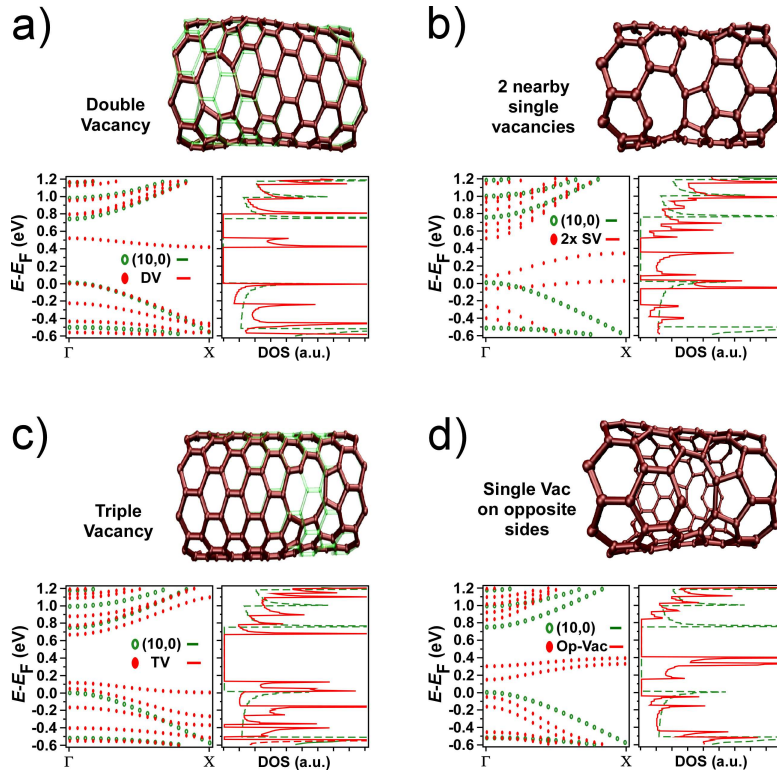
Figure 6.2: Ab initio *calculations of the electronic structure (band structure $E(k)$ and TDOS) of different vacancy related defect configurations in a semiconducting $(10,0)$ SWNT. a) Double vacancy (DV), b) two nearby single vacancies (SV), c) triple vacancy (TV), d) two single vacancies on opposite sides of the tube wall.*

showing a falling inflection point (rising inflection point for a SV on a $(10,0)$ tube) giving rise to narrow split peaks in the calculated TDOS. Note that the calculated width of the defect related band (non polarized DFT) for a DV is about 100 meV, which is nearly half of the value for a SV with about 180 meV.

Figure 6.2 c) presents *ab initio* calculations for a triple vacancy (TV) as an example of a multi-vacancy defect type. The band structure $E(k)$ shows the emergence of a flat band at the VBE. Although calculations for other tube species were not performed, a chirality dependence of the energy position of the new defect-induced states must be expected.

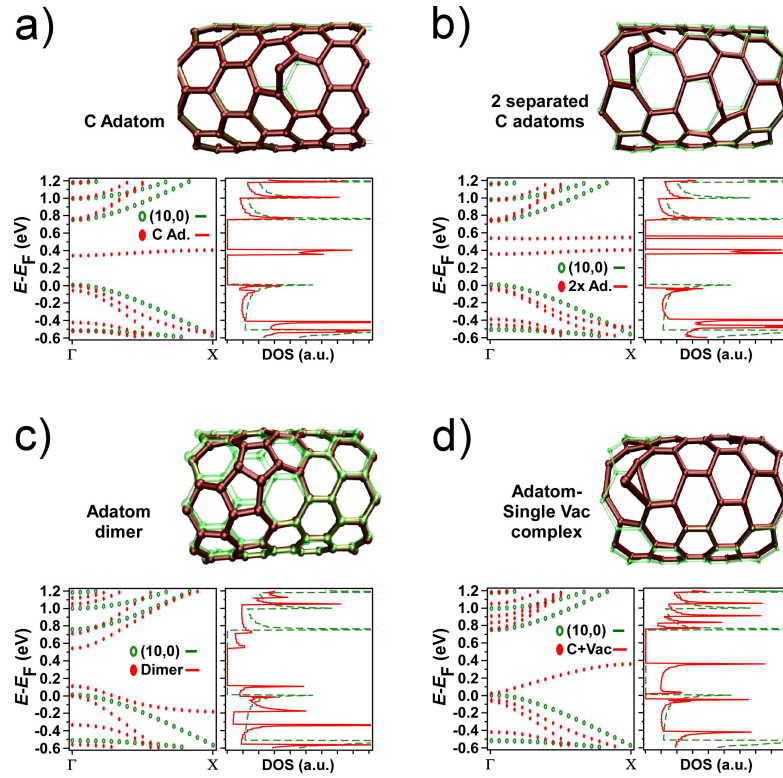Two examples for defect configurations of two separated vacancies (non-

Figure 6.3: Ab initio *calculations of the electronic structure (band structure $E(k)$ and TDOS) of different C-adatom related defect configurations in a semiconducting $(10,0)$ SWNT. a) Single C-adatom, b) two separated C-adatoms, c) C-adatoms dimer, d) adatom at the border of a single vacancy (Frenkel pair).*

adjacent removed atoms) are shown in Fig. 6.2, with two nearby SVs in the uppermost part of the SWNT in b), and two SVs on opposite sides of the SWNT in d). The SV on the lower side of the SWNT in d) can occur due to a collision with the recoil C atom or with the incident Ar ion itself. Note that the nanotubes can also be damaged by the incident ions being reflected back from the substrate or even by atoms sputtered from the substrate. In our case, this mechanism should only occur for 1.5 keV Ar ions [131]. Both configurations give rise to a pair of dispersive (with a rising inflection point) bands in the bandgap resulting in quite complex peak structures in the TDOS, as can be seen in the lower panels of Figs. 6.2 b) and d).

Defect configurations related to C-adatoms are shown in Fig. 6.3. The upper panel of Fig. 6.3 a) shows a ball-and-stick model of a single C-adatom. Previous *ab initio* calculations on different SWNT species have shown that the adsorption energy E_a is always lower for configurations with the C-adatom positioned above the middle of C-C bonds (bridgelike structure) oriented perpendicular to the SWNT axis than for a "parallel" configuration ($\Delta E \approx 1$ eV). The adsorption energy for both configurations is chirality dependent and its value increases with decreasing tube diameter. For our raw material with $d_{avg} \approx 1$ nm, typical values for E_a are around 3 eV, whereas E_a on the inner surface of the tube is lower with values of about 1.5 eV [31]. This has implications on the energy barriers for migration E_m. Indeed, E_m is found to be weakly dependent on the SWNT diameter and ranges between 0.5 eV and 0.7 eV. In contrast, adatoms inside the the SWNT are found to be mobile at room temperature with $E_m = 0.1$-0.3 eV [31], and all of them (about 45% of produced adatoms) quickly recombine with vacancies [130].

Similarly to H-adatoms, a single C-adatom gives rise to a low dispersive new state in the mid-gap region, as can be seen in the lower panel of Fig. 6.3 a). Note that the calculated width (non-polarized DFT) of a C-adatom-induced peak is about 0.06 eV, which is three times larger than the width found for a H-adatom (0.02 eV).

As an example of possible defect combinations with several C-adatoms, we calculated two configurations: two separated C-adatoms in Fig. 6.3 b) and a C-adatom dimer in c), which is found to be a stable configuration [31]. In the case of the two separated C-adatoms in Fig. 6.3, the defect structure gives rise to a pair of quasi dispersionless bands in the upper half part of the bandgap. This results in a double peak structure in the TDOS, with an energy separation of about 0.17 eV. The ball-and-stick model for the dimer in c) shows a defect structure which is similar to a Stone-Wales (SW) defect, with the difference that for the dimer the two pentagons have a common side, whereas the two heptagons share a common side in the SW configuration. It is interesting to see that the electronic structure of both configurations show similar degeneracy breaking features at the CBE and VBE, as can be seen in Figs. 4.11 d) and 6.3 c). Note that SW defects can appear in nanotubes after impacts of energetic ions, for example by the reconstruction of a single C-adatom with a single vacancy [129].

Finally, we calculated the electronic structure of a combination of a SV with a C-adatom (Frenkel pair) shown in the upper panel of Fig. 6.3 d). Here the main feature appearing in the band structure $E(k)$ is a highly dispersive band in the lower half part of the bandgap, with a rising inflection point resulting in a double peak structure with non-zero DOS between peaks.

6.3.2   Topography and spectroscopy measurements

6.3.2.1   200 eV Ar$^+$ bombardment

Figure 6.4 a) shows a STM topography image of a 50 nm long segment of a semiconducting SWNT ($(2,9)$ or $(2,10)$) exposed to 200 eV Ar ions. The average defect spacing is about 7 nm and the apparent height of the defect features is ranging from 0.5 Å to 4 Å, with a lateral extension varying typically between 5 Å and 30 Å. These values are similar to the ones observed for the H and N-plasma treated tubes. Figure 6.4 b) shows a detail image of the tube section inside the dashed ellipse drawn in a). A dI/dV-scan recorded along the horizontal dashed line is presented in the lower panel. Four defect sites labeled d1-d4 are clearly distinguishable and each of them gives rise to spatially localized single peaks in the mid-gap region or in the upper half part of the bandgap. Such signatures in the differential conductance are frequently observed in the case of a 200 eV Ar ion treatment, with FWHMs ranging from 60-200 meV. These FWHM values are larger than for H-plasma-induced single peaks where FWHMs ranging from 30-50 meV were observed. The general observation of broader peaks for the Ar ion bombardment is in accordance with the *ab initio* calculation, where it is shown that the electronic signatures of the most probable individual defect types, *i.e.* SVs, DVs and C-adatoms are single gap states with a FWHM of respectively 170, 100 and 60 meV. The widths for SVs and DVs are well above the values for single peaks induced by H decorated SVs (60-80 meV) and H-adatoms (20 meV) calculated for the same $(10,0)$ SWNT.

A second type of frequently observed features in dI/dV spectra is presented in Fig. 6.4 c). The current error image of another semiconducting SWNT ($(2,9)$ or $(2,10)$) with five defect sites labeled d5-d9 can be seen in the upper panel. In the lower panel, the dI/dV-scan recorded along the horizontal dashed line shows the emergence of double peak structures for defect sites d5, d7 and d8. These structure are very similar to the H dimers-induced symmetric paired states discussed earlier in Sect. 4.4.3. However, an explanation based on a possible H adsorption on the SWNT walls during the Ar ions bombardment can be practically ruled out. This statement is based on the H partial pressure in the low 10^{-10} mbar range, measured during the ion bombardment by means of mass spectrometry. We believe that such double peak structures are due to defect configurations composed of two close C-adatoms, as ab initio calculations for a $(10,0)$ SWNT show in Fig. 6.3 b). Here, the double peak structure is positioned in the upper half of the bandgap, similar as for the observed defect site d7 in Fig. 6.4 c). The origin of the double peak structure can be attributed as in the case of H to a tube mediated interaction between two low dispersive states.
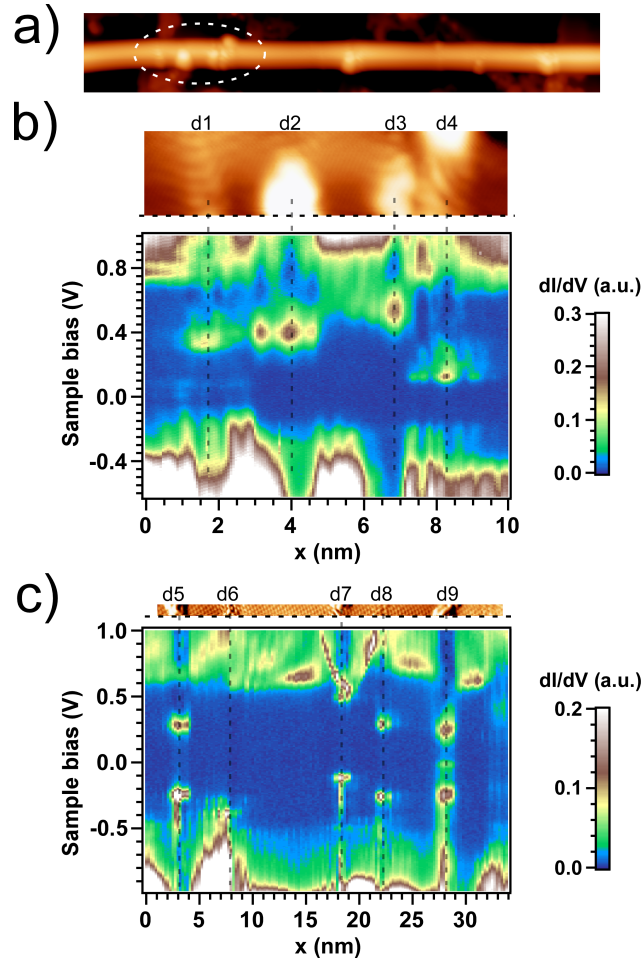
Figure 6.4: *a) STM topography image of a 50 nm long segment of a semiconducting SWNT exposed to 200 eV Ar ions. $U_s = 1$ V, $I_s = 0.25$ nA, $\Delta Z = 1.24$ nm. Possible chiral indices: $(2, 9)$ or $(2, 10)$. b) Detail image of the tube section with defect sites d1-d4 inside the dashed ellipse drawn in a) and dI/dV-scan recorded along the horizontal dashed line. $U_s = 1$ V, $I_s = 0.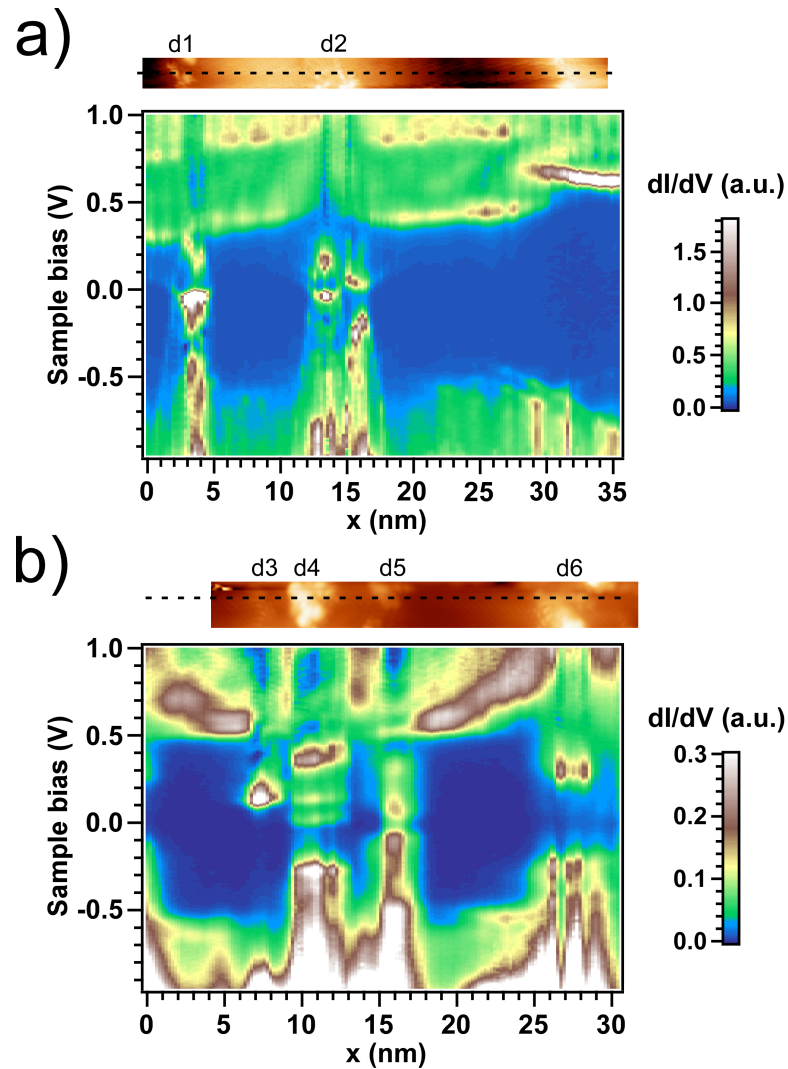25$ nA, $T = 5.3$ K, $U_{mod} = 15$ mV, $x_{res} = 0.67$ nm. c) Upper panel: Current error image of another semiconducting SWNT ($(2, 9)$ or $(2, 10)$) with five defect sites d1-d5. Lower panel: dI/dV-scan recorded along the horizontal dashed line. $U_s = 1$ V, $I_s = 0.1$ nA, $T = 5.22$ K, $U_{mod} = 15$ mV, $x_{res} = 0.22$ nm.*

Figure 6.5: *STM topography images (line by line flattened) of two semiconducting SWNTs treated with 1.5 keV Ar ions and corresponding dI/dV-scans (lower panels) recorded along the horizontal black dashed lines. Possible chiral indices in a): $(4,8)$, $(5,9)$ or $(5,10)$ for b): not found. Measurement parameters in a): $U_s = 1$ V, $I_s = 0.15$ nA, $T = 5.24$ K, $U_{mod} = 15$ mV, $x_{res} = 0.24$ nm, b):$U_s = 1$ V, $I_s = 0.1$ nA, $T = 5.2$ K, $U_{mod} = 15$ mV, $x_{res} = 0.3$ nm.*

6.3.2.2   1.5 keV Ar$^+$ bombardment

Figures. 6.5 a) and b) show dI/dV-scans recorded along two different semi-conducting SWNTs irradiated with 1.5 keV Ar ions. Two (d1-d2) and four (d3-d6) defect sites can be seen in a) and b), respectively. Besides d3 which gives rise to a single peak in the mid-gap region and d6 with a double peak structure, all the other defect sites presented in Fig. 6.5 show complex multi-peak configurations with non-zero intensity almost in the entire gap region. These features resemble to the electronic signature of more complex structures like two nearby SVs, two SVs on opposite sides or the C-adatom-SV complex shown in Figs. 6.2 b), d) and Fig. 6.3 d), respectively. We consider a defect structure as complex if more than two peaks are observed in the corresponding spectra or if the intensity is non-zero in the most part of the gap. Of 34 defect sites investigated for the 200 eV bombardment, we found 8 complex defect structures, and of 60 defect sites investigated for 1.5 keV bombardment, we found 27 complex defect structures. We thus found an increase of about 95% of the complex defect structures (from 23% to 45% of the total structures) going from the 200 eV to the 1.5 keV treatment. Our observation shows a qualitatively similar behavior with the calculations shown in Fig. 6.1. An abundance of complex defect structures of about 18% for 1.5 keV Ar ions and about 12% for 200 eV is predicted.

To conclude, we can state that the most commonly observed modifications of the electronic structure for SWNTs treated by short exposition to 200 eV and 1.5 keV kinetic energy Ar ions are the appearance of single and double peak structures positioned at different positions in the bandgap. These gap states correspond to individual or simple combinations of vacancy or C-adatom related defect structures. More complex multi-peak features have been observed with about 95% higher frequency in 1.5 keV irradiated samples as in 200 eV.

6.4   Metallic SWNTs

The upper panel of Fig. 6.6 shows a STM topography image of a metallic SWNT irradiated with 200 eV Ar ions. Seven defect sites d1-d7 distributed along a ∼30 nm long tube section can be identified. The dI/dV-scan recorded along the horizontal dashed line is displayed in the lower panel. One can observe that local modifications of the density of states are manifested by the presence of new states spatially localized on the defect sites. For each defect site, 1 to 4 peaks positioned near the Fermi level can be observed (1 for d1, 4 for d7). Because of the same limitations of prohibitively high computational costs mentioned earlier, we do not dispose of any *ab initio* calculations for metallic tubes. However, the presence of peaks
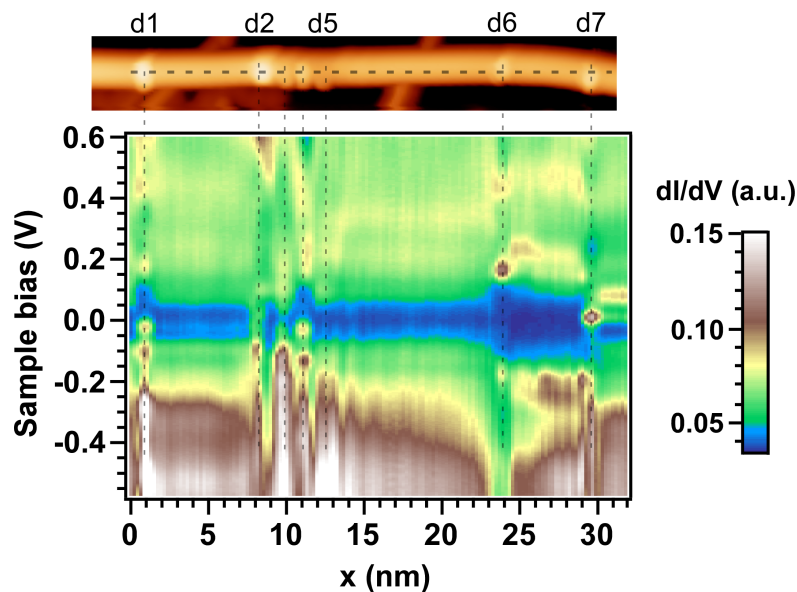
Figure 6.6: *Upper panel: STM topography image of a metallic SWNT irradiated with 200 eV Ar ions. $\Delta Z = 1$ nm. $U_s = 0.6$ V, $I_s = 0.3$ nA. Lower panel: dI/dV-scan recorded along the horizontal dashed line. $U_s = 0.6$ V, $I_s = 0.3$ nA, $T = 5.35$ K, $U_{mod} = 15$ mV, $x_{res} = 0.22$ nm*

around the Fermi level for a metallic SWNT is consistent with earlier TB based calculations showing a spatially localized SV-induced intense peak at the Fermi level [40]. It is important to notice that there are modifications in the LDOS between the defects. In the positive bias range, rather broad states of constant energy can be observed. These are very apparent between d6 and d7 with an energy difference of 230 meV. Less intense but still discernible, they can also be seen between d1-d2 and d5-d6, where the energy difference seems to scale inversely with the separation of the bounding defects. This observation constitutes a first indication of quantum confined states [132] and also shows that the Ar ion-induced defects create sufficiently strong electron scatterers to lead to quantum confinement. The in-depth characterization of defect-induced quantized states will be given in chapter 9.

Chapter 7

Negative Differential Resistance

Negative differential resistance (NDR) is the the effect at the basis of important electronic devices like Esaki diodes [133] or resonant tunneling diodes used in ultra-high frequency applications [133–136]. Previous STS experiments reported the observation of a NDR behavior in molecular systems or semiconductor nanocrystals deposited on metallic or semiconducting substrates, caused by different mechanisms [137–147]. Phonon-mediated NDR has also been observed in STM/STS investigations of suspended SWNTs structures [148, 149]. In this chapter, we are going to characterize and discuss the NDR behavior we regularly observed in the *I-V* curves recorded on SWNT defect sites. This effect, which is related to the presence of narrow gap states in the SWNT LDOS, has been observed independently of the ion treatment we used to create the defects.

7.1   Experimental observations

Figure 7.1 shows both an *I-V* curve and the corresponding dI/dV spectrum recorded at $T = 5.56$ K with setpoint parameters $V_s = 1$ V and $I_s = 0.6$ nA, on a H-plasma induced defect identified as a H dimer. This defect corresponds to the defect site located on the right hand side of the SWNT displayed in Fig. 4.12 b), giving rise to paired peaks D1 and D2. The *I-V* curve exhibits a NDR behavior in the positive $V > V_{D1}$ bias range highlighted by the green shaded zone. Since in this case the lock-in amplifier delivers the absolute value of the differential conductance $|dI/dV|$, the negative value of the derivative dI/dV in the NDR range is displayed with a reversed positive sign in the $|dI/dV|$ spectrum. Such NDR behavior has been observed only in the positive bias range for the vast majority of the
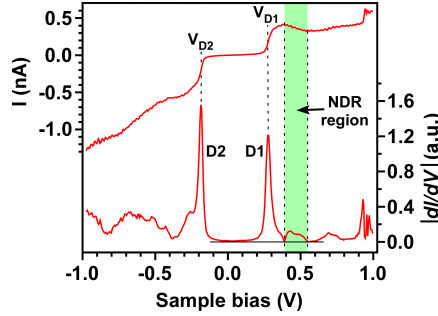
Figure 7.1: *I-V curve and dI/dV spectrum recorded at $T = 5.56$ K with setpoint parameters $V_s = 1$ V and $I_s = 0.6$ nA, on a H-plasma induced defect identified as a H dimer. The NDR behavior is highlighted by a green shaded region.*

investigated defect-induced gap states, which energetic positions are evenly distributed in the positive or the negative bias range. For gap states positioned in the negative bias range like D2, a NDR behavior showed up in some extremely rare cases. We think that this can be due to a resonant energy matching between transient discrete levels in the Pt/Ir tip and narrow peaks in the LDOS at the defect position [137–139, 144].

7.2   Bias-dependent barrier height model

The system formed by the tip, SWNT with defect and the substrate can be regarded as a double barrier tunneling junction with tip-tube and tube-substrate tunneling ratios Γ_1 and Γ_2, respectively. With the typical setpoint parameters we used to characterize defect-induced changes in the LDOS of SWNTs, we confidently assume that $\Gamma_1 << \Gamma_2$, which corresponds to the so-called shell-tunneling spectroscopy regime where the electrons tunnel through the defect/tube states one-by-one [146].

Typically observed NDR behavior can be understood readily within a simple tunneling model. For $T = 0$ K and assuming a constant DOS for the tip in the referred energy window, the current resulting from electrons tunneling from the tip into SWNT defect states with spatial coordinates (x, y) can be written:

$$I(x, y, V) \propto \int_{E_{\mathrm{F}}=0}^{eV} \rho_{\mathrm{d}}(E, x, y) \cdot T(E, eV, z) dE \qquad (7.1)$$

where $\rho_{\mathrm{d}}(E, x, y)$ is the LDOS of the SWNT at the defect position. As shown in chapter 2.1.2, the bias voltage-dependent transmission coefficient $T(E, eV, z)$ can be estimated within the WKB approximation to be:

$$T(E, eV, z) = e^{-\kappa z \sqrt{(\phi_{\mathrm{d}} + \phi_{\mathrm{t}})/2 - E + eV/2}} \qquad (7.2)$$

where κ is the decay constant equal to $\kappa = 2(2m_e/\hbar^2)^{1/2} = 1.02\ \text{Å}^{-1}\text{eV}^{-1/2}$. ϕ_d and ϕ_t are the work functions for the SWNT and the tip, respectively. For a numerical investigation of the NDR behavior, the hypothetical LDOS of the sample $\rho_d(E, x, y)$ is shown in Fig 7.2 a). We chose a typical density of states for a semiconducting SWNT with four van Hove singularities represented (of the form $1/\sqrt{|E - E_0|}$). The bandgap defined by the position of the first VHS is 1.2 eV. The defect-induced states are simulated with two Lorentzians, P1 and P2, of equal amplitude and a FWHM of 8 meV. P1-P2 are symmetrically positioned with respect to the mid-gap level with an energy separation of 0.4 eV. The amplitude in the bandgap is set to zero at the boundaries defined by the position of the first VHS. The corresponding
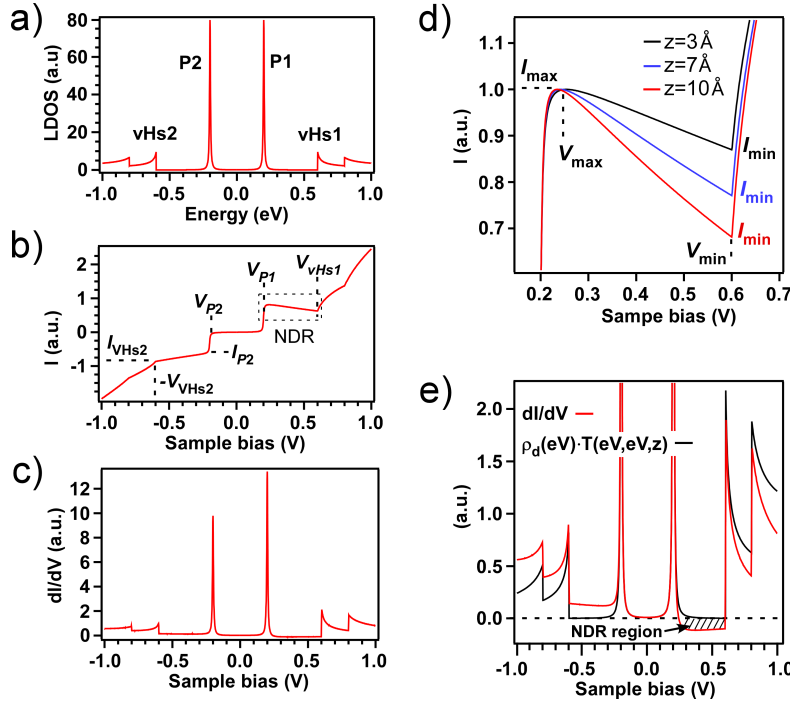

Figure 7.2: *a) Simulated LDOS ($\rho_d(x, y, eV)$) of a typical semiconducting SWNT with a double Lorentzian peak structure P1-P2. b) Corresponding STM current computed numerically from Eq. 7.1 with $z = 7$ Å. c) Derivative $dI/dV(V)$ of the STM current in b) computed numerically. d) Detail of the NDR region in b) computed for three different values of z. e) Detail of the $dI/dV(V)$ curve in c) with $\rho_d(x, y, eV) \cdot T(eV, eV, z)$ corresponding to the first term of Eq. 7.5.*
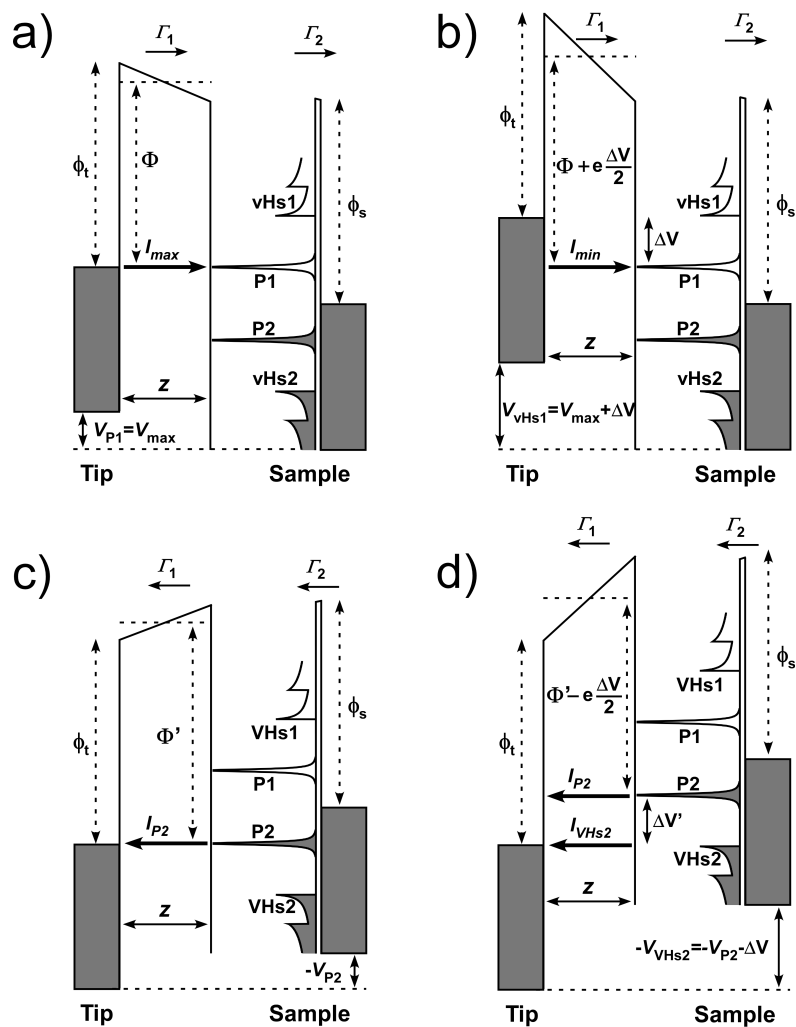
Figure 7.3: *Schematic of the tip-tube-substrate tunnel junction for positive a)-b) and negative c)-d) bias voltage. P1 and P2 represent the symmetric double Lorentzian peak structure in Fig. 7.2 a). The real proportion in amplitude and width are changed for clarity. The tip DOS is assumed to be constant and the tip-sample separation is equal to z. Here the work functions of the tip ϕ_t and sample ϕ_t are chosen to be equal for the sake of simplicity.*

STM current $I(x, y, V)$ computed from Eq. 7.1 with $z = 7$ Å and $\phi_d = 4.7$ eV, $\phi_t = 5$ eV is plotted in Fig 7.2 b). A NDR behavior is clearly visi-

ble between V_{P1} and V_{VHS1}, whereas the current is continuously increasing in the negative bias range. To understand the nature of the NDR and the asymmetry in positive and negative bias range, let us consider the tunneling junction model in Fig. 7.3 for different values of the bias voltage, a) to d). We first consider the situation for positive bias voltages $V > 0$ illustrated in panels a) and b). Resonant tunneling occurs when the Fermi level of the tip is aligned with P1, *i.e.* for $V = V_{P1}$. This situation is depicted in Fig. 7.3 a) and the STM *I-V* curve will show a step at this point. For this value of the bias voltage, the mean tunneling barrier height for electrons tunneling from the tip into P1 is given by $\Phi = \bar{\phi} - eV_{P1}/2$ with $\bar{\phi} = (\phi_d + \phi_t)/2$. When the bias is further increased, there are no new states contributing to the tunneling current until $V_{VHS1} = V_{P1} + \Delta V$ is reached. However, the mean barrier height for electrons tunneling into P1 will increase with increasing bias voltage. At V_{VHS1}, it will reach a value of $\Phi + \frac{e\Delta V}{2}$. This results in a reduced transmission coefficient T and hence, a decreasing current with increasing V in the range $V_{P1} < V < V_{VHS1}$, *i.e.* NDR. Under the assumption that P1 is very sharp ($FWHM(P1) << \Delta V$), it can be shown from Eqs. 7.1 and 7.2 that for $V_{P1} < V < V_{VHS1}$, the ratio $I(V)/I(V_{P1})$ can be written as:

$$I(V)/I(V_{P1}) = e^{-\kappa z \left(\sqrt{\bar{\phi} - eV_{P1} + eV/2} - \sqrt{\bar{\phi} - eV_{P1}/2} \right)} \tag{7.3}$$

This ratio is always smaller than 1 for $V_{P1} < V < V_{VHS1}$ thus NDR is always observed in this bias range due to the bias dependent barrier height. If we assume an ideal discrete state P1, whose spectrum is described by a Dirac peak $\delta(E - eV_{P1})$, the current reaches a maximum value I_{max} at the bias voltage $V_{max} = V_{P1}$. In reality, the width of the states induces a positive shift in V_{max}. In our example, the value of V_{max} is shifted by about 42 meV for P1 centered at $E = 0.2$ eV and $z = 7$ Å (35 meV and 54 meV for $z = 10$ Å and 3 Å, respectively). Tunneling through sufficiently large DOS around narrow states overpowers the current drop and thus impedes the NDR to emerge. This is why no NDR is observed for $V > V_{VHS1}$ where a non-zero DOS occurs between the VHS. From Eq. 7.2, it also follows that the current drop in the NDR region can be tuned by varying the tip-tube distance z, resulting in a more pronounced current drop for increasing z. This is illustrated in Fig. 7.2 d) where the STM current in the NDR region is plotted for three different values of z. The current curves are normalized to $I_{max} = 1$.

The situation for $V < 0$ is illustrated in panels c) and d) of Fig. 7.2. In contrast to the case of increasing positive bias $V > 0$, the height of the tunneling barrier Φ' for any isolated state like P2 is continuously decreasing with an increase of $|V|$. This results in an increasing tunneling current

from P2 into the unoccupied states of the tip for bias voltage in the range $V < V_{P2}$. Formally, we can write the ratio $I(V)/I(V_{P2})$ from Eq. 7.2 again assuming that P2 is very sharp $P1(E) = \delta(E - eV_{P2})$:

$$I(V)/I(V_{P2}) = e^{-\kappa z \left(\sqrt{\bar{\phi} + eV_{P2} - eV/2} - \sqrt{\bar{\phi} + eV_{P2}/2} \right)} \tag{7.4}$$

This ratio is always larger than 1 for $V < V_{P2}$ thus preventing any NDR behavior to emerge in the negative bias range.

This asymmetry in the behavior of the STM current for positive and negative bias range due to a bias-dependent barrier height has consequences on the measured differential conductance. Figures 7.2 c) and e) show the $(dI/dV)(V)$ spectrum computed numerically from the $I(V)$ curve in b). Formally, the differential conductance can be obtained by differentiating Eq. 7.1:

$$\frac{dI}{dV}(x, y, V) \propto e \cdot \rho_d(x, y, E = eV) \cdot T(E = eV, eV, z)$$
$$+ \int_0^{eV} \rho_d(x, y, E = eV) \cdot \frac{dT(E, eV, z)}{dV} dE \tag{7.5}$$

Three different effects can be seen in the $(dI/dV)(V)$ spectrum:

(i) Figure 7.2 c) shows that the unoccupied states in the positive bias range of the spectrum have a higher intensity than the occupied states in the negative bias range. This is due to the weighting of the original LDOS, $\rho_d(x, y, E)$, by the exponential profile of the transmission coefficient in the first term of Eq. 7.5. This effect must be taken into account in the comparison of the amplitude of different peaks. Figure 7.2 e) shows a superposition of the $dI/dV(V)$ spectrum and the first term of Eq. 7.5. The difference of both curves is equal to the second term of Eq. 7.5.

(ii) The NDR behavior results in a region with negative sign in $dI/dV(V)$. Note that formally the information on the NDR behavior is completely defined by the second term of Eq. 7.5.

(iii) The decreasing height of the tunneling barrier in the range $\Delta V'$ for $V < 0$ (Fig. 7.3 d)) results in a non-zero LDOS in the $dI/dV(V)$ spectrum. This effect must be taken into account for the analysis of the density of states around narrow peaks located in the negative bias range.

Figure 7.4 shows an experimental example for the z-dependence of the NDR. Here we recorded two spectra at 0.1 nA and 1 nA with a setpoint
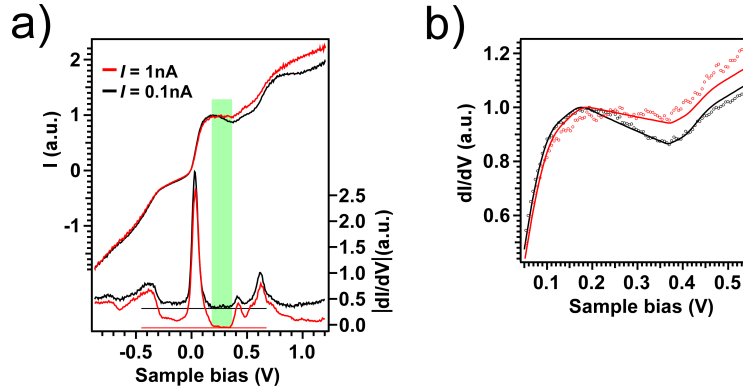
Figure 7.4: *Experimental example for the tunability of the NDR behavior. a) I-V and corresponding dI/dV spectra recorded on a N-plasma-induced defect site. Both I-V were obtained by averaging of three individual spectra. b) Detail of the NDR region with fits computed from Eq. 7.1 with $z = 3$ Å for $I_s = 1$ nA and $z = 7$ Å for $I_s = 0.1$ nA. $T = 5.25$ K*

voltage $V_s = 1.2$ V at the same position on a defect site induced by N-plasma treatment. The $I(V)$ curves for both setpoint currents and the corresponding dI/dV spectra are displayed in Fig. 7.4 a). Note that for each spectrum the recording time is about 30 s, resulting inescapably in a small spatial variation of the position where spectra are recorded. This explains the slight amplitude differences in both dI/dV spectra. However, the tuning of the NDR by varying the setpoint current is clearly visible in the zone highlighted by the green shaded region. To simulate the NDR behavior, we calculated the current from Eq. 7.1 with the LDOS being the measured spectrum for $I_s = 1$ nA, divided by the transmission coefficient $T(E = eV, eV, z)$. The peak locations shift slightly with the setpoint current (tip height) due to band bending [143]. This shift of about 5 meV is taken into account in the simulation. As shown in Fig. 7.4 b), the NDR magnitude can be quite well reproduced with $z = 7$ Å for $I_s = 0.1$ nA and $z = 3$ Å for $I_s = 1$ nA. With a first approximation relation for z derived from Eq. 7.5 considering only the first term, and taking into account a contact resistance for $z = 0$ of 100 kΩ [143], we find values for z being 4.5 Å and 5.6 Å for $I_s = 1$ nA and 0.1 nA, respectively. Even though our approximation of the genuine $\rho_d(x, y, E)$ is crude, our simple model fits the experimental data very well.

Chapter 8

Stability of defect structures

The reliability of potential future devices based on the local modification of SWNTs by a controlled creation of specific defects will highly depend on their structural stability. In the following paragraphs, we will describe and comment observed changes at defect sites which can occur under normal or extreme STM measurement conditions. These changes are classified into two categories: complete disappearance of defect sites and modification of the topographic and electronic structure at the defect site.

Figures 8.1 and 8.2 illustrate two situations where the complete disappearance of a defect site occurs during the scanning of the tip. A semiconducting $(6, 13)$ SWNT with one ECR H-plasma induced defect site is shown in the upper panel of Fig. 8.1 a). The image was recorded at $T = 5.65$ K
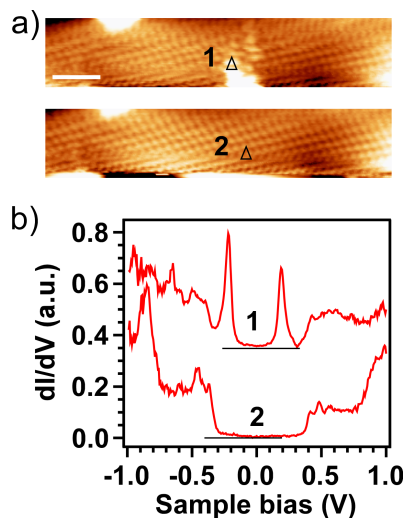

Figure 8.1: *a) Upper panel: Topography STM images (line by line flattened) of a semiconducting $(6, 13)$ SWNT with one ECR H-plasma induced defect site. Lower panel: Same SWNT after disappearance of the defect. Scale bar is 1 nm. b) Individual spectra recorded on the SWNT in a) at the locations indicated by black triangles, before and after the disappearance of the defect site. Spectrum 1 is offset for clarity. $V_s = 1$ V, $I_s = 0.3$ nA, $T = 5.65$ K.*
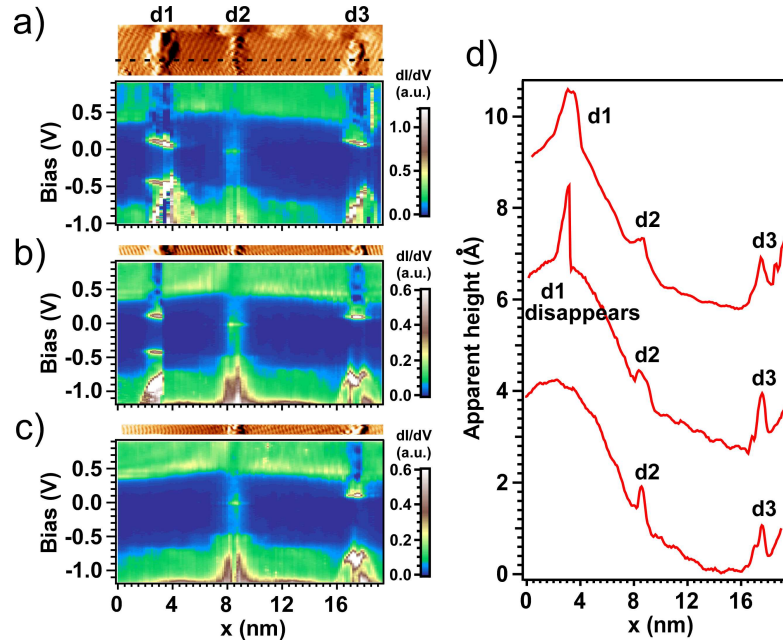
Figure 8.2: *a),b),c) Time sequence of dI/dV-scans recorded along the axis of a semiconducting SWNT (black dashed line) exposed to 1.5 keV Ar^+ ions. d) Time sequence of apparent height profiles recorded along the same lines as for the dI/dV-scans in a)-c), offset for clarity. STM parameters for a): $V_s = 1$ V, $I_s = 0.12$ nA, $V_{mod} = 16$ mV, $x_{res} = 0.25$ nm, $T = 5.26$ K, for b) and c): $V_s = 0.9$ V, $I_s = 0.12$ nA, $V_{mod} = 16$ mV, $x_{res} = 0.15$ nm, $T = 5.26$ K.*

with setpoint parameters $V_s = 1$ V and $I_s = 0.3$ nA. A single spectrum measured at the position 1 is plotted in Fig. 8.1 b) (offset for clarity). This spectrum corresponds to the signature of an adsorbed hydrogen dimer, with typical paired gap states. A second topography image recorded a few minutes later shows a perfect atomic lattice at and around the position of the defect site in the upper panel, and the spectroscopy at position 2 shows a typical spectrum for a defect free semiconducting SWNT.

Figure 8.2 shows a chronological sequence of three dI/dV-scans recorded on a semiconducting SWNT with three defect sites labeled d1-d3 induced by an exposition to 1.5 keV Ar^+ ions. The three dI/dV-scans have been recorded at a temperature of 5.26 K and the setpoint parameters are $V_s = 1$ V, $I_s = 0.12$ nA in a) and $V_s = 0.9$ V, $I_s = 0.12$ nA in b) and c). The corresponding apparent height profiles recorded along the same lines as for the the dI/dV-scans are plotted in panel d). In panel a), each defect site

d1)-d3) gives rises to different electronic signatures: symmetric paired gap states for d1, non-zero intensity across the entire gap with a single peak at the mid-gap level for d2 and a structure with non-symmetric paired peaks for d3. In panel b), one can observe that the defect structure d1 is disappearing during the recording of the dI/dV-scan, where about only the first half of the spatial extent of the paired gap states is visible, followed by a sharp transition to the unperturbed electronic structure. This sharp transition is also clearly visible in the corresponding apparent height profile in d). The third dI/dV-scan in c) and the corresponding apparent height profile in
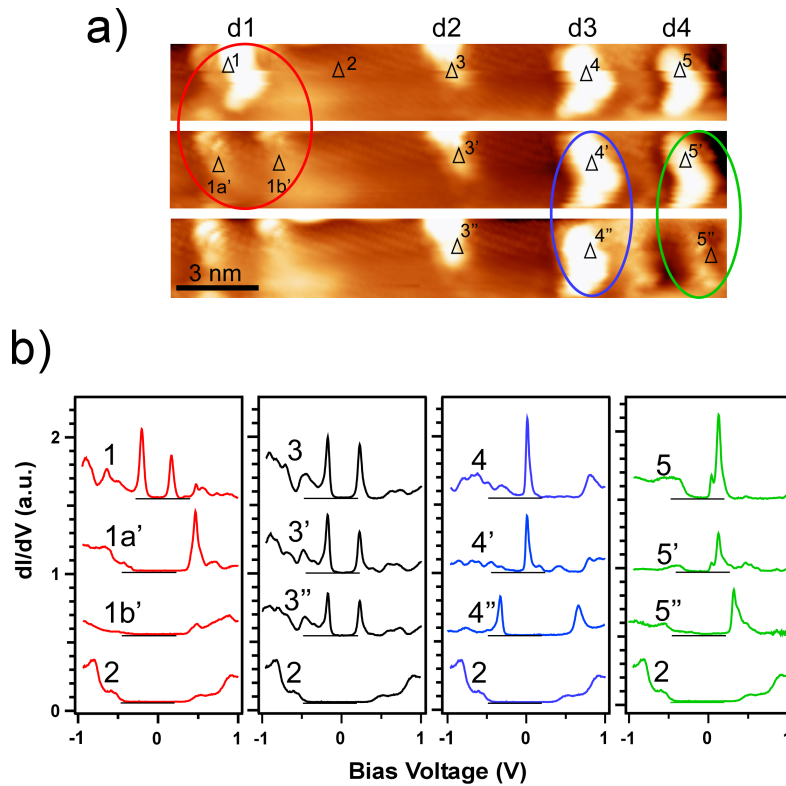

Figure 8.3: *a) Consecutive topography STM images (line by line flattened) of a semiconducting* $(7,5)$ *SWNT exposed to 200 eV* Ar^+ *ions with changes in the defect structure after scanning at higher setpoint current (1) or spectroscopy with increasing setpoint currents on individual defect sites (4 and 5). b) Individual spectra recorded on the SWNT in a) at locations indicated by black triangles.* $V_s = 1$ *V,* $I_s = 0.3$ *nA,* $T = 5.35$ *K.*

d), both recorded immediately after the second dI/dV-scan in b), confirm the complete disappearance of the defect structure, leaving the underlying lattice unperturbed. According to the discussions on defect structures induced by medium energy Ar^+ ions in chapter 6, we can assign d1 to a structure composed of at least two close C-adatoms. In this case, since no clear transition in the dI/dV features in the CB and VB besides the electronic signature of d1 is visible, we can think that the C-adatoms do not adsorb on the tip apex but desorb or diffuse along the wall of the SWNT out of the scanning window, or even adsorb on the substrate. The same assumptions can be made for the H dimer in Fig. 8.1.

Figure 8.3 gives an illustration for the case where defect sites experience a modification in their structure. Here, three consecutive STM images (from top to bottom) of a semiconducting $(7, 5)$ SWNT exposed to 200 eV Ar^+ ions are displayed. These images have been recorded at T = 5.35 K with setpoint parameters $V_s = 1$ V and $I_s = 0.3$ nA. In the top image of panel a), four defect sites labeled d1-d4 are visible and single point spectra have been recorded on each of them at positions 1,3,4 and 5. These spectra are displayed in panel b), showing paired gap states for 1 (red) and 3 (black), and single gap states for 4 (blue) and 5 (green). According to discussions in chapter 6, the double peak structures are associated to two (or more) close but separated C-adatoms and single peaks can be due to single C-adatoms, SVs or DVs. A comparison between the top and middle STM images in panel a) clearly shows a modification in the structure of defect d1 which splits into two defect sites indicated by positions 1a' and 1b'. Spectroscopic signatures in panel b) show a single intense peak at the CBE for 1a' and also a single peak at the same energy position but less intense for 1b'. This modification in the structure of d1 occurred between the recording of the top and middle images. All other defect structures remain unchanged.

In the framework of a z-dependence measurement of the NDR behavior on defect d3, a series of spectra have been recorded at different setpoint currents for the same bias voltage of 1 V. We could observe that this defect structure remained stable up to a current of about 300 nA and changed its structure at the maximal available current of about 330 nA, with a transition in the electronic structure from a single mid-gap peak to paired peaks with one in the CB and the second in the VB (spectra 4' and 4" in panel b)). Besides this change, it can be observed that the structure of the nearby defect site d4 has also undergone a modification during the same measurement at 330 nA, with a shift of the initial mid-gap peak toward the CBE (spectra 5' and 5" in panel b)).

To summarize, we could make the following observations:

(i) Some defect structures disappeared from the imaged tube surface af-

ter a certain time (few seconds up to tens of minutes) under scanning with standard setpoint parameters of $V_s = 1$ V, $I_s = 0.1 - 1$ nA, which correspond to a dissipated power of 0.1 - 1 nW, independently on the type of treatment (H-plasma or Ar^+ bombardment). These defect structures show an electronic signature corresponding to adatom configurations.

(ii) In some rare cases, the defect sites were seen to change their configuration under scanning with standard setpoint parameters, like *e.g.* in the transition from a double peak structure on a single defect site (1) to two defect sites each showing a single peak at the CBE (1a').

(iii) Some defect sites showing one (or two) gap state disappear or change their structure by recording single spectra with standard setpoint parameters. Here the residence time of the tip at the position of the defect site is longer than for scanning.

(iv) A defect site showing a single gap state close to the mid-gap level remained stable with setpoint parameters $V_s = 1$ V, $I_s \simeq 300$ nA and changed its structure with a setpoint current of 330 nA. This event has been accompanied by a change in the structure of a close defect site (about 3 nm) showing a shift of mid-gap peak towards the CBE.

This classification reflects a hierarchy in the stability of the observed defect structures. (i)-(iii) refer to configurations which are observed to be the less stable. The disappearing of adatom-related defect sites during the scan with standard conditions (i) is most probably due to tip-adatom interactions whose nature is similar as in the case of controlled manipulation of weakly adsorbed molecules on metallic surfaces [150]. However, in our case the topography signal never showed any typical signature for an adsorption of the adatoms on the tip, indicating a possible desorption of the adatoms or a tip-induced diffusion out of the scanning range [151].

Generally, the change in configuration referred in (ii) can also be understood from the arguments in (i). However, the example of transition given in (ii) for a semiconducting SWNT exposed to 200 eV Ar^+ ions is difficult to explain within the assumption of an initial defect structure composed of two C-adatoms as usually attributed for a double peak structure in this system. Indeed, an hypothetical diffusion or desorption of only one C-adatom should result in a peak in the mid-gap region and not at the CBE (see Fig.6.3). Note however that we only performed *ab initio* calculations for the most favorable configuration of a C adatom positioned above the middle of C-C bonds oriented perpendicular to the SWNT axis, and only for one chirality. Furthermore, *ab initio* calculations report that C-adatoms have roughly the

same mobility as single vacancies [28]. Thus, the possibility that the initial structure might be composed of a vacancy-type configuration cannot be ruled out since a double peak structure could arise from two non adjacent SVs.

The defect site showing a high stability described in (iv) is thought to be a double vacancy. This assumption is based on the measured electronic structure showing an intense and narrow mid-gap state, which is in good agreement with *ab initio* calculations for a double vacancy in a $(10, 0)$ SWNT. Furthermore, a value for the migration barrier of a double vacancy of more than 5 eV has been recently reported. For comparison, the migration barrier of a SV has been calculated to be about 1 eV [28] and 0.5 - 0.7 eV for a C-adatom on the outer shell of a SWNT [31]. Thus, stable double vacancies can be obtained from the coalescence of single vacancies through heating (SVs are already mobile at 100-200°C [31]).

Chapter 9

Quantum confinement

9.1   Introduction

When the wavelength of particles like electrons or holes become comparable to the dimensions of a given system, the behavior will then be dominated by the rules of quantum mechanics. The latter teaches us that such finite-size effects lead to a quantization of the wave vector in the confined direction. The system can be referred to as a quantum dot (QD) when the particles are confined in all spatial directions. The system is thus reduced to a zero-dimensional problem where the energy eigenvalues are discretized. The experimental realization of QDs [152, 153], which are sometimes called "artificial atoms", led to new concepts allowing researchers to define QD-based advanced devices in fields like nanoelectronics and nanophotonics. Moreover, QDs are thought to be possible candidates for the implementation of spin- or charge-based qubits for future quantum computation applications [154, 155].

Carbon nanotubes have shown to provide a well-suited platform for studying QD physics [156]. SWNT-based QDs can be defined by the creation of two spatially separated tunneling barriers, which electronically decouple a section of the tube and lead to quantum confinement. Such tunneling barriers have been experimentally realized by high resistive contacts [157], gate electrodes [158], or by local bending [3]. However, from a technological point of view it would be highly desirable to decouple short sections of a SWNT by artificially created defects in way to define intratube QDs. The advantage here is that the technologically extremely difficult task of contacting a nanometer-sized functional unit could be intrinsically solved by using the unperturbed tube ends as larger and less sensitive contact pads. That this is in principle realizable was demonstrated by the observation of confined electronic states in a metallic SWNT due to backscattering on a defect of unknown nature near the end of the tube [159].

In this chapter, we discuss the observation of confined states between ion-induced defects in metallic and semiconducting SWNTs by means of LT-STM/STS investigations.

9.2 Confined states in ion-irradiated metallic SWNTs

Figure 9.1 a) shows a ~ 50 nm long portion of an armchair SWNT which has been exposed to a low dose of 200 eV Ar ions. The current error image of the tube section delimited by the dashed rectangle in a) is displayed in panel b) with the corresponding dI/dV-scan recorded along the horizontal dashed line running over seven defect sites labeled d1-d7. Note that d5 does not show a very pronounced feature in the topography, but exhibits a clear electronic signature. This defect most probably lies on the substrate side of the tube and might be of intrinsic nature. Several broad discrete states characterized by a modulation of the differential conductance in the spatial direction can be distinguished in the negative bias range between d3-d4 and d5-d6, and in the positive bias range between d2-d3. A better contrast can be obtained by subtracting a second or third order polynomial fit from each dI/dV spectrum. The result of this operation for a third order fit is shown in Fig. 9.1 c). From this image, it appears clearly that the discrete states between d3-d4 and d5-d6 in the negative bias range each show a discrete number of equidistant anti-nodes. Moreover, especially between d3-d4, the number of maxima in each discrete state shows a regular sequence i, $i+1$, $i+2$... for an increasing absolute value of the bias, similarly as for the 1D particle-in-a-box model. This simple model allowed a quite accurate estimation of the level spacing around the charge neutrality point (CNP) for discrete states observed in very short SWNTs (cut) deposited on gold [132, 160], as well as in SWNT-based QD devices [158]. It is based on the linear dispersion $E = \hbar v_\mathrm{F} k$ around $\mathbf{K}$ ($\mathbf{K}'$) for a SWNT with finite length L, resulting in discrete k-values parallel to the tube axis, $k = m\pi/L$ with m being an integer number. With $v_\mathrm{F} = 8.5 \cdot 10^5$ m·s^{-1} [160], the energy spacing is thus given by:

$$\Delta E = \frac{h v_\mathrm{F}}{2L} \simeq \frac{1.76}{L} \, \mathrm{eV} \cdot \mathrm{nm} \tag{9.1}$$

with L in nm. The measured energy spacings for the SWNT in Fig. 9.1, *i.e.* ΔE_a1-ΔE_a4 in the negative bias range between d3-d4 and ΔE_b1-ΔE_b4 between d5-d6, are reported in Table 9.1. The CNP is difficult to determine from Fig. 9.1, but within the particle-in-a-box model, the number of anti-nodes for each discrete state follows the sequence 1,2,3,... starting from the CNP. Thus the CNP closest level spacings are $\Delta E_\mathrm{a1} = 0.22$ eV and $\Delta E_\mathrm{b1} = 0.18$ eV between d3-d4 and d5-d6, respectively. For these values,
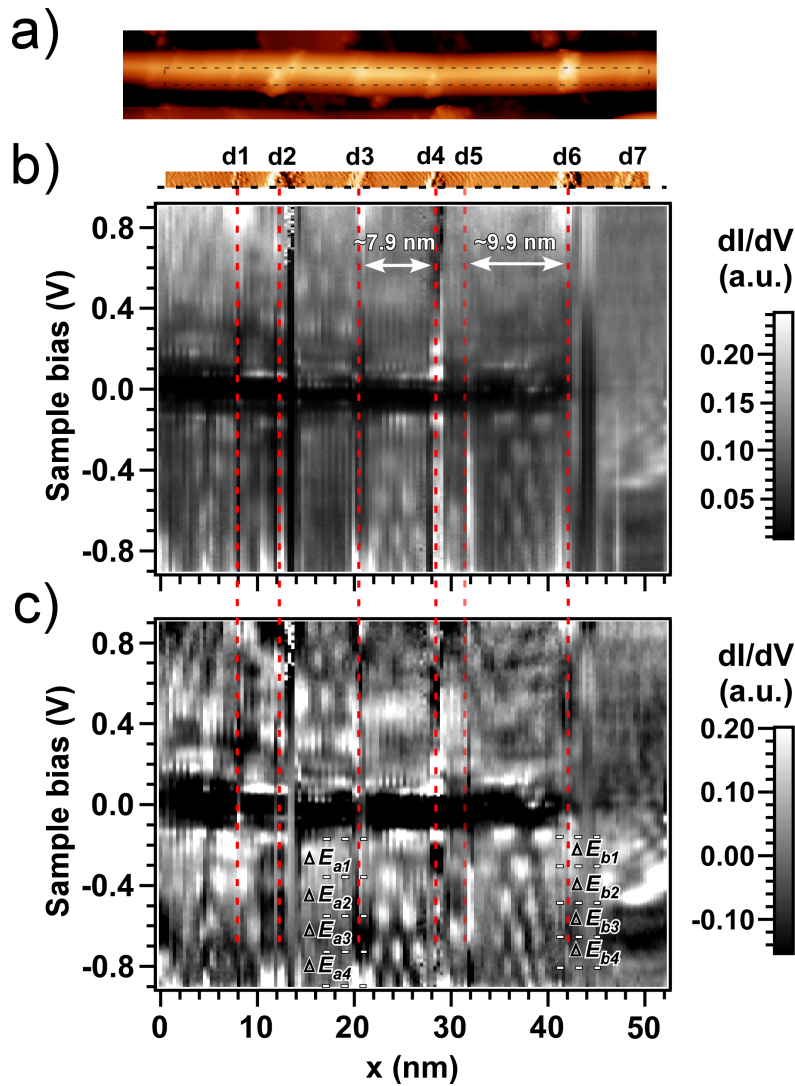
Figure 9.1: *a) Topography image of a ∼ 50 nm long portion of an armchair SWNT exposed to 200 eV Ar⁺ ions. b) Current error image of the tube section delimited by the dashed rectangle in a) with the corresponding dI/dV-scan recorded along the horizontal dashed line running over seven defect sites labeled d1-d7. c) Same dI/dV-scan as in b), with background subtraction. $\Delta z = 1.37$ nm, $V_s = 1$ V, $I_s = 0.1$ nA. b) T = 5.3 K, $U_{mod} = 12$ mV, $x_{res} = 0.34$ nm*

d3-d4	d5-d6
$\Delta E_{a1} = 0.22$ eV	$\Delta E_{b1} = 0.18$ eV
$\Delta E_{a2} = 0.19$ eV	$\Delta E_{b2} = 0.17$ eV
$\Delta E_{b3} = 0.18$ eV	$\Delta E_{b3} = 0.17$ eV
$\Delta E_{b4} = 0.17$ eV	$\Delta E_{b4} = 0.15$ eV

Table 9.1: Energy spacings between visible discrete states in the negative bias range between defect sites d3-d4 ($\sim$ 6.5 nm) and d5-d5 ($\sim$ 9.5 nm) in Fig.9.1

Eq. 9.1 gives $L = 8$ nm for the defect separation d3-d4 and $L = 9.78$ nm for d5-d6, in good agreement with the measured values at the center of the defect sites $L \simeq 7.9$ nm and $L \simeq 9.9$ nm. The slight decrease of ΔE for increasing $|V_{\mathrm{bias}}|$ can be attributed to the divergence from linearity of the real dispersion relation for energies far from the CNP [24]. We thus have a first clear indication that artificially created defects can define electron confinement regions with particle-in-a-box like states in metallic SWNTs, *i.e.* intratube QDs. Moreover, with our method where spatially close defects can be generated, we obtain level spacings which are much larger than the thermal energy at room temperature $k_{\mathrm{B}}T \simeq 25$ meV. It should be noted here that such confinement effects have been observed for medium enery Ar^+ bombardment and also for ECR N-plasma treatment. For the light ion-irradiation we made use by means of low energy ($E_{\mathrm{kin}} \approx 1$ eV) H-plasma treatment, we could not observe clear discrete energy states between defects, although electron scattering showed up by the formation of superstructures in the spatial charge density. However, quantum confinement in H-plasma treated SWNTs cannot be excluded.

The spatial resolution of about 0.34 nm for the dI/dV-scan in Fig. 9.1 is not high enough to allow a complete analysis of the discrete state features. A higher resolution dI/dV-scan recorded along the axis of a $\sim$ 16 nm long section of a metallic SWNT exposed to 200 eV Ar ions is shown in Fig. 9.2 a). Two defect sites d1 and d2 are clearly visible on the topography image. However, the spectroscopy reveals the presence of a third defect site d3 which is visible on the apparent height profile in the middle panel. The dI/dV-scan further reveals at least two discrete states in the negative bias range between d3 and d2. The energy spacing is about 170 meV, which corresponds well to the predicted value of 177 meV for a measured defect separation of about 9.5 nm. Figure 9.2 d) shows the dI/dV-scan portion recorded between the red arrows displayed in a), on which the above described background subtraction has been applied. This allows us to distinguish two additional states in the negative bias range. Discrete states

can also be observed in the positive bias range, but with lower contrast. The detailed spatial pattern of each discrete state exhibits a rapid oscillation which is modulated by a slow variation of the amplitude. In order to clearly display these oscillations, the dI/dV signals recorded between d3-d2 at $E = -0.22$ eV and $E = -0.39$ eV are plotted in Fig. 9.2 b). The wavelength of the rapid oscillation varies around 0.7 nm in both plots. The slow modulation has been fitted with the function $|\psi(x)|^2 = A + B\sin(2kx + \phi)$, where ϕ is an arbitrary phase and the factor 2 originates from the fact that STS does not probe $|\psi(x)|$ but $|\psi(x)|^2$. The wavelength of this slow modulation decreases with increasing $|V_{\mathrm{bias}}|$. The values of k given by the fit function are ~ 0.31 nm^{-1} for $E = -0.39$ eV and ~ 0.64 nm^{-1} for $E = -0.22$ eV. A detailed analysis of the oscillatory features can be obtained in the Fourier space. Therefore we performed a line-by-line zero-padding Fast Fourier Transform (FFT) of the dI/dV-scans where the offset amplitude of each line has been subtracted. The resulting $dI/dV(k, V)$ maps are plotted from $k = 0$ to about $k = 2\pi f_{\mathrm{s}}/2 = \pi/x_{\mathrm{res}}$, where f_{s} is the sampling frequency and x_{res} is the resolution in x. The sampling theorem states that the highest spectrum component of a signal must be smaller than $2\pi f_{\mathrm{s}}/2$ to avoid aliasing. For our purpose, we can show that for the usual number of 150 spectroscopy points in a dI/dV-scan, the relevant spectral features with $k < 25$ nm^{-1} are visible for a maximum analyzed length of about 20 nm. Such Fourier analysis has been performed on the dI/dV-scans displayed in Fig. 9.2 c) and d), recorded between the positions indicated by the red arrows in panel a). The original dI/dV-scan amplitude is reproduced in c) and the background subtraction has been performed in d). The corresponding $|dI/dV(k, V)|^2$ maps are displayed on the right hand side of panels c) and d). From these maps, it can be observed that the Fourier spectrum of each discrete state is composed of several components. The low frequency peaks between $k = 0$ and $k = 4$ nm^{-1} correspond to the slow modulation discussed above. The rapid oscillation in the dI/dV-scan is produced by Fourier components around $k = 11$ nm^{-1} and $k = 17$ nm^{-1}. The major part of these Fourier components are aligned along sloped lines. These lines are better defined in the $|dI/dV(k, V)|^2$ map in d) where the background subtraction has been performed on the dI/dV-scan. However, the background subtraction induces a slight distortion in the dI/dV-scan resulting in a small shift of the Fourier components of the order of 1-2%. Thus the use of this technique should be limited to increase the contrast of the spatial features. Note also that in both cases the position of the low frequency component is generally slightly distorted due to an interference artifact with the complementary negative components. Around $k = 17$ nm^{-1}, a unique positive sloped line is clearly visible, with $dE/dk \simeq 0.32$ eV·nm, whereas two lines with positive and negative slopes can be distinguished around $k = 11$
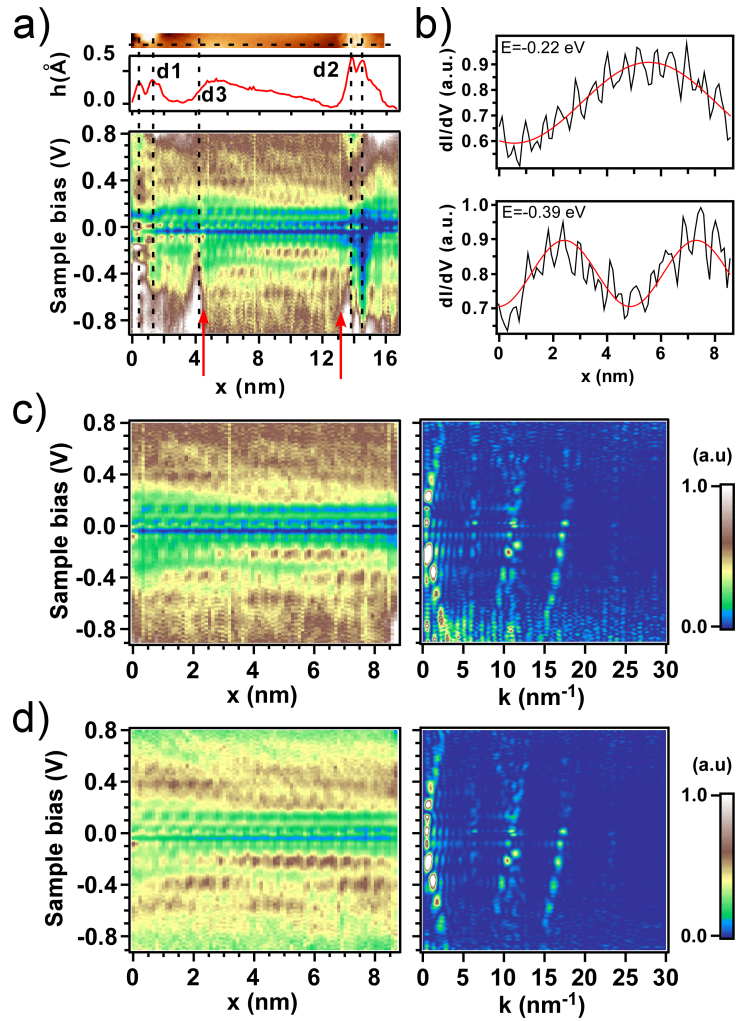
Figure 9.2: *a) Line by line flattened topography image of a metallic SWNT with three 200 eV Ar^+ ions-induced defects d1-d3, with an apparent height profile and the corresponding dI/dV -scan recorded along the same horizontal dashed line. b) dI/dV line profiles of the first two modes in the negative bias range, recorded between the two red arrows in a). The fit function is of the form $|\psi(x)|^2 = A + B\sin(2kx + \phi)$. c) dI/dV scan between the red arrows in a) with the corresponding dI/dV(k,V) map. d) The same as in c) with background subtraction. $U_s = 0.8$ V, $I_s = 0.32$ nA. b) T = 5.21 K, $x_{res} = 0.1$ nm.*
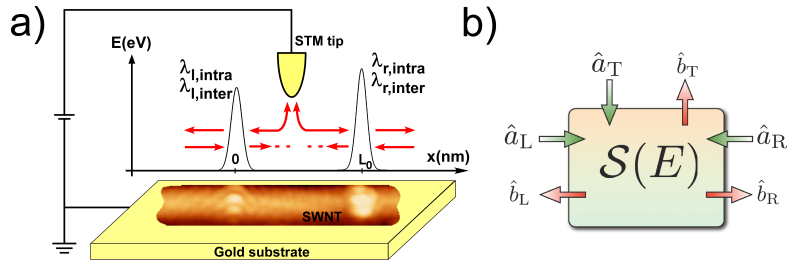
Figure 9.3: *a) Schematic diagram of a STM experiment on a SWNT with two defect sites separated by L_0, deposited on a gold substrate. b) Scheme of the scattering states used in the scattering matrix formalism.*

nm^{-1}, with an estimated slope of about 0.3 eV·nm. In order to understand the nature of the various observed features in the Fourier space, we considered two complementary theoretical approaches: the first one is based on a scattering matrix formalism and the second makes use of geometrical arguments within the Fourier projection-slice theorem. Both methods are described in detail in the following paragraphs.

9.2.1 Fabry-Pérot electron resonator model

We saw earlier that the observation of superstructures near the defects we created in SWNTs by means of ion bombardment (independently of the ion type) indicates that the latter act as scattering centers for the electrons. Therefore, an analogy can be made between a metallic SWNT with two close defects and an optical Fabry-Pérot cavity where photons experience multiple reflections between partially transmissive mirrors [161]. A Fabry-Pérot electron resonator model has been used to explain the presence of interference patterns in the source-drain differential conductance of a metallic SWNT with near-perfect ohmic contacts [162]. It is however important to note that the main difference between the nanotube electron resonator and a simple single-mode optical cavity arises from the fact that the two propagating modes in SWNTs are characterized by different wave vectors $k_1 = K + k$ and $k_2 = K - k$ which results in a higher complexity in the interference patterns, as we will see. Here we use a model illustrated in Fig. 9.3 a), based on a scattering matrix formalism taking into account the effect of the tip and where the scattering strength of the defects can be tuned. Moreover, in contrast to the approach presented in [162], we consider the possibility that a scattering event can change or not the valley index.

9.2.1.1   Scattering matrix model

The theoretical model presented here was developed in collaboration with Dr. Dario Bercioux from the Theoretical Solid State Physics group of Prof. Hermann Grabert at the University of Freiburg, Germany.

Let us start with the linear dispersion branches of the energy spectrum of a metallic SWNT: $E = \pm\hbar v_{\mathrm{F}} k$. The linearity allows us to use a field theoretical approach and write down the Hamiltonian for the SWNT as:

$$\mathcal{H}_0 = -i\hbar v_{\mathrm{F}} \sum_{\mathcal{Q},\alpha} \int dx\,\alpha : \Psi^{\dagger}_{\mathcal{Q}\alpha}(x)\partial_x \Psi_{\mathcal{Q}\alpha}(x) : \tag{9.2}$$

where $\mathcal{Q}$ is the valley index and α is the index for right ($\rightarrow$) or left ($\leftarrow$) moving electrons. The notation $::$ stands for normal ordering and is playing the role of subtracting the energy of the ground state. The operators $\Psi_{\mathcal{Q},\alpha}(x)$ and $\Psi^{\dagger}_{\mathcal{Q},\alpha}(x)$ annihilate and create an electron in the valley $\mathcal{Q}$ with motion direction α and in the position x, respectively. Here we consider an armchair SWNT. The valley indexes are then $K = 2\pi/3T$ and $K' = -K$. For a fixed energy, k denotes the displacement of the electron momentum from the CNP at $K(K')$.

As a function of the symmetry (see chapter 1.4.2) of the defects, two kind of scattering events can occur: intravalley scattering in which the valley index $\mathcal{Q}$ is not changed, and intervalley scattering in which the valley index is changed. Therefore, the Hamiltonian associated with an impurity at position x_0 is characterized by two contributions:

$$\mathcal{H}_{\mathrm{Impurity}}(x_0) = \mathcal{H}_{\mathrm{intra}}(x_0) + \mathcal{H}_{\mathrm{inter}}(x_0). \tag{9.3}$$

We model an impurity as a δ-like potential, therefore the usual scattering or intervalley scattering is described by the following Hamiltonian:

$$\mathcal{H}_{\mathrm{inter}} = \hbar v_{\mathrm{F}} \lambda_{\mathrm{inter}} \sum_{\mathcal{Q},\alpha} \Big[: \Psi^{\dagger}_{\mathcal{Q}\alpha}(x_0)\Psi_{\mathcal{Q}\alpha}(x_0) : \tag{9.4}$$

$$+ \mathrm{e}^{-2i(\mathcal{Q}+\alpha k)}\Psi^{\dagger}_{\mathcal{Q}\alpha}(x_0)\Psi_{-\mathcal{Q}-\alpha}(x_0)\Big]$$

where λ_{inter} denotes the intervalley scattering strength. The first term represents the forward scattering event which is related to the transmission of the electron without changing its momentum, while the second term represents the backward scattering event which is related to the reflection of the electron. This kind of scattering is associated with a large momentum exchange $\Delta k = 2(K + k)$.

Intravalley scattering is instead described by the following Hamiltonian:

$$\mathcal{H}_{\text{intra}} = \hbar v_{\text{F}} \lambda_{\text{intra}} \sum_{\mathcal{Q},\alpha} \Big[: \Psi^{\dagger}_{\mathcal{Q}\alpha}(x_0) \Psi_{\mathcal{Q}\alpha}(x_0) :$$

$$+ \, \mathrm{e}^{-2\mathrm{i}\alpha k} \Psi^{\dagger}_{\mathcal{Q}\alpha}(x_0) \Psi_{\mathcal{Q}-\alpha}(x_0) \Big] \tag{9.5}$$

where λ_{inter} denotes the intravalley scattering strength. The first and second terms correspond to the forward and backward scattering, respectively. This kind of scattering is associated with a long-wavelength modulation of the charge density, therefore resulting in a small value of the exchanged momentum $\Delta k = 2k$ in the backscattering event.

The STM tip is described in a semi-infinite non-interacting Fermi gas and the SWNT-tip coupling is described by the standard tunneling Hamiltonian:

$$\mathcal{H}_{\Gamma} = \hbar \sqrt{v_{\text{F}} v_{\text{F}}^{\text{STM}}} \gamma \left[\left(\sum_{\mathcal{Q},\alpha} \mathrm{e}^{-\mathrm{i}(\mathcal{Q}+\alpha k)x_0} \Psi^{\dagger}_{\mathcal{Q}\alpha}(x_0) \right) c(0) + \text{h.c.} \right] \tag{9.6}$$

where, in this case, x_0 is the position of the tip in the CNT coordinate system. The constant γ is the tunneling probability strength. The Fermi velocity of the tip $v_{\text{F}}^{\text{STM}}$ can be set to a generic value and the one of the SWNT v_{F} can be extracted from the energy spectrum by linearization around K. In the model presented here, we used the value $v_{\text{F}} = 10{\cdot}10^5$ m·s^{-1}. The first term of the Hamiltonian describes the creation of an electron in the SWNT with a momentum $\mathcal{Q}+\alpha k$ and the annihilation of an electron in the STM tip, and *vice versa* for the second term.

After solving the equations of motion for the field operators $\Psi_{\mathcal{Q}\alpha}(x,t)$ and $c(y,t)$ for two impurities separated by L_0 with scattering strengths $\lambda_{\text{inter,l}}$ and $\lambda_{\text{intra,l}}$ with $l = R, L$ the impurity index, we get the following 5×5 scattering matrix equation:

$$\begin{pmatrix} \hat{b}_{K,\text{R}} \\ \hat{b}_{K,\text{L}} \\ \hat{b}_{-K,\text{R}} \\ \hat{b}_{-K,\text{L}} \\ \hat{b}_{\text{T}} \end{pmatrix} = \mathbf{S}_{i,j}(E) \cdot \begin{pmatrix} \hat{a}_{K,\text{R}} \\ \hat{a}_{K,\text{L}} \\ \hat{a}_{-K,\text{R}} \\ \hat{a}_{-K,\text{L}} \\ \hat{a}_{\text{T}} \end{pmatrix}. \tag{9.7}$$

where $\hat{a}_{\mathcal{Q},\text{L(R)}}$ is the destruction operator for an incoming electron from the left (right) direction, $\hat{b}_{\mathcal{Q},\text{L(R)}}$ is the destruction operator for an outcoming electron from the left (right) direction, and $\hat{a}_{\text{T}}$ and $\hat{b}_{\text{T}}$ in analogy for the tip, according to the scattering scheme in Fig. 9.3 b). For fixed energy, these

operators are related to the field operators $\Psi_{\mathcal{Q},\alpha}(x)$ and $\Psi^{\dagger}_{\mathcal{Q},\alpha}(x)$ through the scattering states:

$$\Psi_{\mathcal{Q}\rightarrow}(x,t) = \frac{e^{-iEt/\hbar}}{\sqrt{2\pi\hbar v_{F}}} \begin{cases} \hat{a}_{\mathcal{Q},L}e^{-ik_{E}x} & x < x_{l} \\ \hat{b}_{\mathcal{Q},R}e^{-ik_{E}x} & x > x_{l} \end{cases} \tag{9.8a}$$

$$\Psi_{\mathcal{Q}\leftarrow}(x,t) = \frac{e^{-iEt/\hbar}}{\sqrt{2\pi\hbar v_{F}}} \begin{cases} \hat{a}_{\mathcal{Q},R}e^{-ik_{E}x} & x < x_{l} \\ \hat{b}_{\mathcal{Q},L}e^{-ik_{E}x} & x > x_{l} \end{cases} \tag{9.8b}$$

$$c(y,t) = \frac{e^{-iEt/\hbar}}{\sqrt{2\pi\hbar v_{F}^{STM}}} \begin{cases} \hat{a}_{T}e^{-ik_{E}y} & y < 0 \\ \hat{b}_{T}e^{-ik_{E}y} & y > 0 \end{cases} \tag{9.8c}$$

The current operator in the STM tip can be written as:

$$J(|y|,t) = 2ev_{F}^{STM} \iint\limits_{0}^{\infty} dE_{1}dE_{2} \left[c^{\dagger}_{E_{1}}(-|y|,t)c_{E_{2}}(-|y|,t) \right. \tag{9.9}$$
$$\left. -c^{\dagger}_{E_{1}}(|y|,t)c_{E_{2}}(|y|,t) \right] .$$

Making substitution of Eqs. 9.8 in the previous equation and thermal averaging over the ground state, we get the following expression of the differential conductance for a grounded SWNT at zero temperature:

$$\frac{dJ_{T}}{dV_{T}} = \frac{2e^{2}}{h} \left[\sum_{j=1}^{4} |\mathcal{S}_{5,j}|^{2} \right]_{E=qV_{T}} . \tag{9.10}$$

The left column of Fig. 9.4 shows the calculated $\frac{dJ_{T}}{dV_{T}}(x,E)$ maps for an armchair SWNT with an impurity separation of $L_{0}=15$ nm for different combinations of the scattering strengths $\lambda_{\text{inter,intra});L,R}$. The corresponding $\frac{dJ_{T}}{dV_{T}}(k,E)$ maps performed within a line-by-line zero-padding FFT (with offset subtraction) are displayed in the right column. Here we consider the same intervalley and intravalley scattering strengths for both impurities. In Fig. 9.4 a), we have a low scattering strength with $\lambda_{\text{inter,l}} = \lambda_{\text{intra,l}} = 0.1$ and a 10 times higher scattering strength in b) with $\lambda_{\text{inter,l}} = \lambda_{\text{intra,l}} = 1$. Note that since the energy spectrum $E = \pm\hbar v_{F}k$ on which the calculation is based is fully symmetric with respect to the CNP, occupied $(E < 0)$ and unoccupied $(E > 0)$ states are equivalent. Thus, without loss of generality, we can consider only the occupied states.

For both cases, in terms of a resonant cavity, we distinguish three resonant modes with one, two and three anti-nodes corresponding to the low frequency components in the $\frac{dJ_{T}}{dV_{T}}(k,E)$ maps, with an energy spacing of
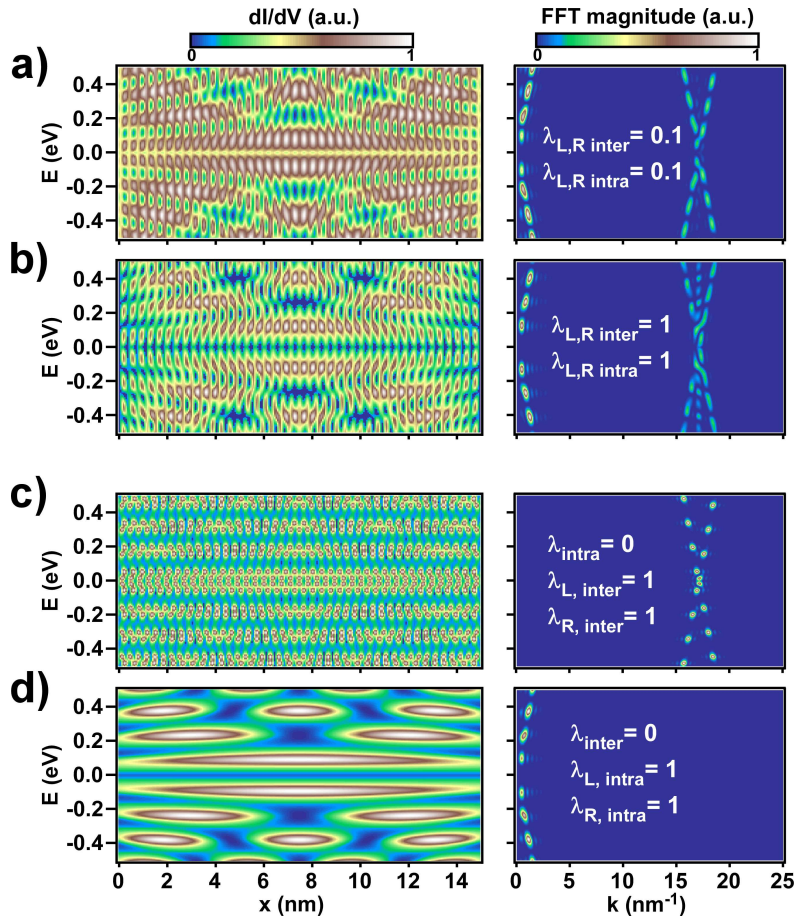
Figure 9.4: $\frac{dJ_T}{dV_T}(x,E)$ and corresponding $\frac{dJ_T}{dV_T}(k,E)$ calculations for different values of $\lambda_{inter,intra;L,R}$: $\lambda_{inter,l} = \lambda_{intra,l} = 0.1$ in a) and $\lambda_{inter,l} = \lambda_{intra,l} = 1$ in b). c) and d) One of the scattering channel is switched off with $\lambda_{intra,l} = 0$ in c) and $\lambda_{inter,l} = 0$ in d).

$\Delta E = \frac{h v_F}{2L}$. These intravalley scattering contributions correspond to interference patterns formed by the coherent superposition of left- and right-moving electron plane waves of the form $\psi(x) = e^{\pm ikx}$. The interference pattern is thus of the form $|\psi(x)|^2 = \left|e^{+ikx} + e^{-ikx}\right|^2 \sim \cos(2kx + \phi)$. Thus the Fourier spots corresponding to modes 1-3 are aligned along a line which correspond to the linear energy spectrum $E(k)$ of the SWNT, with a slope

of $2\hbar v_{\mathrm{F}}$ due to the fact that $\frac{dJ_{\mathrm{T}}}{dV_{\mathrm{T}}}(x, E) \propto |\psi(x)|^2$.

The rapid oscillation in the $\frac{dJ_{\mathrm{T}}}{dV_{\mathrm{T}}}(k, E)$ map is mainly produced by Fourier contributions which are aligned along two lines with opposite slopes of $\pm 2\hbar v_{\mathrm{F}}$, crossing at the CNP for $k \simeq 17$ nm^{-1}. This value of k corresponds to the projection of $\mathbf{K}$ on the $k_{\parallel}$ axis multiplied by 2, *i.e.* $k = 2 \cdot \frac{2\pi}{3a}$ with $a = \sqrt{3} \cdot a_{cc} = 0.246$ nm. These intervalley scattering contributions correspond to interference patterns formed by the coherent superposition of left- and right-moving electron plane waves with wavevectors $\pm (K \pm k)$. The interference pattern is thus of the form $|\psi(x)|^2 \sim \cos [2 (K \pm k) x + \phi]$. In both cases, we can observe that the position in energy of the Fourier spots belonging to different branches are not resonant. We can show that this effect depends on the impurity spacing L_0. These states are resonant if $K = m\pi/L_0$, *i.e* if K is a multiple of the spacing between two consecutive allowed values of $k_{\parallel}$. Note that stronger scatterers as in b) induce resonant states which are narrower in energy, in analogy with the larger finesse in an optical cavity for a higher reflection strength of the mirrors [161].

Now we consider two examples where one of the two scattering channels is switched off. The case for $\lambda_{\mathrm{intra}} = 0$ ($\lambda_{\mathrm{inter;R,L}} = 1$) is depicted in Fig. 9.4 c). As expected, only Fourier components along the dispersion lines crossing at the CNP are present. It is however worth noticing that if the resonance condition $K = m\pi/L_0$ is fulfilled, we will have the superposition of two standing waves of the form $\cos [(K + k) x + \phi]$ and $\cos [(K - k) x + \phi]$, which will result in a beating pattern at the resonance positions, composed of a rapid oscillation modulated by a slow variation of the form $|\psi(x)|^2 \sim \cos^2(Kx) \cdot \cos^2(kx)$. The case for $\lambda_{\mathrm{inter}} = 0$ ($\lambda_{\mathrm{intra;R,L}} = 1$) is shown in Fig. 9.4 d). As expected, only the intravalley low frequency components are present in the Fourier space, resulting in well-defined modes without rapid oscillation.

From a comparison between the measured $dI/dV(k, V)$ map in Fig. 9.2 and the simulations above, one can observe that the low frequency behavior in both the simulation and the measured $dI/dV(k, V)$ map in Fig. 9.2 are in good agreement. However, some differences can be observed for higher frequencies. The theoretical model typically shows two dispersive branches crossing at $k \simeq 17$ nm^{-1} whereas at this position the measurement shows a strong dispersive branch with a slope of $dE/dk \simeq 0.32$ eV·nm which is in very good agreement with the theoretical value of $2\hbar v_{\mathrm{F}} \simeq 0.329$ eV·nm. Moreover, the presence of frequency contributions around $k = 6$ nm^{-1} and $k = 11$ nm^{-1} do not come out of our model. The origin of these contributions can be understood from geometrical arguments as we will show in the following section.

9.2.2 Fourier projection-slice theorem

A STM topography line recorded along the axis of a SWNT can be regarded in a first approximation as a slice oriented in the direction of the translational vector $\mathbf{T}$ through the charge density $|\psi(\mathbf{r})|^2$ of a sheet of graphene. In the presence of scattering centers like structural defects, we saw in chapter 4.5 that the large momentum scattering-induced $(\sqrt{3} \times \sqrt{3})\,R30°$ super-structure can be reproduced by a linear combination of six plane waves having vectors $\mathbf{k}_j$ corresponding to the six Fermi vectors of the first BZ: $\psi(\mathbf{r}) = \sum_{j=1}^{6} \phi_j \cdot e^{i\mathbf{k}_j \cdot \mathbf{r}}$ with $|\mathbf{k}_j| = \frac{4\pi}{3a} \simeq 17$ nm^{-1}. The 2D-FFT of this function for a given set of complex amplitudes $\{\phi_j\}_{j=1}^{6}$ is shown in Fig. 9.5 a), left panel. The charge density $|\psi(\mathbf{r})|^2$ and its corresponding FFT with additional Fourier spots resulting from the $||^2$ operation are plotted in Fig. 9.5 a), middle and right panel, respectively. The underlying atomic honeycomb network is highlighted in white in the middle panel. In the right panel, the blue encircled spots correspond to the K points whereas the red encircled ones are the reciprocal lattice points G. In the STM, the amplitude of the charge density on a line is measured (here at E_F since only the contributions at the K (K') points are taken into account). Figure 9.5 b) shows two simulation examples of a STM measurement along the axis of an armchair SWNT with scattering centers (this could be measured between two defects). The upper panel in b) shows the charge density contribution measured with a sharp tip, where only the intensity in the range -0.05 nm $<$ y $<$ 0.05 nm contributes to the STM signal. The normalized resulting STM signal which is given by $I(x) = \int_{y_-}^{y_+} |\psi(x,y)|^2 \, dx$ is plotted in blue in Fig. 9.5 c). The situation for a blunt tip (low resolution) where the STM signal originates from a wider zone -0.2 nm $<$ y $<$ 0.2 nm is shown in the lower panel of b) and the corresponding STM signal is plotted in red in Fig. 9.5 c). As can be seen in Fig. 9.5 d), the Fourier analysis (blue(red) spectrum for sharp(blunt) tip) of both STM signal curves reveals four contributions which are located in this case at multiples of $k = \frac{2\pi}{3a} \simeq 8.5$ nm^{-1}. Interestingly, the spot at 17 nm^{-1} becomes dominant when the tip resolution decreases. The origin of the four contributions for an armchair SWNT can be understood and generalized to different chiralities within the so-called Fourier projection-slice theorem [163]. In 2D, a version of this theorem states that the Fourier transform of a slice through a 2D function is equal to the projection of the 2D Fourier space on a line passing through the origin and which is parallel to the direction of the slice. Since in our case the slice is 2D with a profile given by $I(x,y)$ on a width $y_- < y < y_+$, the projected components in the Fourier space are weighted in direction perpendicular to the projection line by the Fourier transform of the y-resolution profile in
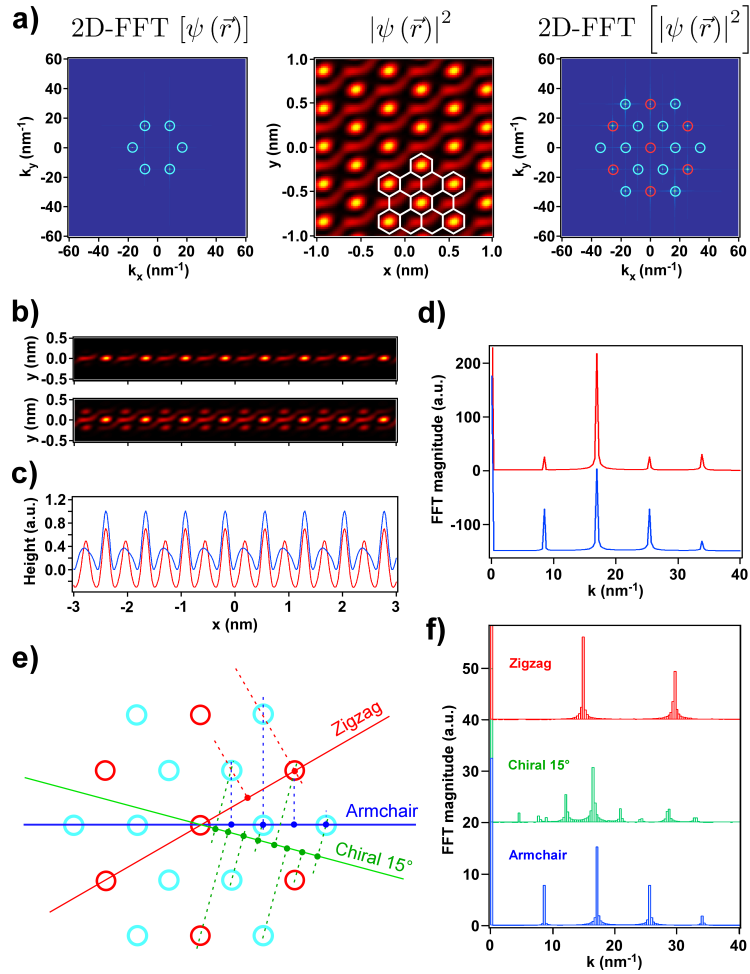
Figure 9.5: *a) left: Reciprocal space with the first BZ spots, middle: corresponding $\left(\sqrt{3} \times \sqrt{3}\right) R30°$ in the real space, right: Reciprocal space with spots corresponding to $|\psi|^2$. b) upper panel: Charge density contribution for the measurement with a sharp tip along the axis of an armchair tube, lower panel: the same for a blunt tip. c) Resulting normalized STM signal computed with $I(x) = \int_{y_-}^{y_+} |\psi(x,y)|^2 \, dx$, blue(red) curve for a sharp(blunt) tip. d) Corresponding FFT. e) and f) Illustration of the Fourier projection-slice theorem with the projetions in the reciprocal space for different chiralities in e) and the Fourier transforms of the STM signals for the different chiralities for a sharp tip in f).*

the real space. This is illustrated in Figs. 9.5 e) and f). The FFT of the computed STM signal (for a sharp tip) for three different tube chiralities, *i.e.* zigzag, armchair and chiral with θ=15°, are displayed in e). The origin of the different Fourier spots can then be understood from the projection diagram in the Fourier space in f), according to the Fourier projection-slice theorem. For a blunt tip, the spots which are the closest to the projection line are dominant. Thus, it can be shown for a blunt tip that the intensity in the three cases will be dominated by the peaks at 17 nm^{-1} for the armchair, 29.4 nm^{-1} for the zigzag and 16.4 nm^{-1} for the chiral tube. Generally, the intensity of the different spots will depend on two factors which are the defect scattering strength giving the complex amplitude in the plane wave linear combination and the resolution of the tip. In the model above we only considered the Fourier components at the CNP (E_F if no doping). In the case of a Fourier transform of a measured dI/dV-scan, *e.g* the $dI/dV(k,V)$ map in Fig. 9.2, we can show that all the obtained spots belong to dispersive branches. For the case of the $\theta = 15°$ chiral SWNT in Fig. 9.5 e), one can observe that the projected spots originate from both K points (BZ of graphene) and G points (reciprocal lattice of graphene). It can be understood that the projected spots at different bias voltages are only dispersive for the K points and those originating from the G points show dispersive and non-dispersive behaviors. The non-dispersive branches correspond to the lattice components in the STM signal, which are not taken into account in our model.

Within the two theoretical models described above, a better understanding of the features observed in the $dI/dV(k,V)$ map in Fig. 9.2 for a chiral SWNT with $\theta = 14.5 \pm 1.5°$ is possible. The origin of the Fourier spots observed around $k \simeq 6$ nm^{-1}, $k \simeq 11$ nm^{-1} and $k \simeq 17$ nm^{-1} can now be explained by the projection of Fourier components of the 2D-FFT of the measured $|\psi|^2$ on a line forming an angle of 14.5±1.5° with the armchair direction. The higher intensity for the components around $k \simeq 17$ nm^{-1} can be explained by the limited resolution of the tip. Moreover, the position of the CNP can be estimated by measuring the energy position of the crossing point of two branches originating from the same valley. Note that when it is possible, this measurement should be made from high frequency components since the position of low frequency spots can be slightly distorted as explained above. Here we find a shift of the CNP with the Fermi energy of about $\delta E = 30$ meV. This is far away from the usually reported value of $\delta E = 0.3 \pm 0.1$ eV for SWNT deposited on gold [164]. This indicates a low charge transfer from the tube to the substrate.

However, some observations remain unclear, as for example the fact that the branch corresponding to the π^* band strongly appears around $k \simeq 17$ nm^{-1} (positive slope) and that the one corresponding to the π band is very
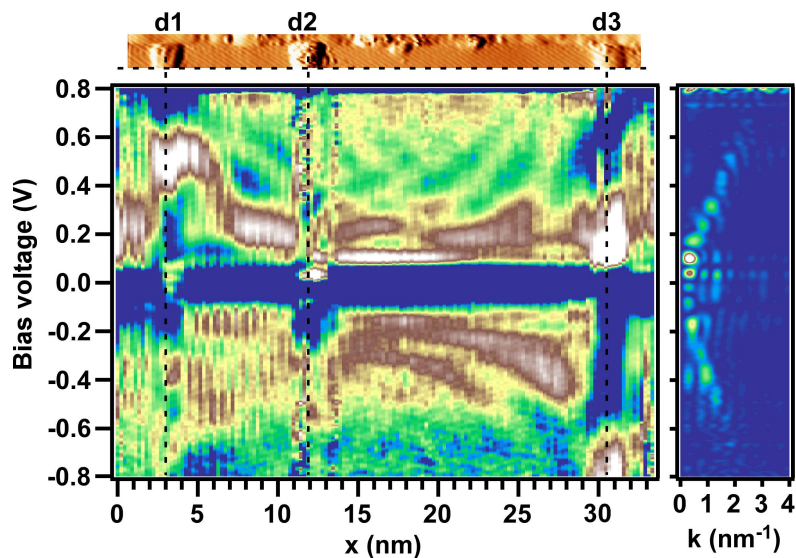
Figure 9.6: *STM current error image of a metallic SWNT with three defect sites d1-d3 produced by an exposition to 1.5 keV Ar^+ ions, with the dI/dV-scan with background subtraction recorded along the horizontal dashed line. The corresponding $dI/dV(k,V)$ map limited to low frequencies contributions is displayed on the right-hand side. $V_s = 0.8$ V, $I_s = 0.3$ nA, $T = 5.3$ K, $x_{res} = 0.22$ nm.*

weak (negative slope), instead of at least two branches predicted by the scattering model. This could be explained by symmetry arguments where the specific parity of one or both defects hinders or decreases scattering of electrons belonging to the π band [75].

9.2.3   Asymmetric boundary conditions

Figure 9.6 shows a current error image of a metallic SWNT which has been exposed to 1.5 keV Ar^+ ions, and the corresponding dI/dV-scan recorded along the tube axis, through three defect sites labeled d1-d3. The important effect we would like to point out here is the asymmetry in the interference patterns of the confined states observed in the dI/dV-scan between d2 and d3. Instead of clear "textbook-like" modes as shown in the example above in Fig. 9.2, here the interference patterns tend to form curved strips, especially pronounced in the negative bias range. However, the $dI/dV(k,V)$ map on the right hand side corresponding to the zone between d2 and d3 clearly shows well-defined low frequency spots with an average energy separation of about 90 meV. This is in good agreement with Eq. 9.1 which gives $\Delta E \simeq 93$
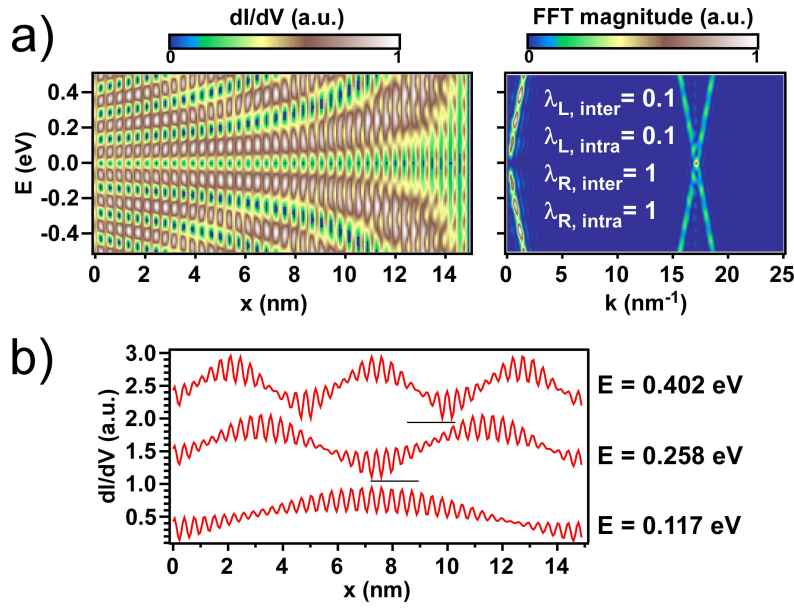
Figure 9.7: *a)* $\frac{dJ_T}{dV_T}(x, E)$ *simulation within the scattering matrix approach and corresponding* $\frac{dJ_T}{dV_T}(k, E)$ *map for the situation with asymmetric boundary conditions* $\lambda_{inter,intra;L} = 0.1$ *and* $\lambda_{inter,intra;R} = 1$. *b)* *Line profiles in* $\frac{dJ_T}{dV_T}(x, E)$ *along the x-axis for the energy given by the low frequency Fourier spots in the positive bias range.*

meV for a measured defect separation L_0 of about 19 nm.

The curved shape of the interference patterns can be understood within the scattering matrix approach described above. Up to this point, we only considered the cases with two identic impurities, *i.e.* with the same scattering strengths λ, giving rise to interference patterns (see Fig. 9.4) which are perfectly symmetric with respect to the mirror axis at $x = L_0/2$. An example of a $\frac{dJ_T}{dV_T}(x, E)$ map for different $\lambda_{R,L}$'s, *i.e.* $\lambda_{inter,intra;L} = 0.1$ and $\lambda_{inter,intra;R} = 1$, is displayed in Fig. 9.7 a). A clear asymmetry characterized by strips with increasing curvature when moving from the impurity with the smallest scattering strength on the left to the one with higher scattering strength on the right is now visible. In spite of this asymmetry, energy equidistant low frequency spots are still visible in the $dI/dV(k, V)$ map on the right hand side, with the difference that they are broadened along the dispersion line. The same effect is observed for the spots on the dispersion lines crossing at $k = 17$ nm^{-1}. The line profiles along the x-axis

at energy positions corresponding to the three low frequency spots in the negative bias range are plotted in Fig. 9.7 b). One can note the "resonant mode" nature of the interference patterns. According to this model, we can now explain the formation of curved strips between d2 and d3 in the dI/dV-scan in Fig. 9.6 by different scattering strengths for the the defects, with $\lambda_{d2} > \lambda_{d3}$. Figure 9.8 shows another example where this asymmetry effect is even more pronounced. Here we locally cut the SWNT at the position of a defect site in order to change the scattering strength. Such cut can be achieved by applying a voltage pulse of about $|V| = 5$ V at constant height at a defined location [165]. The result of this operation can be seen in the topography (upper panel) and current error (lower panel)images in Fig. 9.8 a), where a metallic SWNT has been cut at two positions labeled cut 1 and cut 2, separated by about 30 nm. The obtained short tube contains two defect sites d1 and d2. A pronounced asymmetry effect in the positive bias range between cut 1 and d1 can be observed in the corresponding dI/dV map recorded along the short tube axis. According to the simulation in Fig. 9.7, the curved shape indicates a much larger scattering strength a the cut position than at d1. This can be intuitively understood as the cut can be regarded as a hard wall potential for the electrons, which means that the transmission is strictly zero. However, this does not automatically mean that the coherent scattering strngth is very high. Indeed, the incoherent scattering and the electron absorption due to tube-substrate interaction a the cut can reduce the coherent scattering strength. It should be noted that the interference patterns are different in the negative bias range where quasi-symmetric resonant modes can be observed. This behavior suggest energy-dependent boundary conditions. In Fig. 9.8 c), we show the situation when a second cut is performed at the position of d1. We observe that the earlier clear asymmetry in the positive bias range is no more present. Instead, we can distinguish quasi-symmetric modes. This second recorded dI/dV-scan is not distorted by a possible tip change happening during the voltage pulse since the confined states observed between d1 and d2 in a) are still clearly visible in b), with a slight increase of the energy spacing of about 90 meV due to a reduction of the resonator length. We can suggest that since no clear asymmetry of the interference pattern is visible, the structure of both tube ends is similar or at least their coherent scattering strengths are close.

Sometimes however, two cuts can have different scattering strengths as we will discuss in the following. Figure 9.9 a) displays a 23 nm long section of a metallic SWNT irradiated with 200 eV Ar^+ ions showing two defect sites separated by $L_0 \simeq 17.5$ nm. The dI/dV-scan and also the $dI/dV(k, E)$ show the appearance of well-defined modes with an energy spacing of about 100 meV as expected the separation of the two defects. The interference
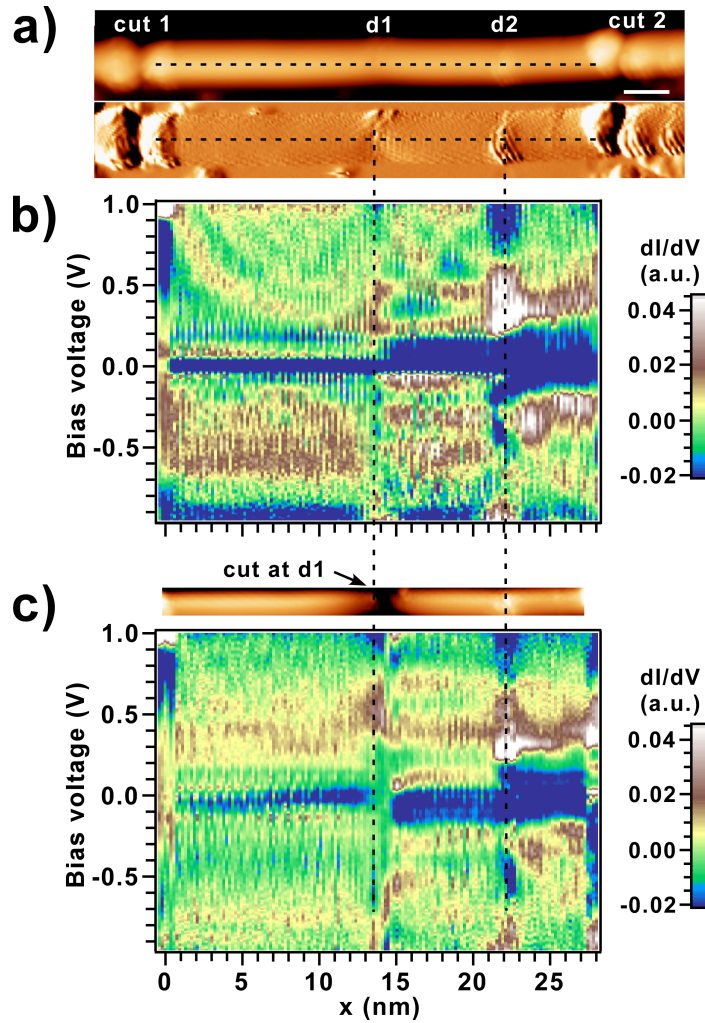
Figure 9.8: *a) STM topography and current error image of a metallic SWNT exposed to 200 eV Ar$^+$ ions. Two cuts produced by voltage pulses at $|V| \simeq 5$ V have been performed at positions cut 1 and cut 2, on both sides of defect sites d1 and d2. b) dI/dV-scan recorded along the horizontal dashed line in a), with background subtraction. c) STM topography image and corresponding dI/dV-scan for the situation where a third cut has been performed at position d1. $V_s = 1$ V, $I_s = 0.32$ nA, $T = 5.23$ K, $x_{res} = 0.18$ nm.*
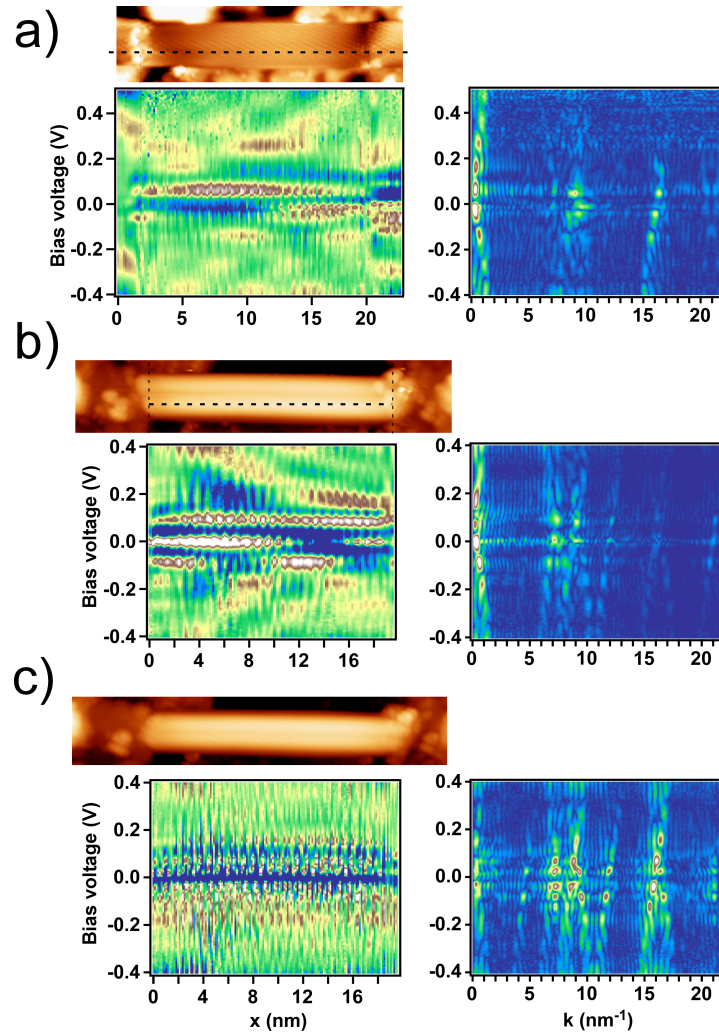
Figure 9.9: *STM topography image and corresponding dI/dV-scan of a metallic SWNT exposed to 200 eV Ar$^+$ ions. a) Situation with two defect sites. b) Situation where two cuts have been performed at the defect positions by means of voltage pulses at $|V| \simeq 5V$. b) A third voltage pulse has been performed close to the left end. $V_s = 0.5$ V, $I_s = 0.3$ nA, $T = 5.22$ K, $x_{res} = 0.15$ nm.*

pattern does not show curved stripes and therefore indicates similar scattering strengths at the defects. There is a discernable symmetry breaking

with respect to the y-axis at $x = L_0/2$, which should be the position of a mirror-axis. This points to different scattering phase shifts at the two defect sites. Note that our Fabry-Pérot model does not take the phase shift into account. When the tube is cut at both defect sites as shown in Fig. 9.9 b), the mode pattern develops the typical asymmetric stripe pattern, which we found to be characteristic for different scattering strength (here with $\lambda_L > \lambda_R$). Applying a further cutting pulse close to the left end of the tube results in the disappearance of the asymmetry as shown in Fig. 9.9 c), but also to a weaker signature of the resonant modes pattern, indicating the reduction of the scattering strength at the left end of the tube, so that now the left and right ends have a similar scattering strength. This sequence of experiments indicates that even though one can expect tube ends to be hard potential walls for the electrons, the coherent scattering strengths at ends can be different. This might be a result of incoherent scattering, *e.g* due to different symmetry properties of the ends or due to a stronger tube-substrate interaction at the tube end, induced by the cutting procedure, leading to electron absorption instead of scattering.

For the three $dI/dV(E, k)$ maps in Fig. 9.9, it is interesting to notice the change of the intensity of the dispersive high frequency components, which are related to large momentum intervalley scattering. According to the discussion in chapter 9.2.2, there can be two reasons for this changes. First the change of the $(\sqrt{3} \times \sqrt{3}) R30°$ superstructure pattern. Due to the small periodicity of this pattern of 4.26 $\mathring{A}$, even small changes of the scatter configuration (by a characteristic distance comparable to 4.26 $\mathring{A}$) will lead to a significant change of the pattern and correspondingly for the associated Fourier components. Secondly, as we have seen earlier, the tip resolution can strongly affect the intensity of the high frequency components according to the Fourier projection-slice theorem.

In conclusion, we can state that the different kind of ion bombardment-induced defects and the extreme case of a tube end can show energy-dependent boundary conditions. A better understanding of this effect is important in view of a future controlled realization of quantum devices based on intratube QDs, like *e.g* single-electron transistors. A first step could be achieved *e.g.* within calculations based on the scattering matrix model above accounting for energy-dependent scattering strengths and scattering phases.

Conclusion and Outlook

In this work, we demonstrated by means of LT-STM/STS investigations that the local electronic structure of individual SWNTs can be dramatically changed by the introduction of defects produced by low- and medium-energy ion bombardment. A general observation was the appearance of new electronic states at different energy positions for semiconducting and metallic tubes, generally strongly localized in space at the defect positions ($\sim$ 2nm spatial extent along the tube axis). Furthermore, we demonstrated the ability of our method to create intra-tube room temperature active QDs in metallic SWNT. These two main results can have important implications for optics and transport applications. Although our work has concentrated on the investigation of QDs in metallic tubes, we have also observed, in a few cases, QD states in semiconducting ones. The data of these observations have not been included in this work as analysis is still under way and because we only have very few measurements of these cases. But as the fabrication of intra-tube QDs in semiconducting SWNTs can be of high importance for quantum information applications, we think that it is very worthwhile to investigate in future works the quantum confinement in semiconducting tubes in much more detail.

From the point of view of optics, the observed gap states can have important implications. They can act as local recombination centers for electrons and holes by emission of photons of well-defined energy [125]. Investigations on the optical properties of such defect structures were performed in collaboration with the Quantum Transport Group at the TU Delft, the Netherlands. The presence of ion bombardment-induced defects could clearly be observed by means of Raman scattering experiments. However, our preliminary measurements of a possible photoluminescence signal from the defect sites on tubes deposited by spin coating on a nanoporous surface (Al_2O_3) failed. This is most probably due to a quenching of the luminescence by the substrate or the presence of metallic tubes in bundles. Thus, to be able to probe the optical properties of such gap states, one need to define specific devices where large portions of individual tubes are decoupled from the substrate, like $e.g$ in suspended tubes configurations [166]. This might require

samples, where SWNTs are CVD grown over micro-fabricated trenches, to insure high purity.

Transport measurements of SWNTs with ion bombardment-induced defects will be important in order to understand the correlations between the local modifications of the electronic structure and the transport properties of the tubes. Simultaneous STM investigations and transport measurements in the same setup have already been reported [167], but the possibility to address different SWNTs with different chiralities and defect configurations has never been realized. It should be noted that STM/STS investigations on a micro-fabricated device is highly challenging from the experimental point of view.

In our experiments with N ion induced defects we could not find signatures which can be clearly attributed to a n-type doping. We think that this results should not discourage further investigations in this direction as we have explored only the low ion energy and defect density regime. It might well be that the ion energy in our experiments was too low for the creation of substitutional donor sites. This energy could be gradually increased by an appropriate biasing of the substrate. Also it can be imagined that annealing steps at elevated temperatures ($> 1000^\circ$C) are necessary to convert, e.g. vacancy N-adatom configurations into well defined substitution N sites, what can be envisioned using Pt instead of gold as substrates. There are still many experimental routes to be explored in this direction.

The recent reports on magnetism induced by proton irradiation of carbon systems [87–89] of course also open an interesting window of opportunity, to search for similar effects in SWNTs. Here the characterization of the possible defect configurations and the understanding how they change the local electronic structure, as we carried them out here, may help the understanding of defect related magnetism in carbon systems.

At least, the recent ability to isolate a single monolayer of graphite, the so-called graphene, has ignited intense research activities to elucidate the electronic properties of this novel two-dimensional (2D) electronic system [21]. We were also interested in the electronic properties of graphene and defects in graphene. In order to get a graphene sample easily accessible to STM investigations, we annealed a silicon carbide (SiC(0001)) film at about 1500 K in a way to desorb the first silicon layers and form graphene layers at the surface [168]. We obtained interesting results as for example small graphene flakes with armchair edges which showed strong signatures of large momentum scattering, as shown in Fig. 9.10. Deeper investigations have to be performed on this system in order to test the reproducibility of such flake shapes, which could also be interesting for quantum optics experiments.

The proven possibility to lithographically pattern graphene into device structures [169], which features sizes of the order of 10 nm, indicates that
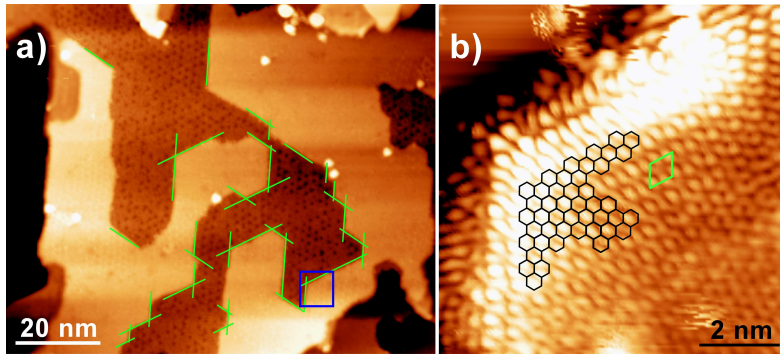
Figure 9.10: *a) STM topography image of SiC(0001) annealed at 1500 K. Armchair edges of the observed flakes are highlighted in green. $V_s = 3$ V, $I_s = 0.1$ nA, $T = 5.4$ K. b) Detailed image corresponding to the blue square in a), with unit cell of the $\left(\sqrt{3} \times \sqrt{3}\right) R30°$ reconstruction indicated in green. $V_s = 0.1$ V, $I_s = 0.2$ nA, $T = 5.4$ K.*

graphene might be a better candidate than SWNTs for future nanoelectronic devices, at least from the technological point of view. No matter whether this will be the case or not, the importance to understand defects and the possibility to engineer electronic properties by defects is the same for graphene or SWNTs. Therefore, besides further investigations of defects on SWNTs, *e.g.* electronic changes induced by a functionalization, the STM/STS characterization of ion-induced defects on graphene constitutes a natural continuation on the work presented here.

Appendix A

Density Functional Theory simulations

To understand the nature of the created defects and the type of the induced electronic modifications, we calculated the atomic and electronic structure of nanotubes with different defect structures within the framework of density-functional theory (DFT). We used Projector Augmented Wave (PAW) potentials [170] to describe the core electrons and the Generalized Gradient Approximation (GGA) [171] for exchange and correlation implemented in the plane-wave code VASP [172]. All structures were fully relaxed until the forces acting on atoms were less than 0.02 eV/Å. A kinetic energy cutoff of 400 eV was found to converge the total energy of our system to within meV. The same accuracy was also achieved with respect to the **k**-point sampling of the BZ (normally 9 points along the tube axis). The band structure and LDOS were calculated with a larger number of **k**-points (32-48 points), while the electron density was kept fixed. The calculated STS spectra represent LDOS on atoms within the range of 3 Å from the adatoms averaged with equal weights.

We considered $(10, 0)$, $(8, 4)$ and $(8, 0)$ nanotubes with up to 120 carbon atoms in the simulation cell. We could not simulate the nanotubes with the chiral indices determined from the experiments due to the prohibitively large unit cells of these tubes. As our theoretical results for the investigated tubes are in qualitative agreement with the experimental observations, we believe that our simulations for the three tubes are sufficient to generalize our results to all semiconducting SWNTs.

All the details concerning the plane-wave VASP code can be found in http://cms.mpi.univie.ac.at/vasp/vasp/vasp.html

Appendix B

Ab initio *calculations of vacancy-H complexes*
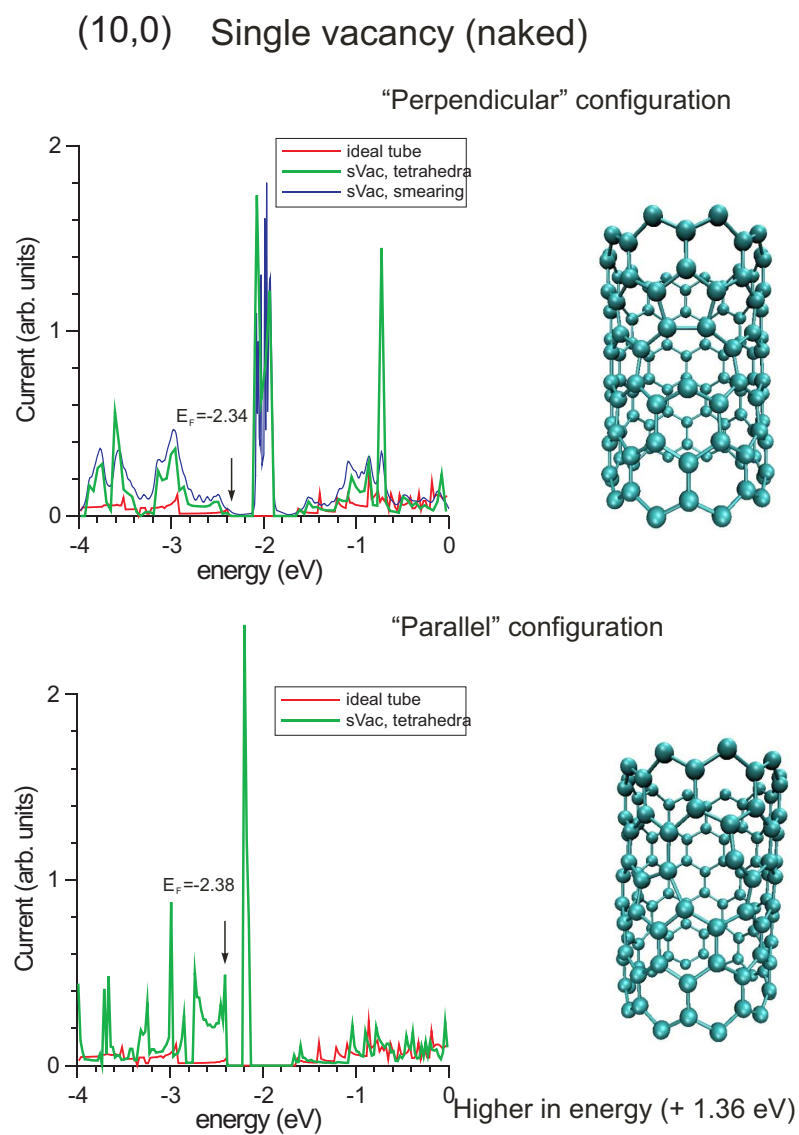
(10,0)   Single vacancy (naked)

Figure B.1: *Upper panel: Ball-and-stick model and LDOS of a (10,0) SWNT with a naked SV with the saturating bond oriented perpendicular to the tube axis. Lower panel: the same for the "parallel" configuration.*
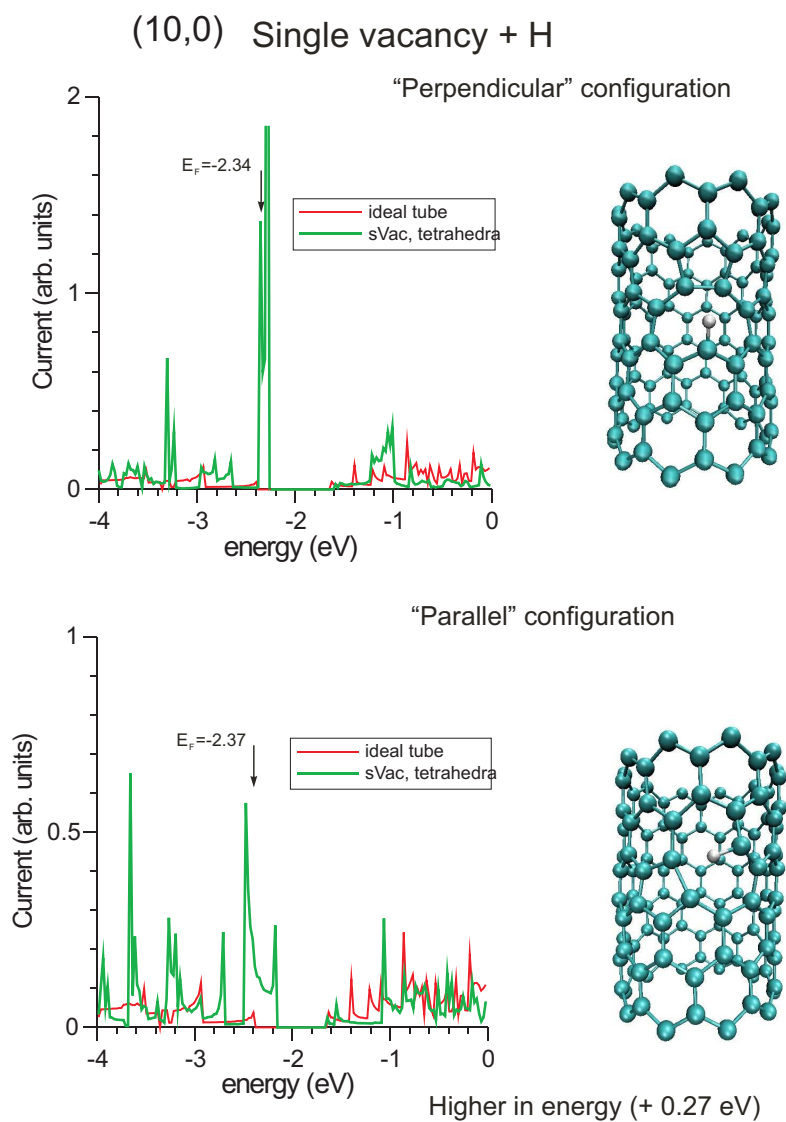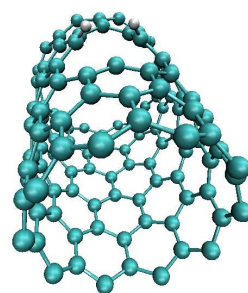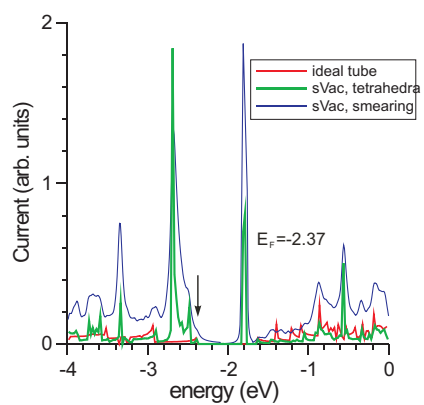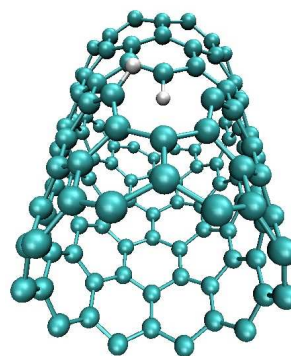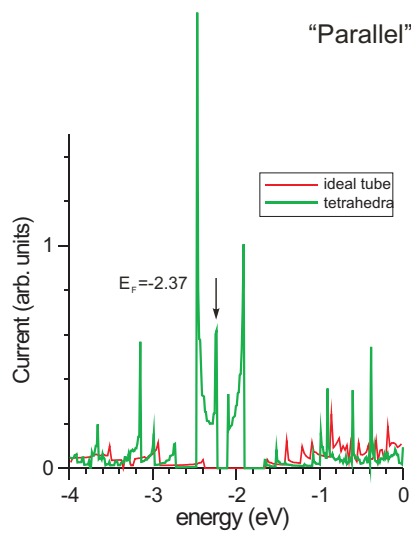
Figure B.2: *Upper panel: Ball-and-stick model and LDOS of a* (10, 0) *SWNT with a SV decorated with one H adatom, with the saturating bond oriented perpendicular to the tube axis. Lower panel: the same for the "parallel" configuration.*

Figure B.3: *Upper panel: Ball-and-stick model and LDOS of a* (10, 0) *SWNT with a SV decorated with two H adatom, "perpendicular" configuration. Lower panel: the same for the "parallel" configuration.*
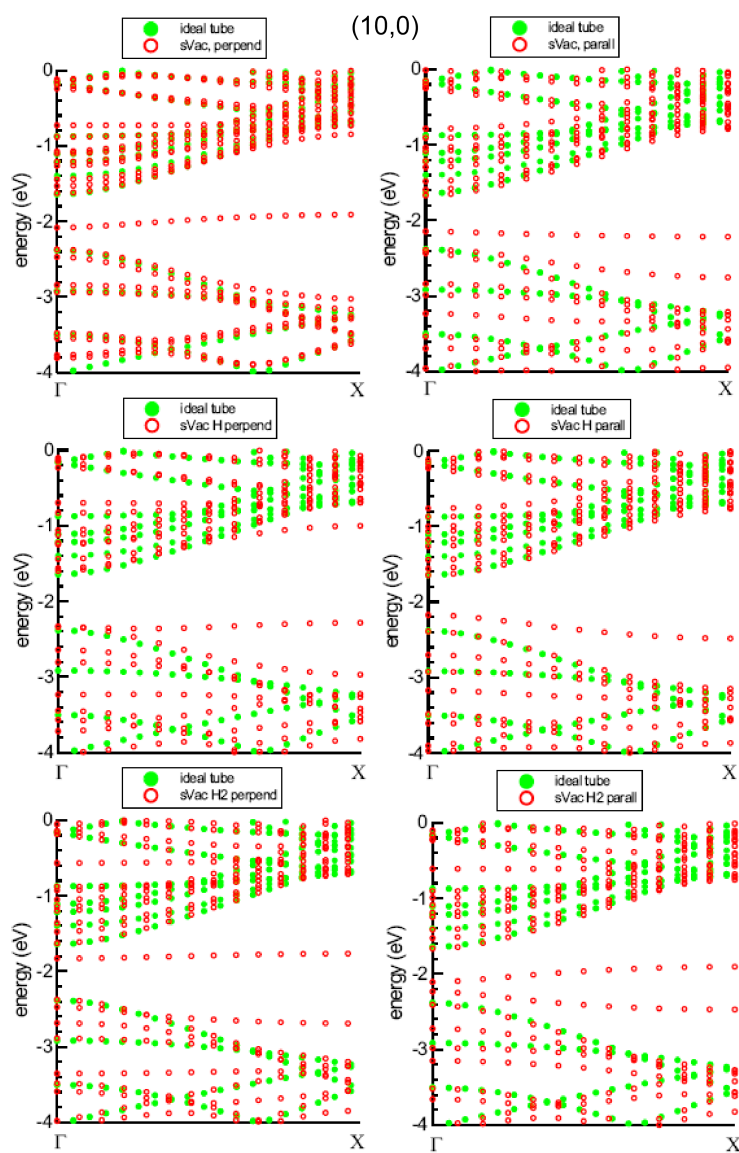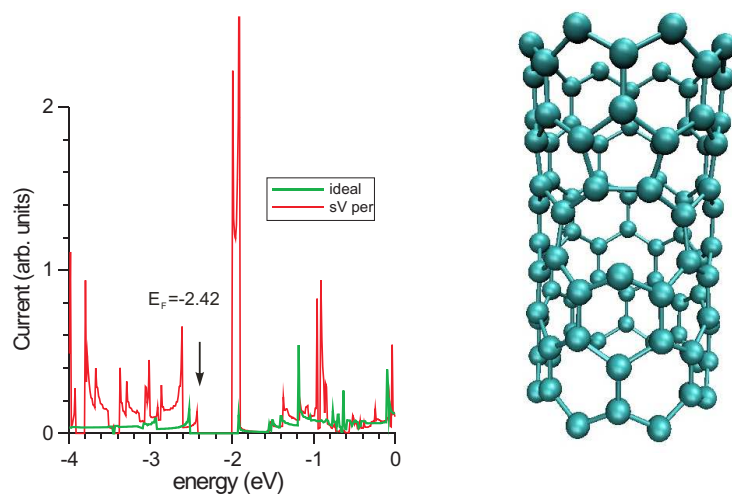
Figure B.4: *Band structures for* $(10,0)$ *SWNTs with the different defect configurations presented in Figs. B.1, B.2 and B.3.*

(8,0) tube, VASP calculations

Single vacancy (naked)

"Perpendicular" configuration

"Parallel" configuration

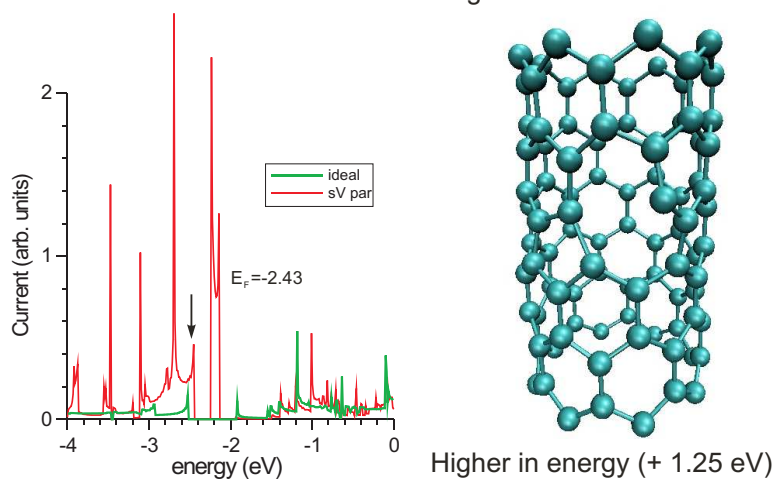
Higher in energy (+ 1.25 eV)

Figure B.5: *Upper panel: Ball-and-stick model and LDOS of a* (8,0) *SWNT with a naked SV with the saturating bond oriented perpendicular to the tube axis. Lower panel: the same for the "parallel" configuration.*
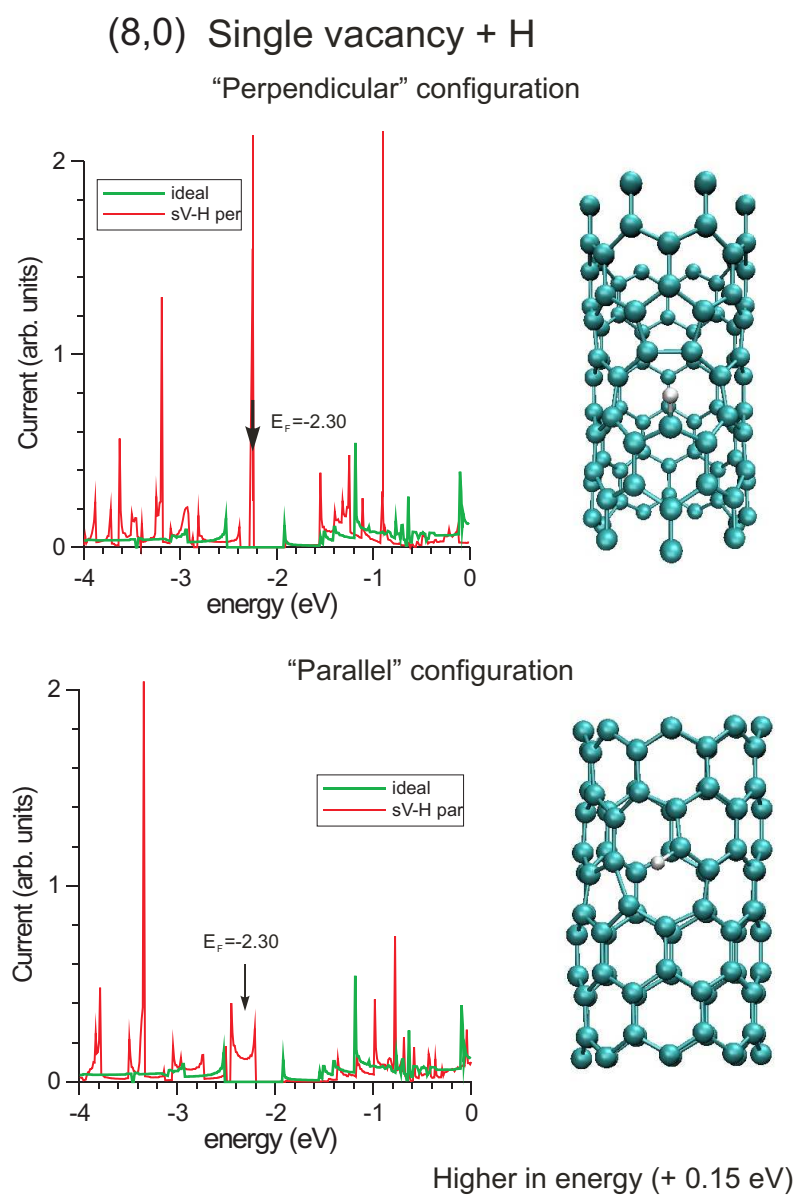
Figure B.6: *Upper panel: Ball-and-stick model and LDOS of a* $(8,0)$ *SWNT with a SV decorated with one H adatom, with the saturating bond oriented perpendicular to the tube axis. Lower panel: the same for the "parallel" configuration.*
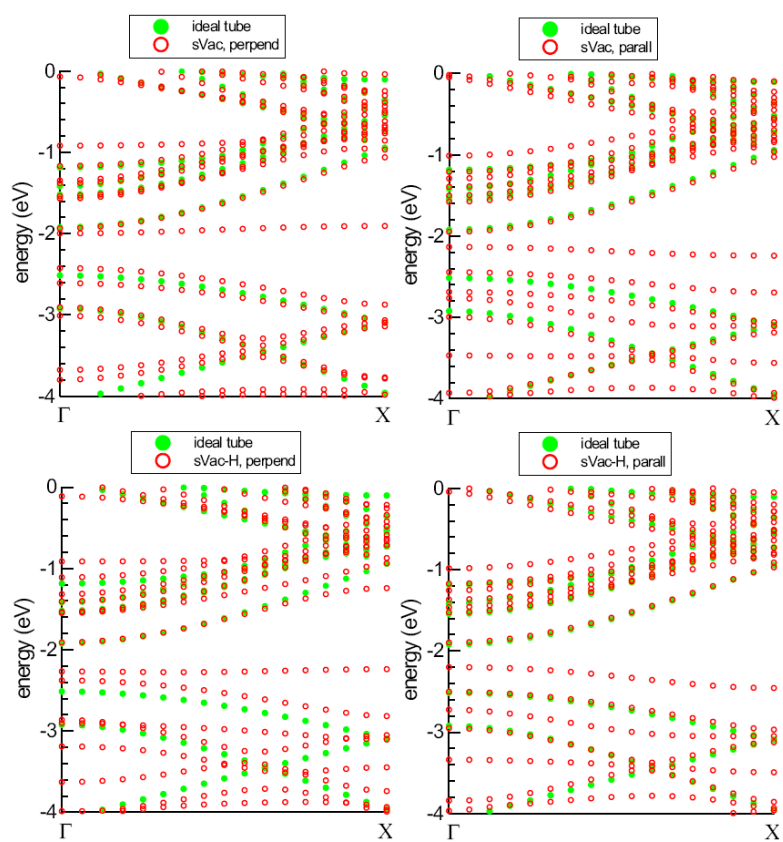
Figure B.7: *Band structures for* (8,0) *SWNTs with the different defect configurations presented in Figs. B.5 and B.6.*

Bibliography

[1] S. Iijima, Nature **354**, 56 (1991).

[2] S. J. Tans *et al.*, Nature **386**, 474 (1997).

[3] H. W. C. Postma *et al.*, Science **293**, 76 (2001).

[4] S. J. Tans, A. R. M. Verscheueren, and C. Dekker, Nature **393**, 49 (1998).

[5] A. Bachtold, P. Hadley, T. Nakanishi, and C. Dekker, Science **294**, 1317 (2001).

[6] V. Derycke, R. Martel, J. Appenzeller, and P. Avouris, Nanolett. **1**, 453 (2001).

[7] S. J. Wind *et al.*, Appl. Phys. Lett. **80**, 3817 (2002).

[8] M. S. Arnold *et al.*, Nature Nanotech. **1**, 60 (2006).

[9] I. W. Chiang *et al.*, J. Phys. Chem. B **105**, 8297 (2001).

[10] Z. Yao, H. W. C. Postma, L. Balents, and C. Dekker, Nature **402**, 273 (1999).

[11] M. Bockrath *et al.*, Science **291**, 283 (2001).

[12] Y. Fan, B. R. Goldsmith, and P. G. Collins, Nature Mater. **4**, 906 (2005).

[13] C. Zhou, J. Kong, E. Yenilmez, and H. Dai, Science **290**, 1552 (2000).

[14] R. Droppa, Jr. *et al.*, Phys. Rev. B **69**, 045405 (2004).

[15] G. Gómez-Navarro *et al.*, Nature Mater. **4**, 534 (2005).

[16] H. W. Kroto *et al.*, Nature **318**, 162 (1985).

[17] R. Saito, G. Dresselhaus, and M. S. Dresselhaus, *Physical Properties of Carbon Nanotubes* (Imperial College Press, London, UK, 2003).

[18] S. Reich, C. Thomsen, and J. Maultzsch, *Carbon Nanotubes* (WILEY-VCH Verlag, Weinheim, Germany, 2004).

[19] G. Cuniberti, G. Fagas, and K. Richter, *Lecture Notes in Physics Vol. 680: Introducing Molecular Electronics* (Springer Verlag, Berlin and Heidelberg, Germany, 2005).

[20] J.-C. Charlier, X. Blase, and S. Roche, Rev. Mod. Phys. **79**, 677 (2007).

[21] K. S. Novoselov *et al.*, Nature **438**, 197 (2005).

[22] Y. Zhang, Y. W. Tan, H. L. Stormer, and P. Kim, Nature **438**, 201 (2005).

[23] M. Bockrath *et al.*, Nature **397**, 598 (1999).

[24] R. Saito, G. Dresselhaus, and M. S. Dresselhaus, Phys. Rev. B **61**, 2981 (2000).

[25] C. Dekker, Phys. Today **52(5)**, 22 (1999).

[26] M. Ouyang, J. L. Huang, C. L. Cheung, and C. M. Lieber, Science **292**, 702 (2001).

[27] A. D. Vita, J.-C. Charlier, X. Blase, and R. Car, Appl. Phys. A **68**, 283 (1999).

[28] A. V. Krasheninnikov, P. O. Lehtinen, A. S. Foster, and R. M. Nieminen, Chem. Phys. Lett. **418**, 132 (2006).

[29] F. Banhart, Rep. Prog. Phys. **62**, 1181 (1999).

[30] Z. Osváth *et al.*, Phys. Rev. B **72**, 045429 (2005).

[31] A. V. Krasheninnikov *et al.*, Phys. Rev. B **69**, 073402 (2004).

[32] P. O. Lehtinen *et al.*, Phys. Rev. Lett. **91**, 017202 (2003).

[33] A. J. Stone and D. J. Wales, Chem.Phys.Lett. **128**, 501 (1986).

[34] D. Orlikowski, M. B. Nardelli, J. Bernholc, and C. Roland, Phys. Rev. B **61**, 14194 (2000).

[35] P. Jensen, J. Gale, and X. Blase, Phys. Rev. B **66**, 193403 (2002).

[36] M. Berthe *et al.*, Nanolett. **7**, 3623 (2007).

[37] L. Chico, L. X. Benedict, S. G. Louie, and M. L. Cohen, Phys. Rev. B **54**, 2600 (1996).

[38] M. Ouyang, J. L. Huang, C. L. Cheung, and C. M. Lieber, Science **291**, 97 (2001).

[39] A. Hashimoto *et al.*, Nature (London) **430**, 870 (2004).

[40] A. V. Krasheninnikov *et al.*, Phys. Rev. B **63**, 245405 (2001).

[41] H. J. Choi, J. Ihm, S. G. Louie, and M. L. Cohen, Phys. Rev. Lett. **84**, 2917 (2000).

[42] S. H. Lim, R. Li, W. Ji, and J. Lin, Phys. Rev. B **76**, 195406 (2007).

[43] S. Lee *et al.*, Phys. Rev. Lett. **95**, 166402 (2005).

[44] M. Bockrath *et al.*, Science **275**, 1922 (1997).

[45] A. Y. Kasumov *et al.*, Science **284**, 1508 (1999).

[46] M. T. Woodside and P. L. McEuen, Science **296**, 1098 (2002).

[47] R. Martel *et al.*, Appl. Phys. Lett. **73**, 2447 (1998).

[48] C. L. Kane and E. J. Mele, Phys. Rev. Lett. **78**, 1932 (1997).

[49] T. Ando, J. Phys. Soc. Jpn. **74**, 777 (2005).

[50] T. Ando and T. Nakanishi, J. Phys. Soc. Japan **67**, 1704 (1998).

[51] T. Ando, Semicond. Sci. Technol. **15**, R13 (2000).

[52] M. Bockrath *et al.*, Science **291**, 283 (2001).

[53] Y. Fan, B. R. Goldsmith, and P. G. Collins, Nature Mater. **4**, 906 (2005).

[54] R. Wiesendanger, *Scanning probe microscopy and spectroscopy. Methods and applications.* (Cambridge University Press, Cambridge, Great Britain, 1994).

[55] G. Binnig and H. Rohrer, IBM Journal of Research and Development **30**, 4 (1986).

[56] F. Schwabl, *Quantenmechanik, Eine Einfhrung* (Springer, Berlin, 2002).

[57] J. Bardeen, Phys. Rev. Lett. **6**, 57 (1961).

[58] J. Tersoff and D. R. Hamann, Phys. Rev. B **31**, 805 (1985).

[59] K. von Bergmann, *Iron nanostructures studied by spin-polarised scanning tunneling microscopy* (Ph.D thesis, University of Hamburg, Germany, 2004).

[60] G. Binnig, C. F. Quate, and C. Gerber, Phys. Rev. Lett. **56**, 930 (1986).

[61] F. J. Giessibl, Rev. Mod. Phys. **75**, 949 (2003).

[62] *Scanning Probe Microscopy Training Notebook* (Digital Instruments, Veeco Metrology Group, http://www.eng.yale.edu/uelm/Document% 5Cafm.pdf, 2000).

[63] I. B. Chapman, *Glow Discharge Processes: Sputtering and Plasma Etching* (John Wiley and Sons, New York, USA, 1980).

[64] A. Grill, *Cold Plasma in Materials Fabrication: From Fundamentals to Applications* (IEEE Press, New York, USA, 1994).

[65] M. J. O'Connell *et al.*, Science **297**, 593 (2002).

[66] J. N. Coleman *et al.*, J. Phys. Chem. B **108**, 3446 (2004).

[67] M. Zheng *et al.*, Nature Mater. **2**, 338 (2003).

[68] K. K. Kim *et al.*, Journal of Nanoscience and Nanotechnology **5**, 1055 (2005).

[69] J. Liu *et al.*, Nature **385**, 780 (1997).

[70] H. W. C. Postma, A. Sellmeijer, and C. Dekker, Advanced Mat. **12**, 1299 (2000).

[71] M. Sano, A. Kamino, J. Okamura, and S. Shinkai, Science **293**, 1299 (2001).

[72] T. S. Jespersen and J. N. rd, Nanolett. **5**, 1838 (2005).

[73] N. Izard, D. Riehl, and E. Anglaret, AIP Conference Proceedings **685**, 235 (2003).

[74] www.arrandee.com .

[75] M. Ouyang, J.-L. Huang, and C. M. Lieber, Phys. Rev. Lett. **88**, 066804 (2001).

[76] J. W. G. Wildöer *et al.*, Nature **391**, 59 (1998).

[77] T. W. Odom, J. L. Huang, P. Kim, and C. M. Lieber, Nature **391**, 62 (1998).

[78] H. Mizes, S. Park, and W. Harrison, Phys. Rev. B **36**, 4491 (1987).

[79] C. L. Kane and E. J. Mele, Phys. Rev. B **59**, 12759 (1999).

[80] L. C. Venema, V. Meunier, P. Lambin, and C. Dekker, Phys. Rev. B **61**, 2991 (2000).

[81] A. Rubio, Applied. Physics A: Mater. Sci. Process. **68**, 275 (1999).

[82] H. Yorikawa and S. Muramatsu, Phys. Rev. B **52**, 2723 (1995).

[83] Y. Li *et al.*, J. Phys. Chem B **109**, 6968 (2005).

[84] L. Schlapbach and A. Züttel, Nature **414**, 353 (2001).

[85] A. Nikitin *et al.*, Phys. Rev. Lett. **95**, 225507 (2005).

[86] J. Küppers, Surf. Sci. Rep. **22**, 249 (1995).

[87] P. Esquinazi *et al.*, Phys. Rev. Lett. **91**, 227201 (2003).

[88] J. A. Chan *et al.*, Phys. Rev. B **70**, 041403(R) (2004).

[89] P. O. Lehtinen *et al.*, Phys. Rev. Lett. **93**, 187202 (2004).

[90] N. Katz *et al.*, Astrophys. J. **522**, 305 (1999).

[91] T. Yildirim, O. Glseren, and S. Ciraci, Phys. Rev. B **64**, 075404 (2001).

[92] S. M. Lee *et al.*, J. Am. Chem. Soc. **123**, 5059 (2001).

[93] E. J. Duplock, M. Scheffler, and P. J. D. Lindan, Phys. Rev. Lett. **92**, 225502 (2004).

[94] G. Zhang *et al.*, J. Am. Chem. Soc. **128**, 6026 (2006).

[95] A. S. Barnard, S. P. Russo, and I. K. Snook, Phys. Rev. B **68**, 235407 (2003).

[96] A. Allouche *et al.*, J. Chem. Phys. **123**, 124701 (2005).

[97] P. Ruffieux *et al.*, Phys. Rev. Lett. **84**, 4910 (2000).

[98] P. Ruffieux *et al.*, Phys. Rev. B **71**, 153403 (2005).

[99] L. Hornekær *et al.*, Phys. Rev. Lett. **96**, 156104 (2006).

[100] L. Hornekær *et al.*, Phys. Rev. Lett. **97**, 186102 (2006).

[101] G. Zhang *et al.*, J. Am. Chem. Soc. **128**, 60266027 (2007).

[102] P. Ruffieux *et al.*, Phys. Rev. B **66**, 245416 (2002).

[103] S. Park, D. Srivastava, and K. Cho, Nano Lett. **3**, 1273 (2003).

[104] J. Bohdansky, J. Roth, and H. L. Bay, J. Appl. Phys. **51**, 2861 (1980).

[105] A. V. Krasheninnikov *et al.*, Phys. Rev. B **72**, 125428 (2005).

[106] C. Kanai, K. Watanabe, and Y. Takakuwa, Phys. Rev. B **63**, 235311 (2001).

[107] G. Zhang *et al.*, Science **314**, 974 (2006).

[108] A. Hassanien *et al.*, Nanotechnology **16**, 278 (2005).

[109] V. V. Khvostov, M. B. Guseva, V. G. Babaev, and E. A. Osherovich, Surf. Sci. **320**, L123 (1994).

[110] A. V. Krasheninnikov, Sol. Stat. Comm. **118**, 361 (2001).

[111] H. Amara *et al.*, Phys. Rev. B **76**, 115423 (2007).

[112] Y. Miyamoto *et al.*, Phys. Rev. B **69**, 121413(R) (2004).

[113] W. Clauss *et al.*, Europhys. Lett. **47**, 601 (1999).

[114] L. Tapasztó *et al.*, Phys. Rev. B **74**, 235422 (2006).

[115] P. E. Blöchl, O. Jepsen, and O. K. Andersen, Phys. Rev. B **49**, 16223 (1994).

[116] Y. Ferro, F. Marinelli, and A. Allouche, Chem. Phys. Lett. **368**, 609 (2003).

[117] A. J. Lu and B. C. Pan, Phys. Rev. Lett. **92**, 105504 (2004).

[118] M. Hjort and S. Stafström, Phys. Rev. B **61**, 14089 (2000).

[119] L. Vitali *et al.*, Phys. Rev. Lett. **96**, 086804 (2006).

[120] J. W. Janssen, S. G. Lemay, L. P. Kouwenhoven, and C. Dekker, Phys. Rev. B **65**, 115423 (2002).

[121] D. Haude, *Rastertunnelspektroskopie auf der InAs(110)-Oberfläche: Untersuchungen an drei-, zwei- und nulldimensionalen Elektronensystemen im Magnetfeld* (Ph.D thesis, University of Hamburg, Germany, 2001).

[122] J. Repp, F. Moresco, G. Meyer, and K.-H. Rieder, Phys. Rev. Lett. **85**, 2981 (2000).

[123] http://www.mcc.uiuc.edu/cgi-bin/software/software.pl.

[124] H. Hsu and L. E. Reichl, Phys. Rev. B **72**, 155413 (2005).

[125] K. Iakoubovskii *et al.*, Appl. Phys. Lett. **89**, 173108 (2006).

[126] X. Yang and J. Ni, Phys. Rev. B **74**, 195437 (2006).

[127] J. Kotakoski *et al.*, Phys. Rev. B **71**, 205408 (2005).

[128] J. Kotakoski, J. Pomoell, A. V. Krasheninnikov, and K. Nordlund, Nucl. Instr. and Meth. in Phys. Res. B **228**, 31 (2005).

[129] A. V. Krasheninnikov and F. Banhart, Nature Mater. **6**, 723 (2007).

[130] A. Tolvanen, J. Kotakoski, A. V. Krasheninnikov, and K. Nordlund, Appl. Phys. Lett. **91**, 173109 (2007).

[131] A. V. Krasheninnikov, K. Nordlund, and J. Keinonen, Phys. Rev. B **65**, 165423 (2002).

[132] A. Rubio *et al.*, Phys. Rev. Lett **82**, 3520 (1999).

[133] L. Esaki and P. J. Stiles, Phys. Rev. Lett. **16**, 1108 (1966).

[134] L. Esaki, Rev. Mod. Phys. **46**, 237 (1974).

[135] L. L. Chang, E. E. Mendez, and C. Tejedor, *Resonant tunneling in semiconductors: physics and applications* (Plenum Press, New York, 1991).

[136] F. Capasso, *Physics of quantum electron devices* (Springer-Verlag, Heidelberg, 1990).

[137] P. Bedrossian, D. M. Chen, K. Mortensen, and J. A. Golovchenko, Nature **342**, 258 (1989).

[138] I.-W. Lyo and P. Avouris, Science **245**, 1369 (1989).

[139] Y. Xue *et al.*, Phys. Rev. B **59**, R7852 (1999).

[140] C. Zeng *et al.*, Appl. Phys. Lett. **77**, 3595 (2000).

[141] N. P. Guisinger *et al.*, Nanolett. **4**, 55 (2004).

[142] S. Y. Quek *et al.*, Phys. Rev. Lett. **98**, 066807 (2007).

[143] M. Grobis, A. Wachowiak, R. Yamachika, and M. F. Crommie, Appl. Phys. Lett. **86**, 204102 (2005).

[144] L. Chen *et al.*, Phys. Rev. Lett. **99**, 146803 (2007).

[145] J. Gaudioso, L. J. Lauhon, and W. Ho, Phys. Rev. Lett. **85**, 1918 (2000).

[146] P. Liljeroth *et al.*, Phys. Chem. Chem. Phys. **8**, 3845 (2006).

[147] L. Jdira *et al.*, Phys. Rev. B **73**, 115305 (2006).

[148] B. J. LeRoy, S. G. Lemay, J. Kong, and C. Dekker, Nature **432**, 371 (2004).

[149] A. Zazunov, D. Feinberg, and T. Martin, Phys. Rev. B **73**, 115405 (2006).

[150] S.-W. Hla, K.-F. Braun, and K.-H. Rieder, Phys. Rev. B **67**, R201402 (2003).

[151] S.-W. Hla, K.-F. Braun, B. Wassermann, and K.-H. Rieder, Phys. Rev. Lett. **93**, 208302 (2004).

[152] L. P. Kouwenhoven and C. M. Marcus, Phys. World **11**, 35 (1998).

[153] J. M. Elzerman *et al.*, Nature **430**, 431 (2004).

[154] M. Nielsen and I. L. Chuang, *Quantum Computation and Quantum Information* (Cambridge University Press, Cambridge, UK, 200).

[155] J. V. Barth, G. Costantini, and K. Kern, Nature **437**, 671 (2005).

[156] C. Schönenberger, Semicond. Sci. Technol. **21**, S1 (2006).

[157] S. Sapmaz *et al.*, Phys. Rev. B **71**, 153402 (2005).

[158] M. R. Gräber *et al.*, Phys. Rev. B **74**, 075427 (2006).

[159] T. Maltezopoulos *et al.*, Appl. Phys. Lett. **83**, 1011 (2003).

[160] S. G. Lemay *et al.*, Nature **412**, 617 (2001).

[161] B. E. A. Saleh and M. C. Teich, *Fundamentals of Photonics* (Wiley-Interscience, New York, USA, 2007).

[162] W. Liang *et al.*, Nature **411**, 665 (2001).

[163] R. Bracewell, Science **248**, 697 (1990).

[164] L. C. Venema *et al.*, Phys. Rev. B **62**, 5238 (2000).

[165] A. Rubio, S. P. Apell, L. C. Venema, and C. Dekker, Eur. Phys. J. B **17**, 301 (2000).

[166] J. Lefebvre, D. G. Austing, J. Bond, and P. Finnie, Nanolett. **6**, 1603 (2006).

[167] B. J. LeRoy *et al.*, Nanolett. **7**, 2937 (2007).

[168] A. K. Geim and K. S. Novoselov, Nature Mater. **6**, 183 (2007).

[169] M. Y. Han, B. Özyilmaz, Y. Zhang, and P. Kim, Phys. Rev. Lett. **206805**, (2007).

[170] P. E. Blöchl, Phys. Rev. B **50**, 17953 (1994).

[171] J. P. Perdew *et al.*, Phys. Rev. B **46**, 6671 (1992).

[172] G. Kresse and J. Furthmüller, Phys. Rev. B **54**, 11169 (1996).

Publications list

Publications in journals and proceedings:

- *Creation and STM/STS Investigations of Hydrogen Ions Induced Defects on Single-Walled Carbon Nanotubes* , G. Buchs, P. Ruffieux, P. Gröning, and O. Gröning, J. Phys.: Conf. Ser. **61**, 160 (2007).

- *Scanning Tunneling Microscopy Investigations of Hydrogen Plasma-Induced Electron Scattering Centers on Single-Walled Carbon Nanotubes*, G. Buchs, P. Ruffieux, P. Gröning, and O. Gröning, Appl. Phys. Lett. **90**, 013104 (2007).

- *Creation of paired electron states in the gap of semiconducting carbon nanotubes by correlated hydrogen adsorption*, G. Buchs, A. V. Krasheninnikov, P. Ruffieux, P. Gröning, A. S. Foster, R. M. Nieminen and O. Gröning, New Journal of Physics **9**, 275 (2007).

Talks:

- *Local Modification and Characterization of the Electronic Structure of Carbon Nanotubes*, 1st Empa Symposium for Ph.D. students, 20. October 2005, Dübendorf, Switzerland.

- *STM/ STS Investigations of Single-Walled Carbon Nanotubes Defects Induced by Low-Energy Hydrogen Ions*, ICN+T 2006: International Conference on Nanoscience and Technology, 1. August 2006, Basel, Switzerland.

- *Local Modification and Characterization of the Electronic Structure of Carbon Nanotubes*, (**invited**), TU Delft, Quantum Transport group seminar, Prof. L. Kouwenhoven, 28. April 2006, Delft, The Netherlands.

- *STM/STS Investigations of Single-Walled Carbon Nanotubes Defects Induced by Low-Energy Hydrogen Ions*, Empa Ph.D Symposium, 19. October 2006, Dübendorf, Switzerland.

- *Local Modification and Characterization of the Electronic Structure of Carbon Nanotubes*, (**invited**), Universität Freiburg, Theoretical Solid State Physics group seminar, Prof. H. Grabert, 13. November 2007, Freiburg, Germany.

- *Local Modification and Characterization of the Electronic Structure of Carbon Nanotubes*, (**invited**), ETH Zürich, Micro- and Nanosystems group seminar, Prof. C. Hierold, 4. April 2008, Zürich, Switzerland.

Poster contributions:

- *Local Modification and Characterization of the Electronic Structure of Carbon Nanotubes*, NT05: 6th International Conference on the Science and Application of Nanotubes, 26. June-1. July 2005, Gothenburg, Sweden.

- *Local Modification and Characterization of the Electronic Structure of Carbon Nanotubes*, CFN Summer School on Nano-Electronics, 1.-4. September 2005, Bad Herrenalb, Germany.

- *Local Modification and Characterization of the Electronic Structure of Carbon Nanotubes*, (**invited**), NCCR (NANO) Annual Meeting, 6.-7. October 2005, Gwatt, Switzerland.

- *Local Modification and Characterization of the Electronic Structure of Carbon Nanotubes*, SPS/Manep meeting, 13.-14. February 2006, EPF Lausanne, Switzerland.

- *Quasi-Bound States in Intra-Carbon Nanotube Quantum Dots*, 3rd European Conference on the Fundamental Properties of Mesoscopic Physics and Nanoelectronics, 9.-14. September 2007, Mojacar, Spain.

Curriculum Vitae

Gilles Buchs

9. 9. 1976	Born in Payerne (VD)
1983 - 1989	Primary school in Aumont, Nuvilly and Vesin (FR)
1989 - 1992	Secondary school in Estavayer-le-Lac (FR)
1992 - 1996	Apprenticeship at OFEFA Payerne (VD) on electronics with focus on measurement techniques
1996	Academic studies at the engineering school Fribourg
1999	Electronic engineering degree, with focus on telecommunications
1999	Physics study at the ETH Zürich
2003	Bachelor degree in physics, minor degree in semiconductor nanostructures
2003 - 2004	Master thesis at the ETH Lausanne, chief-supervised by Prof. Dr. K. Ensslin (ETH Zürich), in the group of Prof. Dr. A. Fiore on the topic: "*Characterization of single semiconductor quantum dots emitting in the infrared*"
2004	Master degree in experimental physics, Dipl. Phys. ETHZ
2004	Start of the present PhD thesis
17. 06. 2008	PhD exam

For valuable lectures and experimental guidance during my studies I am indebted to:

Engineering School Fribourg
Christoph Herren, Ottar Johnsen, Seraina Kind and Mathias Rech.

ETH Zürich
G. Blatter, K. Ensslin, T. Ihn, H. R. Ott, M. Sigrist and E. Trubowitz.

ETH Lausanne
A. Fiore and V. Zwiller.

University of Basel
C. Schönenberger

Acknowledgements

This thesis is the result of four years of work accomplished at EMPA, the Swiss Federal Labs for Material Testing and Research, section 127: nanotech@surfaces in Thun. During all this time, I have been accompanied and supported by many people. It is now my great pleasure to take this opportunity to acknowledge them.

I thank Prof. Christian Schönenberger for the acceptance of being my "Doktorvater". This situation of having you so far from my work place has not always been easy, but it was always a pleasure to meet you in Basel and to discuss about my results.

I am grateful to my supervisor at EMPA, Dr. Oliver Gröning. He was involved in all stages of this work: from the definition of the project to the discussion of the experimental data. He was always available for all kinds of questions related or not to the project. His broad knowledge in many scientific fields was always profitable to me. Oliver, your incredible skills in programming will always impress me. Thank you very much for all you did to help me during these four exciting years.

I thank Prof. Klaus Kern and Prof. Christofer Hierold for their acceptance of being referees for this thesis.

I would like to thank all the permanent members of the nanotech@surfaces group in Thun: Dr. Pascal Ruffieux, Dr. Roland Widmer, Dr. Pierangelo Gröning. In particular, I would like to thank Dr. Pascal Ruffieux for the introduction to the LT-STM. I could learn a lot from his wide knowledge on surface physics. I would also like to thank Dr. Roland Widmer for the introduction to the AFM techniques. His practical skills (also for MS Word...) were often useful. Pascal and Roland, thank you for the help you always provided me when problems occurred in the lab, even if it was during the weekend or late in the evening.

I would like also to thank the permanent members of the nanotech@surfaces group in Dübendorf: Dr. Roman Fasel and Drs. Daniele Passerone and Carlo Pignedoli for their theoretical support, especially for the TB calculations.

I thank Dr. Arkady Krasheninnikov, Dr. Adam Foster and Antti Tolva-

173

nen for performing DFT calculations. Arkady, thank you again for the nice visit of Helsinki and your availability for my numerous questions.

I thank Dr. Dario Bercioux for theoretical support on the confinement effects. Thank you Dario for the nice time I spent in Freiburg and for your help in latex.

I would like to acknowledge all my colleagues and ex-colleagues at EMPA, Dr. Marta Canas Ventura, Dr. Ana Isabel Borras, Dr. Kamel Ait-Mansour, Dr. Xiao Wende, Dr. Michael Bielmann, Matthias Treier, Ruben Mäder and Thomas Mattle. Marta, thank you for your precious advice during the writing phase. Kamel, I will not forget the long nights in the lab, trying to image epitaxial graphene and talking about faith.

I would like to express my gratitude to Anton Böll who fabricated precious sample holders for me.

I would like to thank our staff, Christian Kauer for support with all informatics stuff, Gerhard Bürki for for performing TEM images of my suspended tubes, and our secretaries Katrin Gurtner and Eveline Straubhaar for their availability and kindness.

I thank Dr. Val Zwiller for the opportunity he gave me to visit him several times at the TU Delft for performing optics experiments on suspended tubes and also to have fun.

I thank Dr. O. Johnsen for helpful discussions about Fourier Transforms.

I thank Dr. M. Rech for his help in English grammar.

I thank my parents. I owe them a lot even if they did not always understand my taste for long studies. Papi, I know you were proud of me.

I would like to thank David Chaignat, my roommate. David, you are the best roommate I've ever had.

I would like to thank my friends at the ICF church in Lausanne and Bern, Nathalie and Avo, Harry, Ronny, Raphi, Marcel, Chrigu, Danu, Reto, Domenica and all my sisters and brothers in Christ for their prayers and support.

And last but not least, I thank you God for everything. The privilege I had to study Your amazing creation, particularly at the atomic level, added an entire dimension of excitement to my research. *"By faith we understand that the universe was formed at God's command, so that what is seen was not made out of what was visible."* (the Apostle Paul's letter to the Hebrews, chapter 11, verse 3, New International Version of the Bible).